The development of mixed oxide adsorbents and catalysts through continuous flow processes.

Gareth John Weightman

A thesis submitted for the degree of Doctor of Philosophy

University of Warwick

School of Engineering

June 2016

Acknowledgements

Many thanks go to MEL Chemicals Ltd. for the raw materials they provided and for the funding they provided for the project. In particular Emiliana Dvininov and Hazel Stephenson have been of great assistance throughout the project. Funding was also provided by ESPRC (allocated by Chemistry Innovation Knowledge Transfer Network (CIKTN)) and by BioGo. Gareth Weightman is grateful to Alexei Lapkin and Andre van Veen for their supervision and guidance throughout the project. Gareth Weightman is grateful to Ben Douglas at the University of Warwick, Department of Chemistry for operating the porosimeter and to John Hanna and Samuel Page for providing ^{27}Al NMR. Many thanks are given to Rob Brown and Marta Granollers for the performance of microcalorimetry and to Warwick Analytical Services for the performing of ICP and CHN analysis. Gareth Weightman is appreciative to Yulia Fedorova for performing the catalytic testing. Many thanks to Richard Walton for his kind loan of a Bruker X-Ray Diffractometer.

Declaration

This thesis is submitted to the University of Warwick in support of my application for the degree of Doctor of Philosophy. It has been composed by myself and has not been submitted in any previous application for any degree.

The work presented (including data generated and data analysis) was carried out by the author except in the cases outlined by below.

^{27}Aluminium nuclear magnetic resonance was performed by John Hanna and Samuel Page.

Porosimetry was performed by Ben Douglas

Catalytic steam reforming was performed by Yulia Fedorova

ICP and CHN analyses were performed by Warwick Analytical Services

Microcalorimetry was performed by Rob Brown and Marta Granollers.

Table of Contents

List of Figures

List of Tables

Abstract

The aim of this project was to produce solid adsorbents and catalysts in a continuous flow process. These materials are traditionally made in a batch process. The materials were made and the effect of the change in synthesis explored.

When hydrotalcite was produced in a batch process it was found to yield material that was synthesised by a reaction governed by thermodynamic control. Contrary, solid formation in a continuous flow it was found to be governed by a kinetically controlled reaction. During the batch reaction the reactants had time and mobility to precipitate, dissolve and re-precipitate in order to arrive at the lowest energy configuration. This configuration resulted in aluminium from one meixnerite intermediate layer aligning with aluminium in the opposing layer (referred to as "in phase"). This allowed carbonate anions to join the layers together creating a crystalline structure by balancing its charge between the two aluminium atoms. In a continuous flow process the reactants were not afforded either the time or space to move. This resulted in aluminium being randomly located within the meixnerite intermediate. Due to the random placement of aluminium, the aluminium in opposing layers did not consistently align (referred to as "out of phase"). Carbonate anions bound to these out of phase aluminium atoms are unable to balance their charge by linking layers together. The anions compensated by taking up hydrogen and forming a bicarbonate anion. The remaining aluminium took up monovalent nitrate anions in the absence of any divalent anions. Hydroxide anions would have been more favourable but they were required in the formation of the lattice. It was also found that the kinetically controlled product could be converted to the

thermodynamically controlled product by washing. Washing, however, degraded the lattice structure and washed away an amount of material.

The hydrotalcites produced by continuous flow process were thermally decomposed to act as a carbon dioxide adsorbent. They decomposed much faster than their batch counterparts, suggesting the carbonate bridge provides thermal stability to the material. The decomposition also revealed that the magnesium/aluminium spinel recorded in other studies did not form for the materials produced in a continuous flow process. Instead the material decomposed to the separate metal oxides. This did not have an effect on the ability of the material to adsorb carbon dioxide and performed comparably to the batch process materials.

The continuous flow process was used to create a Ni/Mg/Al hydrotalcite that could be used as a catalyst in ethanol steam reforming. The continuous flow process allowed three processes for introducing nickel into the system: the doping of the starting reagents, ion exchange during the washing process and the impregnation of the dry product. The doped samples produced material comparable to those produced in continuous flow without doping or washing. The ion exchange and the impregnation samples produced samples that are comparable to those produced in continuous flow with washing The doped samples exhibited a fourth region of weight loss in thermogravimetric analysis which is speculated to be the formation of nickel aluminide at high temperatures. The catalytic activity corroborated this idea with an increase in metallic behaviour. The doped sample was found to be the more active sample tested.

In order to further test the effect of kinetic and thermodynamic control during the continuous flow process, an attempt to control the particle size of zirconium basic

sulfate was made. It was found that the particle size could be altered in the batch process due the variable environment within the reactor. Inefficient mixing created concentration gradients and inefficient heating created temperature gradients. It was these gradients within the batch reactor that facilitated the thermodynamic product to be produced and the particle size to increase. In a continuous flow reactor these gradients did not exist. The advantage of the flow reactor was the ability to control the environment of the reactor in an even and uniform manner. The uniformity of the reactor environment eliminated any temperature or concentration gradients, keeping all the materials at similar chemical potentials, limiting particle growth.

Chapter 1 - Introduction

Batch processes

A batch reaction is a recipe driven process performed in a vessel without material exchange during the process, widely used in the manufacturing of fine and speciality chemicals.[1-4] It is often focused on smaller volumes of a large number of products, which requires multi-purpose equipment.[2-5] Batch processes are often comprised of simple processing units like mixers, stirrers, storage tank, pipelines and transfer units.[2, 6] Pumps that are used are not needed to be optimised but are chosen by filling and emptying times. Without the need of accurate flow rates the cost of this equipment is reduced.[1] In other processes, each unit is specially made for a specific propose under specific conditions. In a batch process, the units involved do not require these specialised qualities. This lack of definition in the process units allows them an increased flexibility with respect to a wide range of products, product quantities and recipes.[1, 2] The simplicity of the process unit means batch manufacturing plants are relatively easy to build compared to a continuous flow plant. Batch processes are easy to scale up from a lab test to manufacturing facilities depending on market demand and requirement. [1, 4, 6] The unit required for a particular processing task is referred to as a Production Unit. Within a manufacturing facility there can be multiple production units, often operating in parallel to produce a greater number of products.[2, 3, 7, 8]

A batch process is a contained reaction having a beginning and an end. [2, 6] Intermediate products can be stored, however when this is not possible they can be immediately processed in another production unit.[2, 3, 9] The output of the process appears in quantities of materials, referred to as “lots”. This leads to the reaction

needing to be repeated. If sufficient quantity cannot be obtained in one reaction, another must be started to obtain the additional product. The products of these repetitions are referred to as a batch, giving the process its name.[6, 8] Batch processes have recipes that are used to produce a product through a number of steps. A process recipe must be completed sequentially; each step must be completed, regardless of how simple or complex, before the next step can be started.[1, 4, 7, 8] Often these recipes include special steps, in the event of a step failing. [6]

A batch processing unit allows for multiple reactions in several steps and multiple products can be made within a facility, minimising the cost of equipment.[1, 6] When a single product is made using the same quantities of raw materials under the same conditions, it is known as "single-product batch processing". [4, 8-10] When different amounts of raw material are used, but the same operations are preformed to produce similar but not identical products it is referred to as "multi-grade batch processing". [11, 12] "Multi-product batch processing" is when different methods and different amounts of raw materials are used to produce different products.[2, 3, 5, 7, 9, 13] All these different types of batch processing are possible with just one processing facility. This grants a company a greater degree of diversity in its manufacturing capacities. [6]

Traditional development of a batch synthesis focuses on the reaction itself and works to improve in terms of yield and selectivity. However other aspects, including automation in synthesis, workup and isolation, still remain of fundamental importance. [14] Consequently, this has led to *enabling techniques* [14] emerging, which Kirschning *et. al.* describes as "various traditional as well as new techniques which have been developed to speed up synthetic transformations and importantly ease workup as well as isolation of products". [14]

The use of batch processing plants is common in industry. Some examples of batch processes are beverage processing, biotech products manufacturing, dairy processing, food processing, pharmaceutical formulations and soap manufacturing.[6, 12]

The batch method of synthesis also has its challenges. This is especially noticeable when an operation needs to be scaled up. The equipment that is required to satisfy industry size yields is expensive and often the cost becomes a limiting factor. This is often the reason that leads to batch processes being redesigned. When larger yields can be handled, they often are unable to reproduce the product quantity seen in lab scale reactions on a production scale. Factors that are involved in this decrease in product quality include a decrease in the mixing efficiency and the heating. Both these factors are dependent on surface area rather than volume. While both the volume and the surface area increase while scaling up, the scale is usually related to a linear dimension. Due to volume increasing by a power of three and the surface area by a power of two, a difference is produced in the scaling that leads to uneven heating and the mixing. This creates hot spots and concentration gradients within the reacting material that can destroy an entire batch.[15, 16]

If a synthesis is based on a very fast precipitation reaction, then correct stoichiometry of the product is attained through maintaining the correct reagent stoichiometry in the reaction medium. [4, 17, 18] This is ultimately impossible to attain in a batch process when reaction times are faster than the characteristic mixing times, typical of large batch reaction vessels. Stirring in classical reactors, such as round bottomed flasks and larger batch reactors are limited by inconsistencies in the flow fields created by the stirring mechanism. As the fluid approaches the stirrer, convection is induced.

This results in turbulence, which leads to chaotic mixing. [19-21] The shear forces that cause the convection are considerably diminished further away from the stirrer. If a reaction is highly exothermic, then a fast release of energy during the synthesis under batch reaction conditions significantly affects the reaction environment and gives rise to risks to process safety. [17, 22-25]

Continuous flow process

A continuous production is a flow production method that produces a material without interruption. This allows for long operating hours which need a minimal amount of intervention and maintenance. This type of processing is often used in large scale chemical plants. Some of the common continuous flow processes include; oil refining, bulk chemical (commodity) synthesis, metal smelting and sanitary waste water treatment.[26] A continuous process negates the need to leave tanks and pipes full of unreacted materials, which avoids the possibility of creating any unwanted chemicals. Continuous processes also require less energy to operate them due to efficient energy recovery when serving for long periods of time meaning the processing plant reactors do not need to be frequently shut down.[27]

When producing a limited number of products in a high volume, continuous flow is typically used as it allows for the use of specialised equipment that facilitates the production.[2, 16] Continuous reactors typically consist of tubes made from non-reactive materials such as stainless steel, glass and polymers. A variety of mixing methods, including diffusion (the diameter of the reactor must be small) and static

mixers, can be incorporated.[28] Some examples of flow reactors are spinning disc reactors,[26, 29-31] microreactors[19, 32] and hex reactors.[33]

Continuous flow processes are easily automated and are very reproducible. [14] They are safe and reliability of the process can be maintained due to constant reaction parameters such as, temperature, time, amount of reagent and solvent. [14] A continuous flow process can also be improved by the combining them with other chemical techniques. [14, 34, 35] These techniques can include microwave assistance [36-38], the use of immobilised reagents and catalyst. [39, 40] They can also take advantage of new fluids such as supercritical CO_2 and ionic liquids. [14, 41] Production rates can vary from nanolitres to litres per minute.[15, 16, 42, 43]

A continuous flow reactor presents greater control over reaction conditions including heat transfer, time and mixing, ensuring consistency in each of these factors throughout the reaction.[31, 44] The residence time of the reagents in the reactor (i.e. the amount of time that the reaction is heated or cooled) is calculated from the volume of the reactor and the flow rate through it.

$$\text{Residence time} = \text{Reactor Volume} / \text{Flow Rate}$$

Therefore, to achieve a longer residence time, reagents can be pumped more slowly and/or a larger volume reactor used. [44]

There are many benefits to using a continuous flow process. Reaction temperatures can be above a solvent's boiling point due to the contained pressure of the system. Mixing can be achieved within seconds at the smaller scales, achieving rapid and homogenous mixing throughout the process. [19, 45-47] The thermal mass of the fluid is typically far lower than the thermal mass of the system (and orders of magnitude less

than with batch chemistry). This makes controlling the temperature of the reactor both faster and easier, making certain that exothermic and endothermic process can be conducted without issue.[48] With efficient temperature control, residence times may be shortened while still providing the required yield. [17, 49]

Continuous flow techniques are becoming an increasingly popular approach to streamlining multi-step synthesis. By combining multiple stages of a synthesis together, one continuous reactor network can be created.[14, 16, 17, 19, 26, 50-54] Such an approach has been called a 'one-flow, multi-step' synthesis. [17, 55] The traditional path-way for multi-step synthesis proceeds via a batch process and iterative step-by-step transformations. After each synthetic step products would require isolating and purifying before the next batch reaction could be performed.[42] With a continuous flow process it is possible to arrange a flowing system in which purification is coupled with the reaction. This circumvents the necessity to isolate intermediate product.[17, 43, 44] This becomes extremely beneficial as some intermediate compounds are unstable, since they will exist only momentarily and in very small quantities.[17] It is possible to arrange the system such that further reagents can be introduced into the flowing reaction stream at precisely the time point in the reaction that is desired.

Coupling the output of the reactor to a detector system makes it possible, with appropriate controls, to create an unattended system which can sequentially investigate a range of possible reaction parameters (varying stoichiometry, residence time and temperature). This allows for the optimisation of reactions with little or no intervention.[17, 18]

Scale up of proven reactions can be rapidly achieved with little process development. By either changing the reactor volume or by running several reactors in parallel yields can be increased without altering the original chemical reaction, provided that flow rates are recalculated where necessary to achieve the same residence times.[15, 17, 42, 44, 49]

Continuous flow processes do not come without draw backs. The materials used for the equipment must be inert to all the reagents and solvents. This can be problematic when performing multistep reactions as it can be a necessary to use different solvents at different stages. Expensive reaction columns can be degraded and require replacing. Other facilities may still be needed to purify the product with additional treatments. Problems are known to arise with different kinetics of reaction. [14, 26, 56]

Overall, with the resulting product generally being oils or liquids, the continuous method of synthesis has been established and becomes increasingly popular in the synthesis of organic compounds.[17, 22-25] Currently, designs are being developed to adapt this technology to the preparation of inorganic materials. Problems can arise from the formation of precipitates in the narrow reactor channels, which create blockages.[15, 26, 56] However with recent developments it has been possible to synthesize a range of materials, including salt-like inorganic nano-particles,[57, 58] metals [59-61] and semiconductors,[62] by using microreactor technology.

Aim of the thesis

The aim of this project is to translate the synthesis of hydrotalcites and zirconium basic sulfates to a continuous flow process. Both these materials are made by MEL Chemicals Ltd. which has an interest in converting their batch processes to

continuous flow processes. It is the aim of the project to attempt to produce these materials by a continuous route and to explore the physical properties of the materials, involving comparison with materials made in a batch made process. For hydrotalcites, the capacity to act as a solid CO_2 absorbent will be investigated, as well as their ability to perform as catalysts. For zirconium basic sulfate an interest was whether the size of the particles could be controlled during the synthesis process. By varying certain conditions in the batch process, MEL Chemicals Ltd. found that particles of different sizes could be produced. It is the aim of this project to investigate whether these effects can be reproduced under flow conditions.

Chapter 2 – Synthesis of hydrotalcites in a continuous flow process

Literature Review

Hydrotalcites were discovered in Sweden around 1842. The first accurate formula for a hydrotalcite ($Mg_6Al_2(OH)_{16}CO_3 \cdot 4H_2O$) was determined by Professor E. Manasse at University of Florence who was the first to comprehend that carbonate ions were vital to the structure.[63, 64] Since their discovery, hydrotalcites, and products of their decomposition, have mainly found applications in catalysis. Examples of their use in this capacity in polymerisation reactions [65, 66], aldol condensation reactions [67-70], ester exchange reactions [71], dehydrogenation reactions [72] and Michael additions [73-75] can be found in the literature. Hydrotalcites have also found a use in medicine as an antacid, relieving the symptoms of ulcers and heartburn. The possibility of using hydrotalcites as high temperature CO_2 adsorbents arose from previous adsorption work carried on various metal oxides, including MgO, CaO and Al_2O_3. Since then, hydrotalcite materials have become a popular target as potentially suitable adsorbents for CO_2.[76-85]

Hydrotalcites are a class of naturally occurring anionic clay known as double-layered hydroxides. [86-90] The most common hydrotalcite is generally of the formula $Mg_6Al_2(CO_3)(OH)_{16} \cdot 4H_2O$. [86, 89-96] They are made up of two distinct layers, a positively charged lattice structure and layer of counter anions. These layers link together, forming a multi-layer structure. Each of these layers will be described individually.

The first layer is an ionic lattice structure described as a brucite-like layer, being repeating units of octahedral hydroxide with both divalent and trivalent metal

centres.[63, 64, 87, 92, 94, 95, 97-104] By substituting some of the divalent metal centres with trivalent metal centres a positive charge is attained across the whole lattice structure. [64, 86, 88, 90, 94, 98-100, 102-107] The lattice is described by the formula $[M^{II}_{1-x} M^{III}_{x} (OH)_2]^{x+}$. [93, 105] While the value of *x* can differ within the literature, it can generally be seen that the value is between 0.2 and 0.33 (Table 1). Due to the repulsion of positive charges, M^{III} cations remain distant from each other in the lattice. For the optimal value of *x*, M^{III} octahedra cannot be adjacent.

Table 1. The values of *x* found in the literature

Value of *x*	**Reference**
0.2 - 0.33	Rey[98], Mantilla[108], Palmer[107]
0.1 – 0.5	Chen[106]
0.25	Millange[92], Climent[103], Miyata[93]
0.17 – 0.33	Kloprogge[87]

The bivalent and trivalent metal centres are not always necessarily magnesium and aluminium. Any bivalent or trivalent transition metal with redox properties and an ionic radius similar Mg^{2+} or Al^{3+} can adopt the same octahedral arrangement (Figure 1) and produce a hydrotalcite-like compound. [63, 90, 95, 100-102, 109, 110]

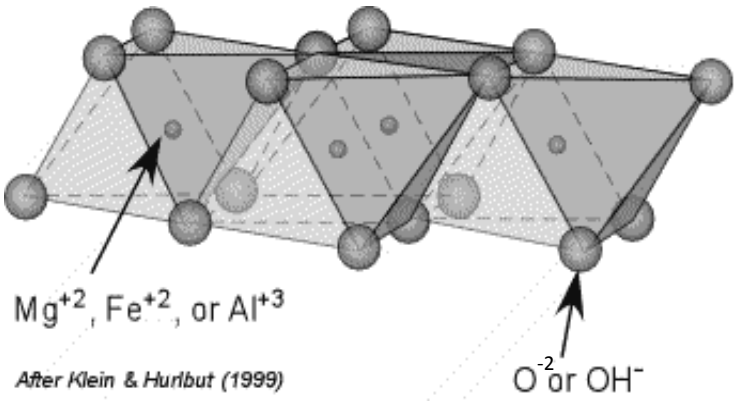

Figure 1. Diagram illustrating the structure of the lattice layer, showing the repeating octahedral units.[111]

The second layer is formed due to the positive charge of the lattice layers, attracting and intercalating with anions to compensate for the charge discrepancy.[86, 88, 90, 92, 96, 101, 103-105, 107] This becomes a multi-layered structure of alternating lattice and interspatial anion layers (Figure 2.).[94, 112] The interspatial anion layers are generally described by the formula $[X_z \cdot 4H_2O]^{2-}$.[93, 96, 106] X can represent any anion. Z is determined by the number of moles of the trivalent cation found in the lattice being divided by the charge on the anion. [91] These interspatial anions and water are usually labile and so exhibit anion exchange capacity. [90, 101, 112] Anion affinity has been found to be based on the size of the ion and its associated charge. Monovalent anions have a lower affinity than divalent anions and will be more likely to participate in ion exchange reactions. [90] Though water molecules are usually present in the crystalline structure it is possible to obtain an anhydrous material by heat treatment. [86, 112] Though any anion, such as MoO_4^{2-}, ClO_4^- or SO_4^{2-} [86, 90, 99, 102, 109, 110, 112], may be used in the formation of a synthetic hydrotalcite-like materials, this project focuses on the production of hydrotalcites with CO_3^{2-} anions. Therefore the formula for these layers will be $[CO_3 \cdot 4H_2O]^{2-}$. The anions found in-between the

brucite layer are generally found in three environments, the first being the anions bonded to the brucite layer by hydrogen bonding. Anions are also hydrogen bonded to the water found in the interspatial gap and they can be unbound anions.[90]

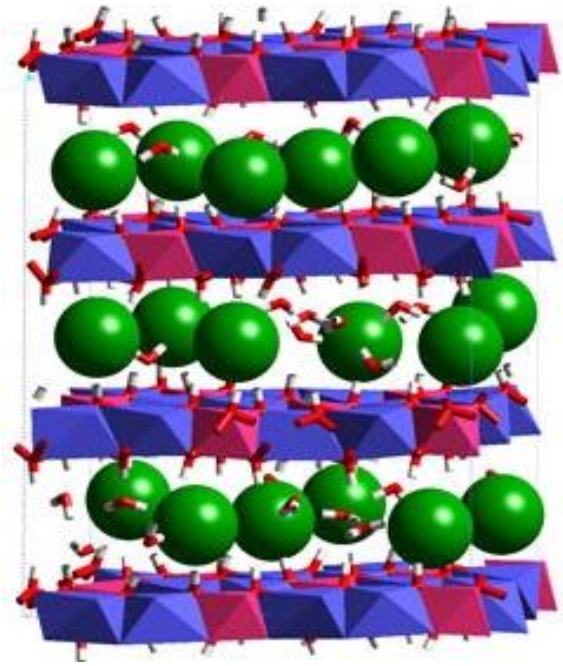

Figure 2. Diagram illustrating the co-ordination the lattice layer shown as the tetrahedral blocks and the interspatial anions represented as the spheres.[113]

Allada *et al* records an enthalpy of formation ($\Delta_f H$) of -1165.98 ± 2.06 kJ/mol (at 298 K) for a material identified as $Mg_{0.74}Al_{0.26}(OH)_2(CO_3)_{0.13}\cdot 0.39H_2O$.[114, 115] (See Table 2). In the same experiment it was found that the same material had an entropy change (ΔS) that measured 85.58 J/mol · K. [114] This was used to calculate the Gibb's free energy of formation ($\Delta_f G$) which is given as -1043 kJ/mol. [114]

Table 2. A table showing the thermodynamic properties for hydrotalcite.

Values at 298 K	$\Delta_f H$ kJ/mol	ΔS J/(mol · K)	$\Delta_f G$ kJ/mol
Hydrotalcite made Allada	-1165.98[114, 115]	85.58 [114]	-1043 [114]

By far the most common method of synthesis for hydrotalcites is by co-precipitation. This involves the drop-wise addition of magnesium and aluminium salts in solution to a solution of sodium carbonate. The pH is kept constant between 9 and 10. This is maintained by the addition of sodium hydroxide. Mixed with vigorous stirring the resulting precipitate is aged at elevated temperatures. [72, 87, 92, 93, 98, 103, 105, 106, 108, 116] Another method involves the hydrolysis of urea in the presence of the magnesium and aluminium salts. [88, 94, 116] It is reported that using the base retardant as a precipitating agent, the nucleation and particle growth can be separated, preventing aging before it begins. [116]

Experimental

Materials Preparation

The samples made in batch (HTCB) were prepared by co-precipitation at pH 9.5 and ambient temperature, by the method described by Miyata (Figure 3).[105, 114, 115, 117] A solution containing magnesium nitrate and aluminium nitrate dissolved in water was added by a HPLC pump (Knauer 100) at a rate of 3 mL min^{-1} with vigorous stirring to a solution of sodium carbonate dissolved in water. The NaOH solution was added by a manually controlled pump (Ismatec ISM597D) to maintain a pH 9.5 (see Table

2 for the quantities of the reagents). Once all the reagents had been added the mixture was left to age for 30 mins after which it was filtered through a Buchner flask and were dried in air for 12 hrs at 85 ºC.

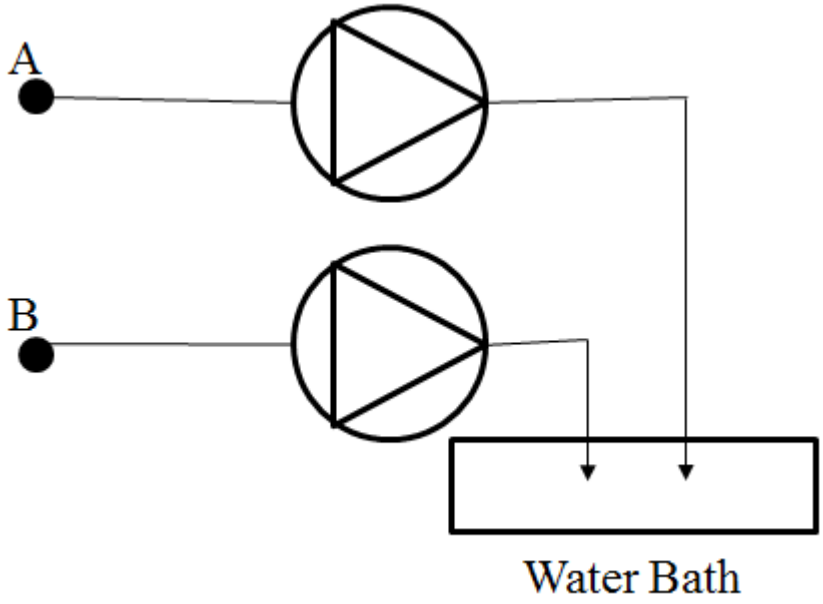

Figure 3. Arrangement of the equipment used for HTCB.

The samples prepared under flow conditions (Figure 4) were made using a system comprising of a peristaltic pump (Ismatec ISM597D) fitted with 3-stop 0.51 ID mm PVC tubes and a Y-mixer (PEEK 0.5 mm). As the hydrotalcite formed it was observed that it slowed down in the tube. This caused a backup and eventually a blockage. Several attempts were made using different length reactors before a hydrotalcite material could be made. By shortening the reactor length blockages were prevented. The decision was made to explore the effect of shortening the reactor length. A reactor comprised a 2 cm long 0.51 mm ID empty PTFE tube was short enough to produce a material of solid nature. Once the slurry had been produced it was found that it would polymerise to produce an unusable polymer when it was collected in a container (HTCF). This was prevented by allowing the

reactor output to collect in a crystallising dish of water (Figure 5) that was continuously stirred (HTCFw).

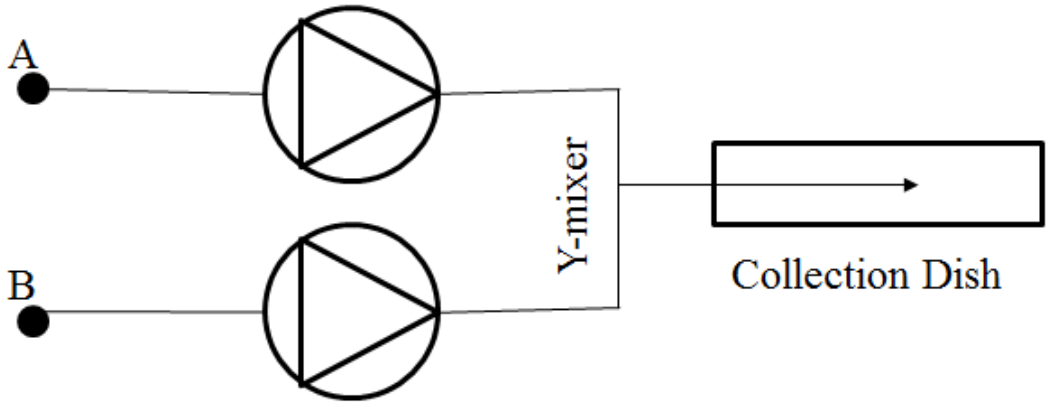

Figure 4. Arrangement of the equipment used for HTCF.

The two feed solutions were pumped at a rate of 1.5 mL min^{-1} at ambient temperature. The first solution contained magnesium and aluminium nitrates dissolved in water. The second solution contained sodium carbonate and sodium hydroxide dissolved in water. Due to the inability of monitoring the pH and the fast rate of reaction it was decided that the hydroxide would be added by stoichiometric formula, as the other reagents are added. Following filtration through a Buchner flask the product was dried in air at 85 ºC for 12 hours.

In an attempt to reduce the amount of nitrate in the material, several alterations to the method and starting reagents were investigated. Due divalent cations having a greater ion affinity than monovalent cations, the effect of doubling the amount of carbonate was looked into (HTCFc). It was considered that the pH may have been too low and this was encouraging the formation of monovalent bicarbonate ions instead of bivalent carbonate ions. Therefore the effect of doubling the amount of hydroxide was investigated (HTCFo). The effect of doubling both the carbonate and hydroxide (HTCFco) was also explored. As the with HTCFw, additional materials

were made with the standard flow parameters stated above and flowed into water, however it was decided to allow these materials to continue washing for 2 h (HTF2h) and 4 h (HTCF4h).

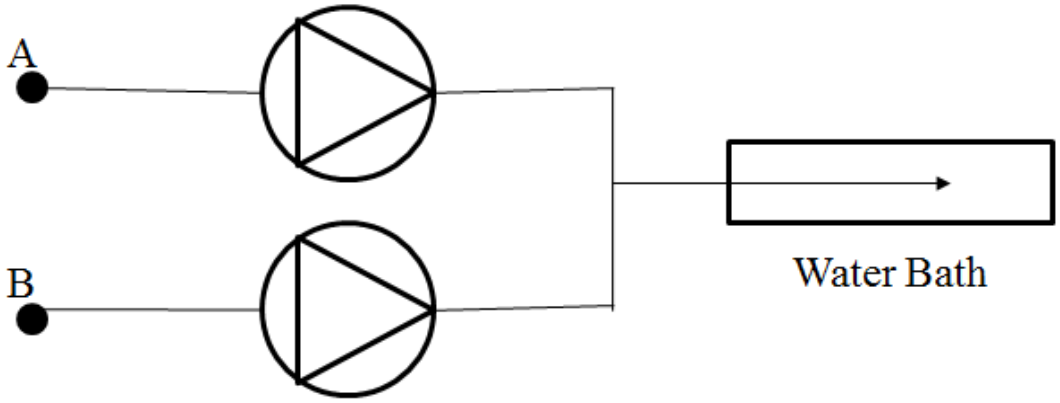

Figure 5. Arrangement of the equipment used for all samples except HTCB and HTCF.

Table 3. The molar concentrations of reactants required for both batch and flow processes

<table>
<tr><td rowspan="2">Sample</td><td colspan="4">Molar concentrations of the ions in the feed composition</td></tr>
<tr><td>Mg^{2+} (mol/l)</td><td>Al^{3+} (mol/l)</td><td>CO_3^{2-} (mol/l)</td><td>OH^- (mol/l)</td></tr>
<tr><td>HTCB</td><td rowspan="8">3</td><td rowspan="8">1</td><td rowspan="3">0.5</td><td>Varied to maintain pH</td></tr>
<tr><td>HTCF</td><td rowspan="3">8</td></tr>
<tr><td>HTCFw</td></tr>
<tr><td>HTCFc</td><td>1</td></tr>
<tr><td>HTCFo</td><td>0.5</td><td rowspan="2">16</td></tr>
<tr><td>HTCFco</td><td>1</td></tr>
<tr><td>HTCF2h</td><td rowspan="2">0.5</td><td rowspan="2">8</td></tr>
<tr><td>HTCF4h</td></tr>
</table>

Procedures of analysis

X-ray diffraction (XRD) yields information on crystalline phases within the sample. X-rays are of the wavelength ca. 10^{-10} m which is the same order of magnitude as the internuclear distances between atoms, i.e. crystalline phase.[118] XRD requires the sample to be irradiated with x-rays at different angles. Powder diffraction is used as it assumes that a fraction of crystals are in the correct orientation to give rise to diffraction. As the X-rays strike the atom they are scattered by the electrons. If the scattering atoms are arranged symmetrically with a

separation, these refracted waves will be in phase only in directions where their path-length difference, 2d sin Θ, equals an integer multiple of the wavelength. In this equation d represents the spacing between diffracting planes and Θ is the incident angle of the x-rays. This means that as the angle of the x-rays changes, so does the path-length. This means the peaks change at different angles due to the path-length not always being equal to 2d sin Θ.[28]

For hydrotalcite-type compounds this technique is useful to compare the crystalline structure of each sample and to get an idea of which conditions give better properties. This can be seen by the patterns that are produced. Substances with smaller crystalline domains will have wider peaks with amorphous material showing no reflections at all, however highly crystalline substances will have sharp peaks.[119] The XRD patterns have been well researched [86, 90, 92, 97] so it can be used to ascertain if the sample is indeed a hydrotalcite and not a mixture of oxides

X-ray diffraction patterns were collected using a Bruker D8 Advance X-Ray Diffractometer, operating in step scan mode, with Co Kα radiation (1.78897Å). Patterns were collected in the range 5 to 75° 2θ with a step size of 0.02° and a rate of 0.2s per step. Samples were crushed into a powdered form. The reflection positions were refined and calculated using the Celref v3.[92]

Inductively coupled plasma - optical emission spectroscopy (ICP-OES) is a technique for identifying elements and the concentrations of those elements within a material. While it is compatible for use with most elements in the periodic table, it is mostly used to quantify metal concentrations.[120, 121] The technique consists of two parts; the first being an inductively coupled plasma torch. The torch is comprised of three concentric quartz glass tubes through which the plasma gas flows. These tubes

are surrounded by a work coil of a radio frequency generator.[121] Argon gas is flowed through the tube and is ignited by a Tesla unit to initiate ionisation. The argon is then ionised in the electromagnetic field generated by the coil.[122] Stable high temperature plasma of about 7000 K is generated by the inelastic collision between the neutral argon atoms and charged particles.

A peristaltic pump delivers an aqueous or organic sample into a nebulizer where it is introduced directly inside the plasma flame.[121, 122] The sample immediately collides with the electrons and charged ions in the plasma, where it is broken down into ions.[120] As the various molecules break down the atoms lose and take up electrons within the plasma, radiation is given off at wavelengths that are unique to the elements involved. Emitted photons focused into a diffraction grating where they are separated according to wavelengths. The photon flux intensity is then measured by photomultiplier tubes positioned at specific wavelength. The intensity is indicative of the concentration of the elements at the characteristic wavelength within the samples.[123]

ICP-OES was performed by Exeter Analytical using a PE Optima 5300 Dual View ICP-OES Spectrometer. Samples were weighed to 6mg and placed into plastic microwave tubes and mixed with 5ml nitric acid (Analar grade) and 1ml hydrogen peroxide (Analar grade). The samples were digested using an Anton Paar Multiwave 3000 microwave digester. The microwave method typically lasts an hour and a half. A maximum temperature of 200°C is achieved. Solutions were ensured to be clear before transfer. The samples were then transferred to 50ml centrifuge tubes and 0.5ml of internal standard of yttrium added to each tube. The solutions were aliquoted to 50ml with de-ionised water. The samples were run against calibration

standards of known concentrations. The ICP-OES calibration used a curve from the standards, against which the intensity readings of the samples can be quantified. Standards containing 10, 30 and 50ppm of Al, Mg and Ni were used in this analysis.

CHN analysis derives its name from the three elements it is used for: carbon, hydrogen and nitrogen. The analysis uses combustion to break down the material. Analysis of carbon, hydrogen and nitrogen was performed by Exeter Analytical using a CE 440 Elemental Analyser. Samples were weighed around 1-2 mg and placed into a high temperature furnace. Once combusted in oxygen the products were passed through additional oxidation reagents to produce carbon dioxide, water, nitrogen and nitrogen oxides. The gases were then passed over copper to remove excess water and reduce the nitrogen oxides to elemental nitrogen. The detection of the combustion products was produced by using thermal conductivity detectors.

Raman spectroscopy relies on the Raman Effect, which occurs when the electromagnetic wave of light interacts with the electrons present in molecular bonds. The incident photons excite the molecule from a ground state to a virtual energy state. Primarily rotational and vibrational energy states are being excited, but phonon and acoustic vibrations are active for solids. When the molecule relaxes it emits a photon and it returns to a different energy state. The difference between the original ground state and the new energy state leads to the emitted photon's frequency being different to the frequency of the incident photon. If the emitted photon has a lower frequency than the incident photon then this is designated as a Stokes Shift. If emitted photon has a higher frequency then this is designated as an anti-Stokes shift. [28] This provides information on properties of material bond interactions of the elements.

Samples were placed on the stage of Olympus BX41 microscope, equipped with 10x and 50x objectives and were part of a Horiba LabRAM HR Raman microscope system, which also included a Synapse Horiba Jobin Yvon detector model 5828-0809 and a filter system. Raman spectra were excited by a neodymium-doped yttrium aluminium garnet (Nd:YAG) laser (532.8 nm). The spectrometer had a nominal resolution of 4-6 cm^{-1} in the range between 0 and 4000 cm^{-1}. Repeated acquisition using the highest magnification were accumulated to improve the signal to noise ratio. Spectra were calibrated using the 520.5 cm^{-1} line of a silicon wafer.

Nuclear Magnetic Resonance (NMR) spectroscopy is an analytical technique used for the determination of the content and purity of a sample, as well as the molecular structure. NMR is capable of analyzing mixtures containing both known compounds and unknown compounds. Being a well-researched analysis, many data tables and libraries of previous results are available to compare unknown results obtained during a spectroscopic analysis.[118] If a compound's molecular structure is already known, NMR can be used to determine the molecular conformation.

The principle behind NMR is that some nuclei have spin.[28, 118] This is when the total angular momentum of the nucleus equals +/- ½ and the effect creates a magnetic field. If an external magnetic field is applied, the magnetic fields of the spinning nuclei will either align with or against the external field. Eventually all the nuclear spins will align with the external magnetic field, as it is the lowest energetic state and therefore more favorable. When a radiofrequency is passed through a sample an energy transfer is possible between the base energy to a higher energy level. The precise resonant frequency of the energy transition is dependent on the effective magnetic field of the nucleus. This field is affected by the electron

shielding which is in turn dependent on the chemical environment. [118, 124] As a result, information about the nucleus' chemical environment can be derived from its resonant frequency. In general, the more electronegative the nucleus is, the higher the resonant frequency.[118, 124]

Single pulse ^{27}Al Magic Angle Spinning (MAS) was performed on a 14.1 Tesla Bruker Avance II+ spectrometer (600 MHz for ^{1}H) operating at a Larmor frequency of 156.34 MHz These measurements utilised a 3.2 mm HX Bruker probe which enabled a MAS frequency of 20 kHz. The flip angle calibration was performed on 1.1 M $Al(NO_3)_3$ from which a 'non-selective' (solution) $\pi/2$ pulse time of 9 μs was measured. This corresponded to a 'selective' (solid) pulse time of 3 μs for the $I = 5/2$ ^{27}Al nucleus. All measurements were undertaken with a $\pi/6$ tip angle to ensure all sites are excited evenly. All ^{27}Al shifts were reported against the IUPAC recommended primary reference of 1.1 M $Al(NO_3)_3$ in D_2O. [125] A common relaxation time of 0.5 s was deemed to be sufficient for all ^{27}Al measurements. To prepare the samples for insert into the 3.2 MAS rotor, samples were ground in an agate pestle and mortar until a fine powder was achieved. This resulting powder was then packed into a 3.2 mm Bruker MAS rotor and the single pulse ^{27}Al MAS experiments were performed.

Porosimetry is an analytical technique used to determine various quantifiable aspects of a material's porous nature, such as pore diameter, total pore volume, surface area, bulk and absolute density. This is achieved by making a series of calculations using data on nitrogen adsorption isotherms at liquid nitrogen temperature; BET, BJH and de Boer t-Plot were applied.

The method of Brunauer, Emmet and Teller (BET) is employed to determine surface area on a model of adsorption which incorporates multilayer coverage.

$$\frac{P}{V_a(P_0 - P)} = \frac{1}{V_m C} + \frac{C-1}{V_m C}\frac{P}{P_0}$$

In this equation, P and P_0 are the equilibrium and saturation pressure, respectively, of the adsorbates at the temperature of adsorption, V_a is the adsorbed gas quantity corresponding to an equilibrium pressure (P), V_m is the volume corresponding to monolayer coverage and C is a constant which is large when the enthalpy of desorption from a monolayer is large compared with the enthalpy of vaporisation of the liquid adsorbate.[28]

The method of Barrett, Joyner and Halenda (BJH) is a procedure for calculating the pore size distribution from experimental isotherms using the Kelvin model of pore filling. It applies only to mesoporous and small macropore size range.

$$v_{ads}(x_k) = \sum_{i=1}^{k} \Delta V_i(r_i \leq r_c(x_k)) + \sum_{i=k+1}^{n} \Delta S_i \, t_i(r_i > r_c(x_k))$$

In this formula, $v_{ads}(x_k)$ is the volume of adsorbate at relative pressure x_k. V corresponds to the pore volume, S is surface area and t is the thickness of adsorbed layer. This formula says, that the adsorbed amount at k-th point of adsorption isotherm may be divided into 2 distinct parts: 1st is a volume in condensate in all pores smaller than some characteristic size depending on current relative pressure, $r_c(x_k)$, 2nd is a volume of adsorbed film on all larger pores, calculated a sum of terms: Σ (pore surface) (thickness of film in pore).

The Kelvin equation describes the change in vapour pressure due to a curved liquid-vapour interface and is used to describe the meniscus that forms in capillary condensation. Vapour condensation in a capillary occurs below the saturation pressure due to an increase in van der Waals interactions between the vapour phase molecules in the confined space. The Kelvin provides a relation for the difference between the actual vapour pressure and the saturation vapour pressure. The equation may be written in the form;

$$In\frac{P}{P_0} = -\frac{2\gamma V_m}{rRT}$$

where P is the is the actual vapour pressure, P_0 is the saturated vapour pressure, γ is the surface tension, V_m is the molar volume of the liquid, r is the radius of the pore, R is the universal gas constant and T is the temperature. [126]

The sorption instrument used was a Micromeritics ASAP 2020 Accelerated Surface Area and Porosimetry System, with software is ASAP 2020 v3.03. Calculations were performed by Ben Douglas in the Department of Chemistry, University of Warwick.

Samples were added to sample tubes which were then fitted with a glass filler rod and a seal frit. They were prepared by outgassing heating from room temperature to 150 C at 10 C/min whilst evacuating at a rate of 5 mm Hg/s, until a pressure of 10 mtorr (µm Hg) was achieved. The temperature was then increased to 200 C (at 10 C/min) and held for 1 hour. The sample was then cooled and the sample tube backfilled with nitrogen, and weighed to obtain the dry mass used in subsequent calculations. The cold and warm free space was measured automatically by filling the sample tube with helium prior to analysis.

The sample tube was immersed in a bath of liquid nitrogen, and fitted with an isothermal jacket to maintain the level of the cryogen around the tube. Full nitrogen adsorption isotherms were collected.

BET analyses were performed on adsorption data in the relative pressure range 0.06 to 0.26. BJH analyses were carried out on the adsorption branch from 0.29 – 1.00, and data from 0.92 – 0.1in the desorption branch.

Results and Discussion

X-Ray Diffraction

Hydrotalcites exhibit symmetric peaks in the low 2θ range. At high 2θ values the reflections become weaker and lose their symmetry.[92] The indices of reflection (003) and (006) are clearly identifiable with reflections at 11.1^{o} and 22.7^{o} respectively.[86] The reflections of (009) and (102) are overlapped producing a broader signal at 34.5^{o}.[86, 92] The (105) reflection is found at 38.6^{o} and reflection (108) is found at 45.8^{o}. [86] Two reflections of (110) and (113) can easily be identified at 60.3^{o} and 61.6^{o}. [86, 92]

The pattern produced by HTCF (Figure 7) did not correspond to pattern described above. While some of the required reflections were present, they were weak when compared with the addition reflections that had also appeared. In particular a reflection found at 30^{o} was prominent, however, it has yet to be definitively identified. It was concluded that while it did form some hydrotalcite the particles reacted further, producing a polymer-like substance. It was found that this could be

compensated for by flowing the product into water (HTCFw). The sample was excluded from further analysis for not being considered relevant to the project.

Both HTCB and HTCFw (Figures 6 and 8 respectively) did show the familiar XRD pattern described above and the intensity of the reflections were in a similar ratio to one another. The only difference of note was the reflections of HTCFw were broader; a broader signal would indicate smaller crystalline domains. For HTCF2h (Figure 12) the reflections at lower 2Θ remained at the same intensities relative to each other but the reflections at a higher 2Θ began to lose definition. With all required caution, overall reflex intensities were tentatively lower than those observed for HTCFw which are consistant with even smaller crystalline domains computed by the Scherrer equation below. For HTCF4h (Figure 13) the reflection (003) had been significantly reduced and definition of the reflection across the whole pattern had begun to degrade. The reason for this loss of definition became more apparent when this analysis was compared with the BET and BJH analyses. It was likely caused by the extended washing phase of its production. Also observed for HTCF2h and HTCF4h was a shift in the reflections to higher 2Θ.

Samples HTCFc, HTCFo and HTCFco (Figures 9-11 respectively) all produced patterns that displayed the indices indicative of a hydrotalcite structure. Yet these samples, especially the samples containing additional hydroxide, displayed reflections that were not typically seen with this structure. This would suggest that, like HTCF, additional reactions had taken place to form a polymer-like substance, as well as forming additional materials, which were formed by the altered concentrations of hydroxide and carbonate. It was decided that these samples were no longer considered relevant in the project; however they were used occasionally

for analysis as an additional comparison to shed more light on what was occurring. All further analyses that feature in this work will focus on the remaining four samples.

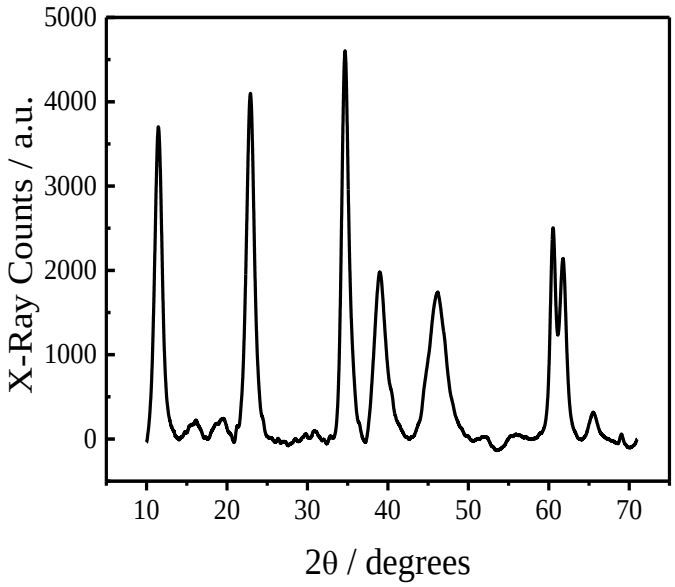

Figure 6. The X-ray diffraction pattern of the sample HTCB.

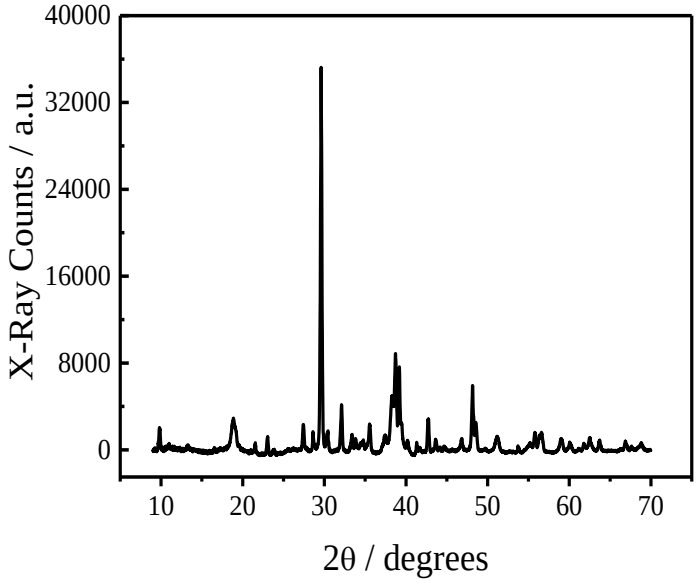

Figure 7. The X-ray diffraction pattern of the sample HTCF.

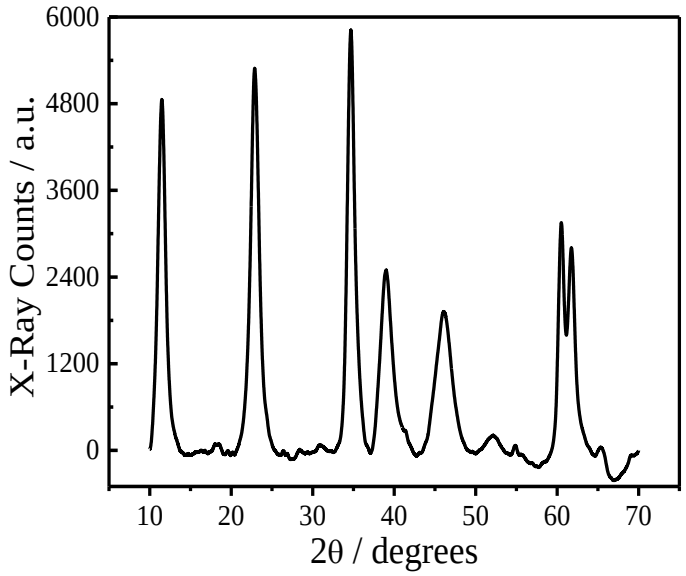

Figure 8. The X-ray diffraction pattern of the sample HTCFw.

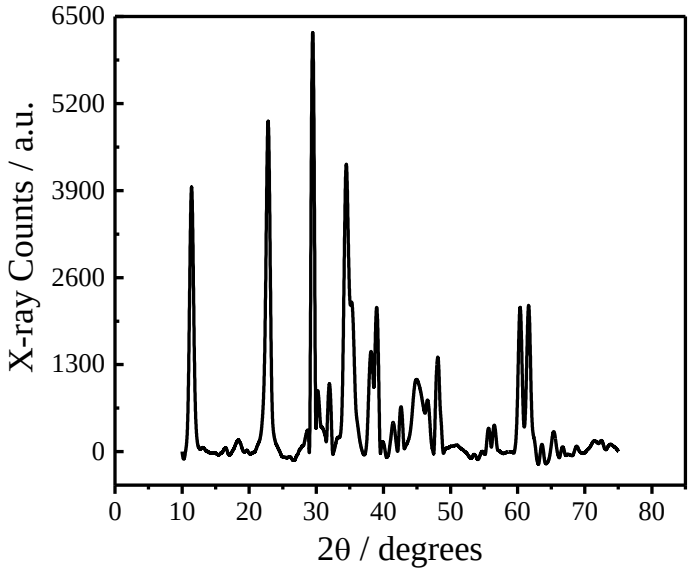

Figure 9. The X-ray diffraction pattern of the sample HTCFc.

.

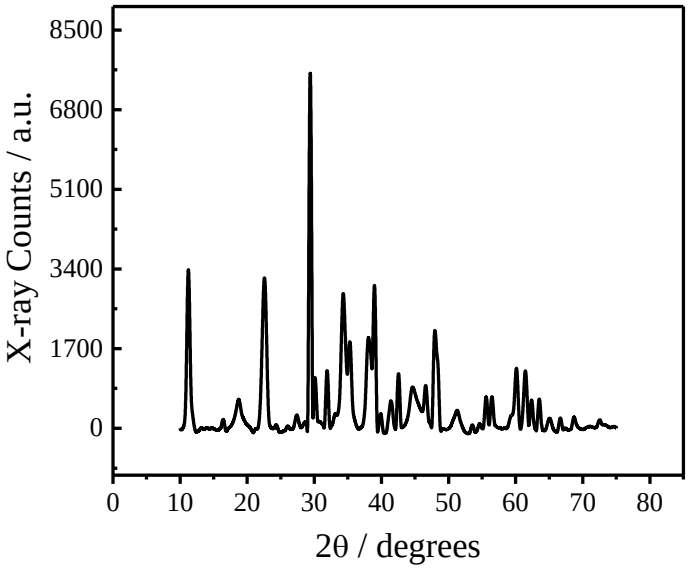

Figure 10. The X-ray diffraction pattern of the sample HTCFo.

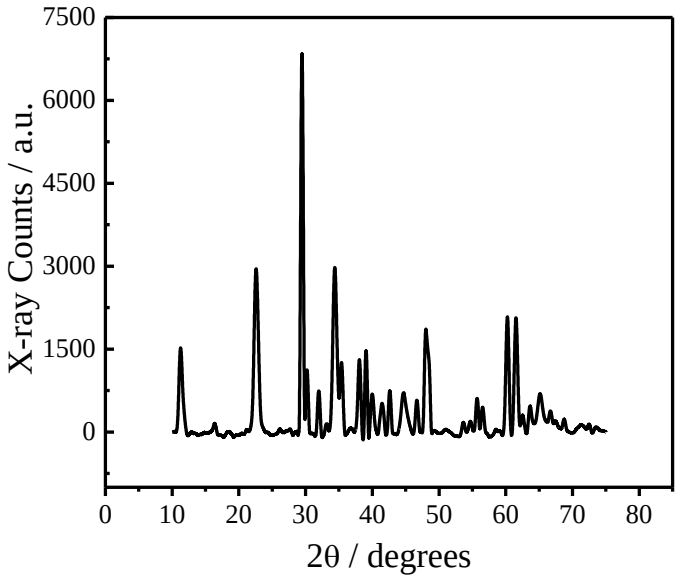

Figure 11. The X-ray diffraction pattern of the sample HTCFco.

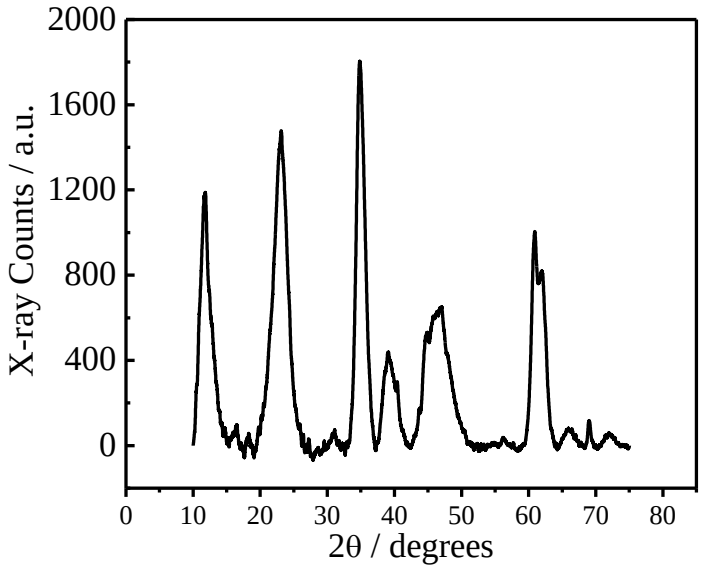

Figure 12. The X-ray diffraction pattern of the sample HTCF2h.

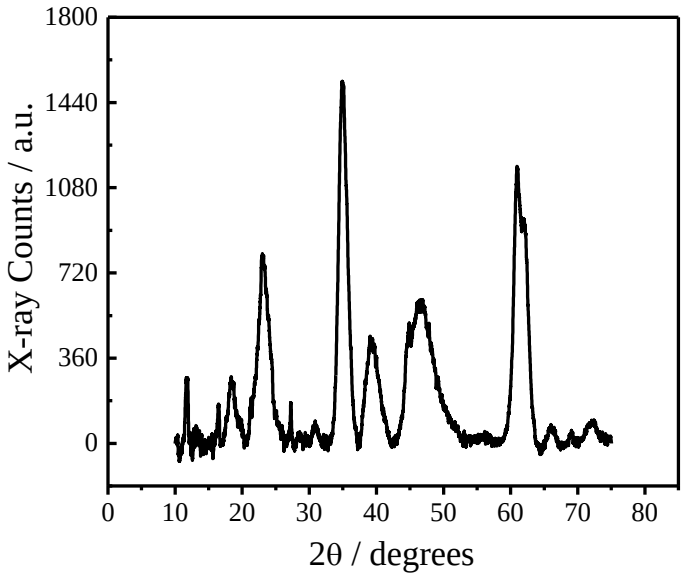

Figure 13. The X-ray diffraction pattern of the sample HTCF4h.

Table 4. Locations of the observed reflections for each of the samples.

Sample	Reflections hkl						
	003	006	009	105	108	110	113
HTCB	11.5	22.9	34.7	38.9	46.2	60.5	61.8
HTCFw	11.5	22.9	34.6	38.9	45.7	60.5	61.8
HTCFc	11.4	22.8	34.4	38.1	48.1	60.9	61.6
HTCFo	11.3	22.5	35.3	38.5	46.6	60.1	61.4
HTCFco	11.3	22.6	34.4	38.1	48.0	60.4	61.6
HTCF2h	11.6	23.0	34.7	39.1	45.9	60.9	62.1
HTCF4h	11.6	23.1	34.9	39.2	45.8	60.9	62.2

The cell parameters for hydrotalcite are represented by (a); the distance between the metal centres, and by (c); three times the interspatial gap between the lattice layers. Analysis of the XRD patterns yields values for a and c were consistent with the literature (see Tables 5). The crystallite size (L) was calculated using the Scherrer equation: [92]

$$L = \frac{K\lambda}{(\beta(\theta)cos\theta)}$$

where K is a dimensionless shape factor in this instance equal to 0.89, λ is the wavelength of the radiation used, $\beta(\Theta)$ is the full width at half maximum given in radians and Θ is the Bragg diffraction angle.

Cell parameters were calculated using the (003) reflection to find the c parameter and (105) reflections to find the a parameter. For HTCF4h the (006) reflection had to be used to find the c parameter due to the near disappearance of the (003) reflection. The parameters calculated from the X-ray diffraction patterns all showed similar distances between the metal centres (represented by the a parameter), which was neither affected by the different process methods or by the amount of time the material was washed for. The width of one lattice and one interspatial layer (represented by the c parameter) also remained consistent.

The sizes of the crystallites were larger in the HTCB and HTCFw samples than those reported in the literature. Overall HTCFo had the largest of the crystallites with HTCFc and HTCFco having larger sizes too. Since these samples are thought to have undergone additional reactions bonding particles together, it was assumed that this had caused the difference in crystallite size. Crystallites for HTCB were bigger than the crystallites of HTCFw but were not significantly bigger. Once the flow samples had been washed, the crystallite size was closer to those found in the literature. This would mean that the larger surface that were seen in the BET (below) were due to the degrading of the particle to from a more porous material, rather than the particle increasing in size.

Table 5. Cell parameters and crystallite sizes of the hydrotalcite samples synthesised in the batch and flow conditions

Sample	Cell Parameters (nm)			Crystallite Size (nm)
	a	b	c	
HTCB	0.31	0.31	2.33	7.16
HTCFw	0.31	0.31	2.35	6.84
HTCFc	0.31	0.31	2.32	11.9
HTCFo	0.32	0.32	2.36	14.6
HTCFco	0.31	0.31	2.34	11.6
HTCF2h	0.31	0.31	2.23	3.88
HTCF4h	0.32	0.32	2.26	3.67
Millage [92]	0.3	0.3	2.3	3.25
Miyata [93]	0.305	0.305	2.59	1.27
Costantino [94]	0.304	0.304	2.27	-
Zavoianu [95]	0.305	0.305	2.32	-
Cavani [63]	0.305	0.305	2.34	-

Inductively coupled plasma – optical emission spectroscopy (ICP-OES) / Carbon, hydrogen and nitrogen analysis (CHN)

The accepted formula for hydrotalcite is given as $Mg_6Al_2(OH)_{16}CO_3 \cdot 4H_2O$.[63, 64] It would be expected that the results of ICP and CHN analysis would give a formula similar to this with some nitrate impurity due to the reagents used.

The main difference between HTCB and HTCFw was the percentage of the nitrate impurity. Nitrate stems from the reagents, being the counter anion to magnesium and aluminium. In HTCB, little nitrate was detected in the compound, while a significantly higher amount was found in HTCFw. The nitrate content was mostly removed by washing leaving its concentrations lower than that in HTCB. Washing, however, was shown to also reduce the Mg:Al ratio. For all other samples the ratio was close to 3:1. The washed samples showed ratios of 1.7:1 and 2.1:1 (see Table 6). As seen below in the space/time yields, yields decreased for the washed samples. When comparing the data in Table 6 with the X-ray diffraction data and the BJH data it was concluded that the decrease in Mg:Al ratio seen after 2 hrs was likely due to the dissolution of magnesium into the washing water, from the lattices nearer the surface of the particles. The increase in ratio after 4 hrs was thought to be due to the loss of both magnesium and aluminium the lattices further dissolved in the washing water.

The samples produced in flow showed a surprising affinity for monovalent anions. With exception of washed flow samples all showed an increased percentage of nitrate anions. Possible reasons are discussed in later analysis. The remaining percentage not represented by these two analytical techniques was consistent with what would be expected to be seen by the percentage of oxygen contained in both the lattice and counter anion layer.

Table 6. Result of ICP and CHN analysis for hydrotalcites synthesised in both batch and flow.

	ICP		CHN			Mg/Al ratio
	Mg (%)	Al (%)	C (%)	H (%)	N (%)	
HTCB	22.09	8.46	1.96	3.74	0.83	2.9:1
HTCFw	17.67	6.93	1.54	2.95	3.32	2.9:1
HTCF2h	16.08	10.36	2.71	3.48	0.24	1.7:1
HTCF4h	17.33	9.35	2.87	3.53	0.03	2.1:1

Using these values it was possible to gain an idea of the general formula of the samples made (Table 7);

Table 7. A Table of the proposed formulas for the hydrotalcite samples.

Sample	Formula
HTCB	$Mg_6Al_2(CO_3)(OH)_{16}\cdot 3.5H_2O$
HTCFw	$Mg_6Al_2(CO_3)(OH)_{15}(NO_3)\cdot 3.5H_2O$
HTCF2h	$Mg_3Al_2(CO_3)(OH)_{10}\cdot 2.5H_2O$
HTCF4h	$Mg_3Al_2(CO_3)(OH)_{10}\cdot 2.5H_2O$

Raman Spectroscopy

The literature (Table 7) on Raman analysis indicates vibration bands related to metal oxygen bonds involving both aluminium and magnesium. It is expected to see the bonds to carbonate and the nitrate, when nitrate is present.

The band seen at 484 cm^{-1} was attributed to the vibrations of Al-O-Al. [90] Due to the repulsion of positive charge, aluminium atoms within the lattice are kept as far from

each other as possible. With a Mg:Al ratio 3:1 it was unlikely that an Al-O-Al bond would appear within the lattice itself. It was then assumed that these Raman bands are likely representing the excitation of the vibration of the bonds between the lattice layers. Being the centres of the charge imbalance, it is rational to assume it is at the aluminium cations where counter anions would be attracted to and link the layers together at adjacent aluminium cations. The band at 557 cm^{-1} corresponded to the vibrations in hydrotalcites of Al-O-Mg. [90] The band found at 717 cm^{-1} was assigned as ν4 bending mode of free nitrate anions, while the bands at 1043 cm^{-1} was assigned at the ν1 mode of the same free nitrate anion. [87, 109] The band at 1058 cm^{-1} was assigned to the vibrations of the ν1 mode of free carbonate anion. [90, 102] The band seen 1068 cm^{-1} was assigned to carbonate anions bound to water within the hydrotalcite layers. [90, 102] The band seen at 1085 cm^{-1} was assigned to the ν1 carbonate anions that are chemically bonded to the hydroxyl surface of the lattice layers. [90, 102]

Table 8. Band assignments in typically hydrotalcite Raman spectra

Wavenumber (cm^{-1})	Assigned Bond
484	Al-O-Al.
557	Al-O-Mg
717	ν4 bending mode free nitrate anions
1043	ν1 mode of the same free nitrate anion
1058	ν1 mode of free carbonate anion
1068	carbonate anions bound to water within the hydrotalcite layers
1085	ν1 carbonate anions that are chemically bonded to the lattice layers
1383	bicarbonate anions

The bands seen between 474 and 481 cm^{-1} on all the samples were assigned to the aluminium that is linked together by oxygen (Al-O-Al) as would likely be found in the lattice. [90] The bands for the aluminium linked to magnesium by oxygen (Al-O-Mg) are found between 547 and 559 cm^{-1}. [90] Vibrations associated with the bonds of magnesium linked to magnesium by oxygen were not seen by the Raman. The bands at 718 and 723 cm^{-1} were assigned to the ν4 mode of nitrate anions [87, 109] and the ν1 mode of the nitrates were found at 1041 and 1049 cm^{-1} [87, 109] The latter nitrate bands were not seen for the washed flow samples. This was expected since CHN analysis showed that washing removed the nitrates from the material (see Figures 16 and 17). The ν1 symmetrical stretching mode of carbonate in was assigned between 1051 and 1074 cm^{-1} [90, 102, 127] with the unwashed flow sample (HTCFw see Figure 15) displaying the higher band frequency. HTCFw also show bands between 1083 and 1085 cm^{-1} which was assigned to carbonate anions bound directly to the lattice layer [90, 102] This sample also displayed bands at 1383 cm^{-1} and this band was assigned to bicarbonate anions (see Figure 18). The samples HTCFc, HTCFo and HTCFco (Figure 19) were also unwashed flow samples and they too displayed the bicarbonate band. When Raman spectroscopy results were related to CHN analysis data it was observed that samples that remained unwashed, after being produced in a flow process, bonded with more nitrate and bonded with the carbonate as monovalent anions.

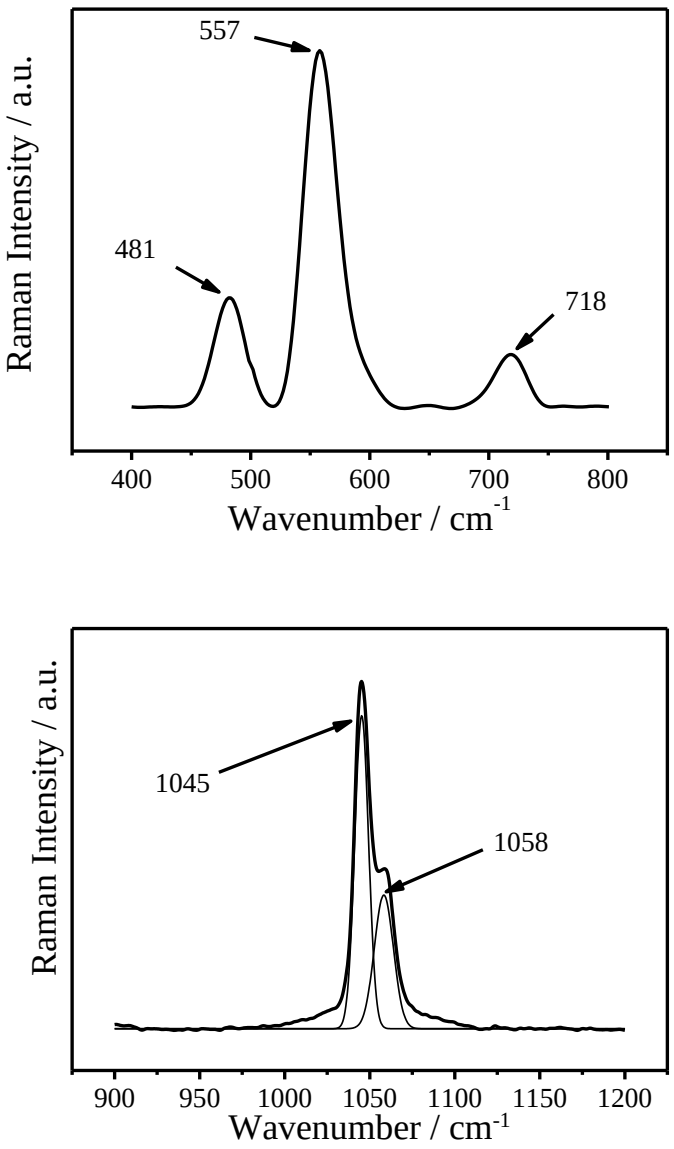

Figure 14. Raman spectra for hydrotalcite HTCB. The spectra display the metal-oxygen peaks (above) and the carbonate peaks (below).

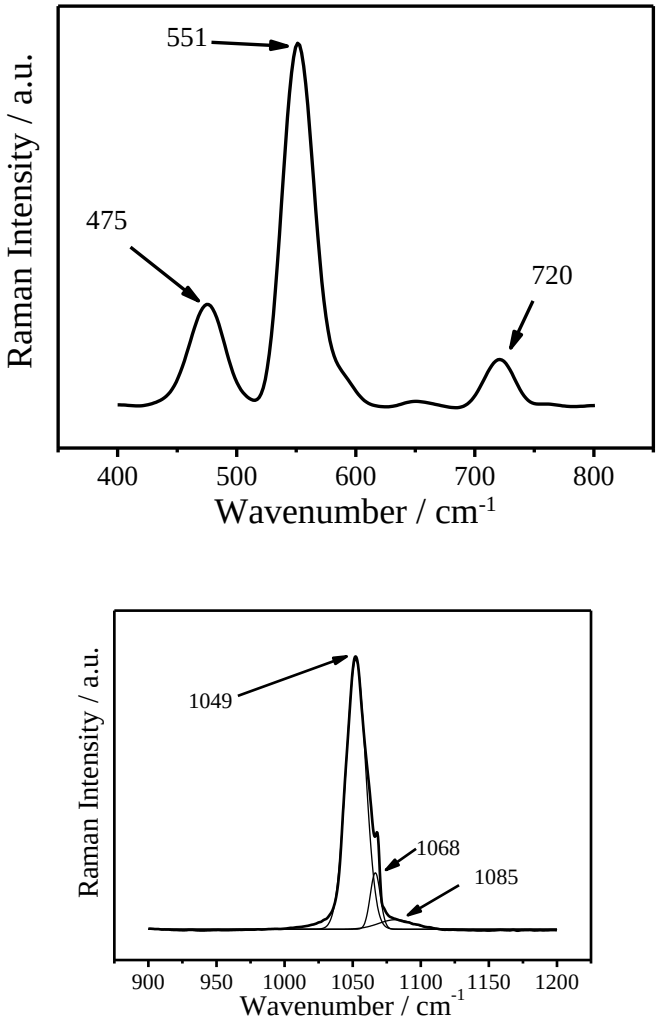

Figure 15. Raman spectra for hydrotalcites HTCFw. The spectra display the metal-oxygen peaks (above) and the carbonate peaks (below).

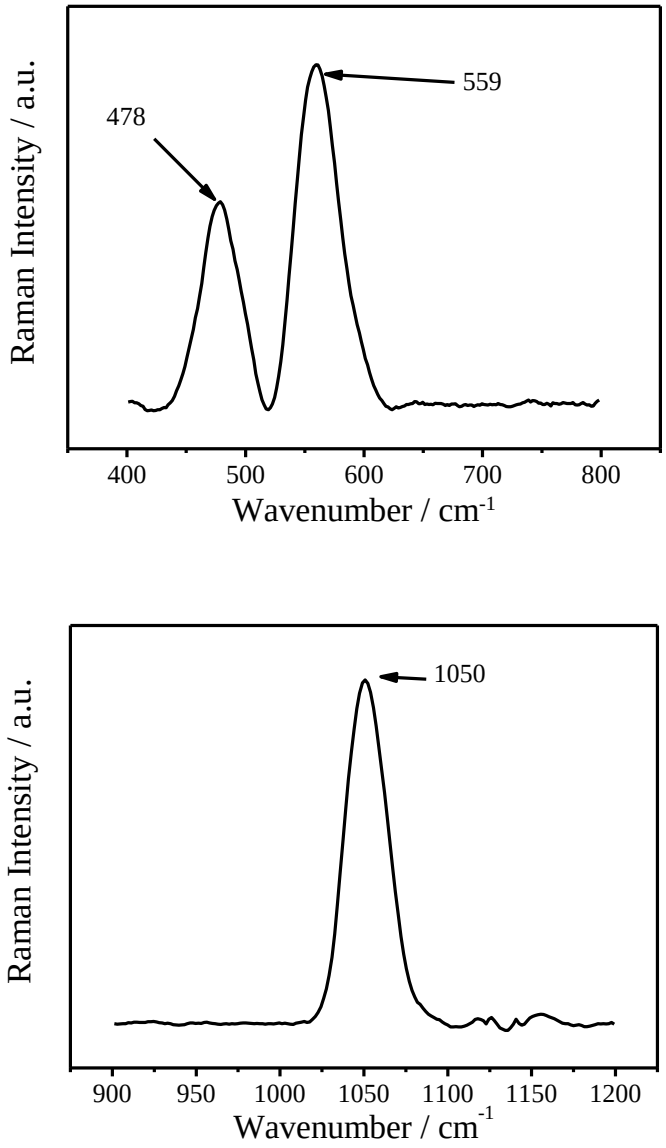

Figure 16. Raman spectra for hydrotalcites HTCF2h. The spectra display the metal-oxygen peaks (above) and the carbonate peaks (below).

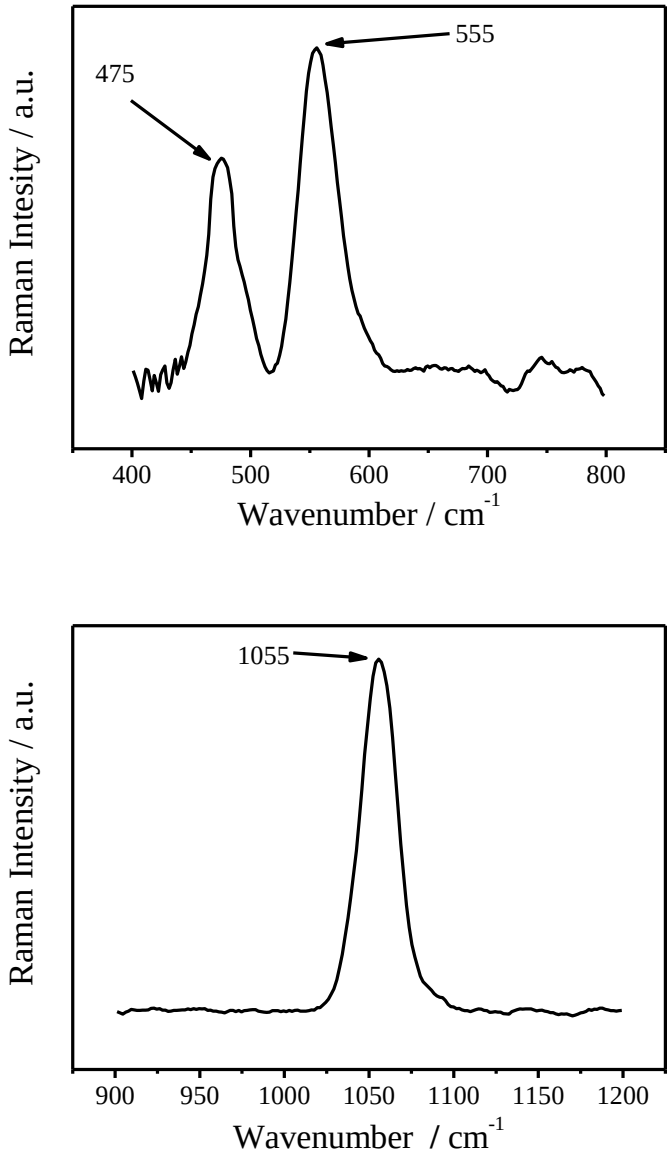

Figure 17. Raman spectra for hydrotalcites HTCF4h. The spectra display the metal-oxygen peaks (above) and the carbonate peaks (below).

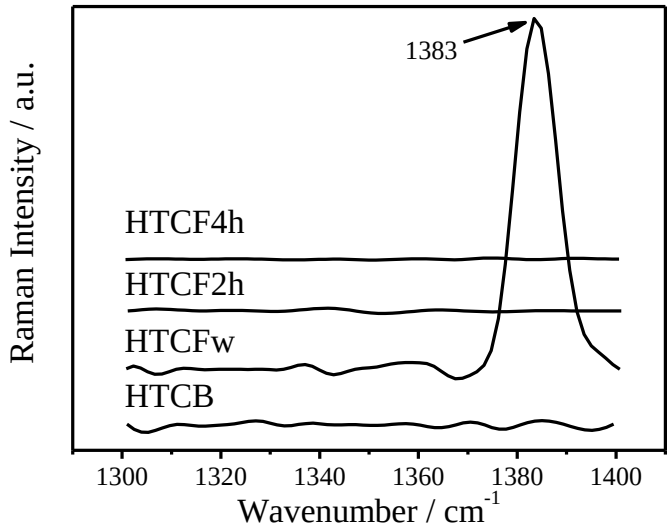

Figure 18. The Raman spectra of the bicarbonate vibration range for HTCB, HTCFw, HTCF2h and HTCF4h.

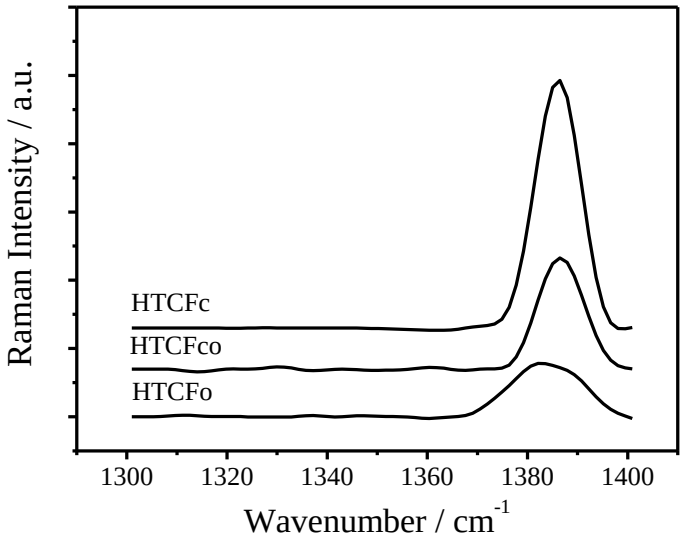

Figure 19. The Raman spectra of the bicarbonate vibration range for HTCFc, HTCFco and HTCFo.

Aluminium Nuclear^{27} Magnetic Resonance

The environment of the dominating aluminium species detected at 9.7 ppm was similar for all of the samples regardless the methods of preparation (Figure 20 and 21). The position of the peak showed the aluminium to be six coordinated in the octahedral position. [74, 98, 128-130] However, there was a clear broadening towards the lower chemical shift observed for washed samples, which was especially pronounced for the HTCF2h material. The broadening was most pronounced in samples showing the strongest deviation from the ideal Mg/Al ratio of 3. The most likely explanation was the formation of an X-ray amorphous alumina rich species due to washing of the samples. Washing out the aluminium element of the lattice would be harder to do due to aluminium acting as a bridge between the layers. This would encourage magnesium oxide to be washed out first, leaving the surface aluminium oxide rich. This change in the surface condition would not be registered by XRD as aluminium oxide is amorphous. Aluminium coordination in the latter nano sized cluster was obviously octahedral. Most likely the latter species was located close to the sample surface. The findings suggest that regardless of the process used in the production of the hydrotalcite the aluminium always functioned in a similar manner. The coordination number further supported the idea that aluminium was bonded to the counter anions found in the interspatial layer and acts as a bridge when the aluminium in opposing layers align. Washing leads to modification such that clusters (or pillars) of octahedral coordinated aluminium forming upon the depletion of magnesium. More extended washing finally resulted in partial dissolution of the aluminium rich clusters (or pillars).[131]

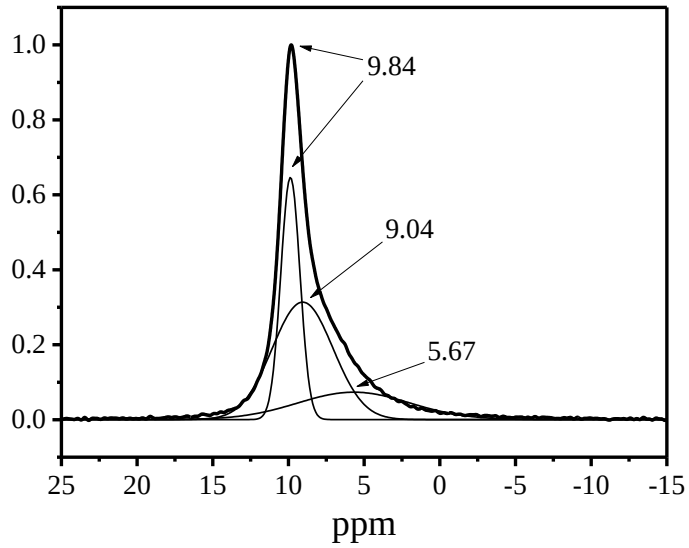

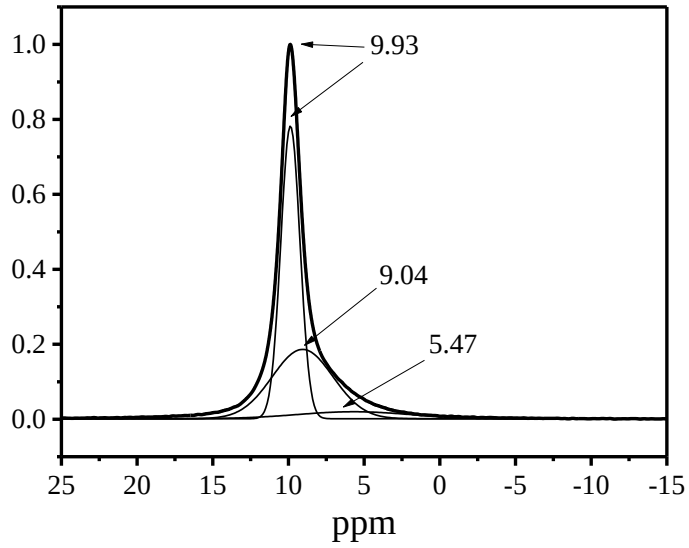

Figure 20. Al-NMR of HTCB (top) and HTCFw (bottom), showing the environments of the aluminium and the anions coordinated to it.

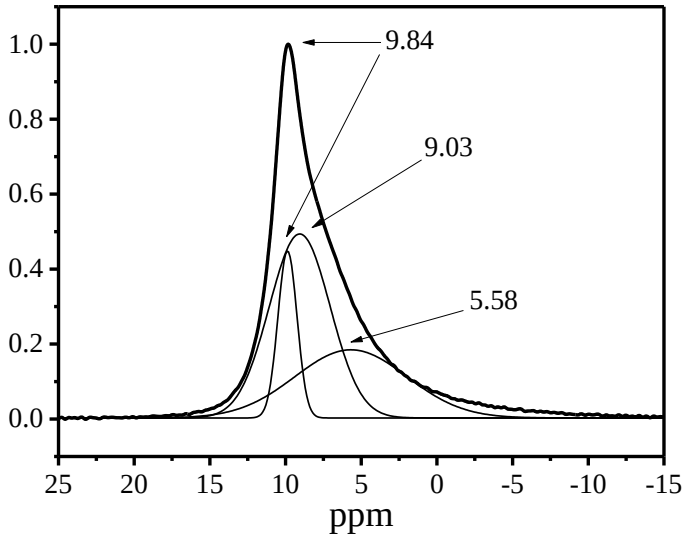

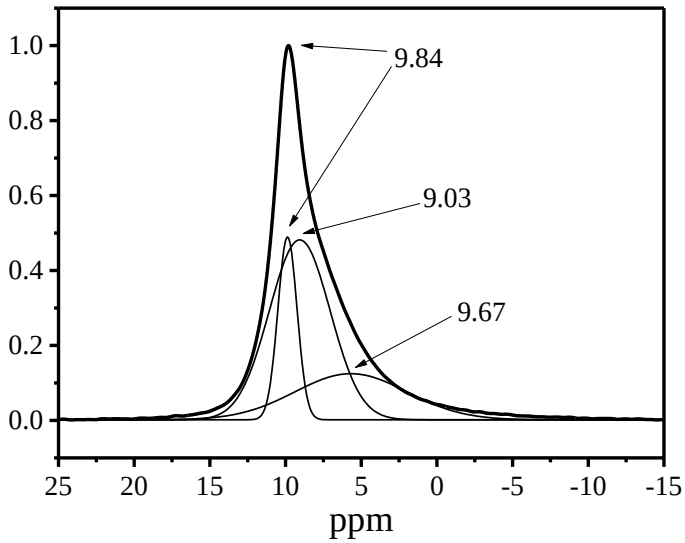

Figure 21. Al-NMR of HTCF2h (left) and (HTCF4h), showing the environments of aluminium and its coordination.

Surface area and pore size distribution analysis

The samples produced in batch and flow processes displayed a Type IV isotherm. A Type IV isotherm displays the same adsorption as a Type II isotherm. A Type II isotherm is obtained by adsorption on non-porous or macroporous powders. It represents unrestricted monolayer-multilayer adsorption on a heterogeneous substrate. These layers may exist simultaneously at different layers, but a monolayer completion is assumed if a point of inflection is observed (point B in figures 22-25). [132] Type IV differs from Type II when the desorption branch follows a different path to the adsorption branch forming a hysteresis. As the relative pressure approaches 0.4 the desorption branch closes on the adsorption branch. The hysteresis is attributed to capillary pores from which molecules of the adsorbed gas do not desorb as readily as they are adsorbed. This is due to a vapour lowering over a concave meniscus formed by the condensed liquid in the pore. Type IV isotherms are commonly found with many mesoporous adsorbents.[76, 132]

The larger surface area of HTCB (Table 8 and Figure 22) would indicate that the material had macropores but the hysteresis indicates mesopores were also in its structure. The small surface area of HTCFw (Figure 23) would suggest that this material did not have the same macropores found in HTCB. The hysteresis was more pronounced in the flow material indicating that the mesopores were present in the structure. The conditions of sample pre-treatment in nitrogen physisorption were optimized to maintain sample integrity. It was intended to clear the pore structure from residual water without major release of carbon dioxide which was involved in the inter-layer assembly. As a result of optimisation, outgassing was performed under vacuum at 200°C for 1h. However, as will be shown in Chapter 3 there was

already slight thermal decomposition of the hydrotalcite observed at 200°C through TGA and DTA. Water removal from the structure occurred between ambient and 250°C with the DTA trace not returning to zero. For that reason, it was possible that the outgassing of HTCFw led to the formation of a weakened structure only stable under vacuum. This structure was then completely or partially collapsed upon raising the nitrogen to atmospheric pressure during the sorption experiment. It is interesting to note the degree of collapse scaled with extent of the hysteresis observed between the adsorption and desorption branch. As the hysteresis increased so too did the degree of collapse that was observed. Tentatively, capillary forces seem to be important in the decline of the surface area, resulting in the desorption branch ending with a lower amount of nitrogen being adsorbed.

HTCF2h (Figure 24) exhibited a surface area increase to an area larger than the batch samples and displayed an isotherm much closer related to a Type II isotherm. Due to the loss of the nitrates and the magnesium in the washing process, the mesopores of the material were opened up becoming macropores. This is evident by the hysteresis being nearly completely removed. The surface area for HTCF4h (Figure 25) had decreased again by nearly half. Most likely the above quoted delayed dissolution of aluminium rich pillars had led to a partial collapse of the macroporous structure. As a result, the remaining material showed a lower degree of crystallinity as confirmed in the x-ray diffraction (above) where corrosion in the crystal structure was observed and the crystallite size decreased.

Table 9. Information derived from the surface area analysis.

BET Surface Area (m^2/g)			
HTCB	HTCFw	HTCF2h	HTCF4h
48	5	98	55

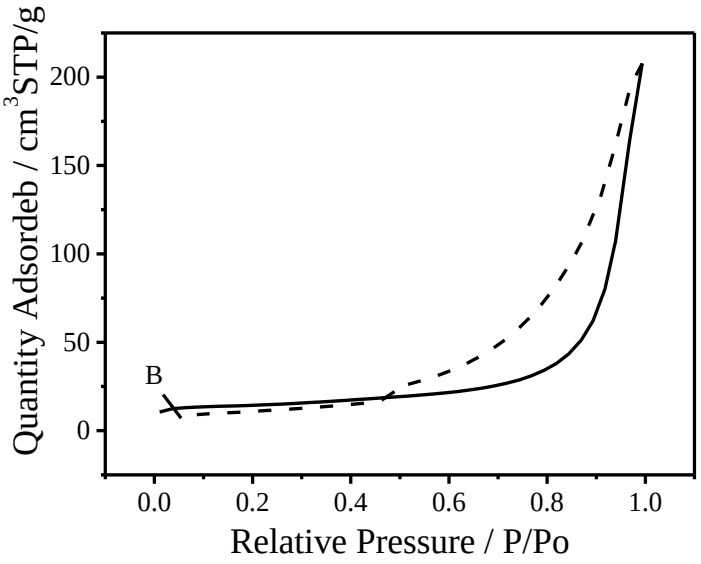

Figure 22. Isotherm for HTCB. Adsorption (solid line) and desorption (dashed line)

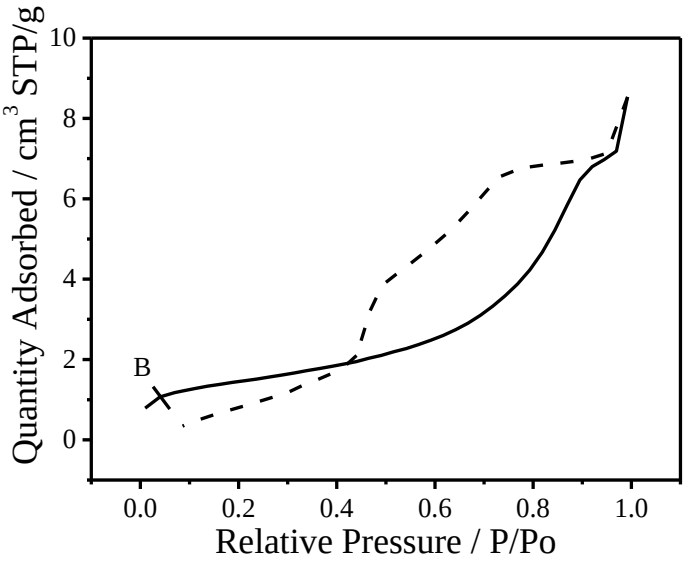

Figure 23. Isotherm for HTCFw. Adsorption (solid line) and desorption (dashed line)

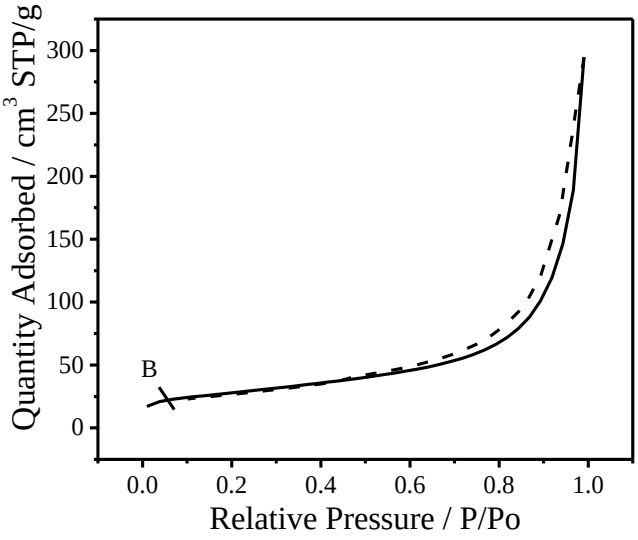

Figure 24. Isotherm for HTCF2h. Adsorption (solid line) and desorption (dashed line)

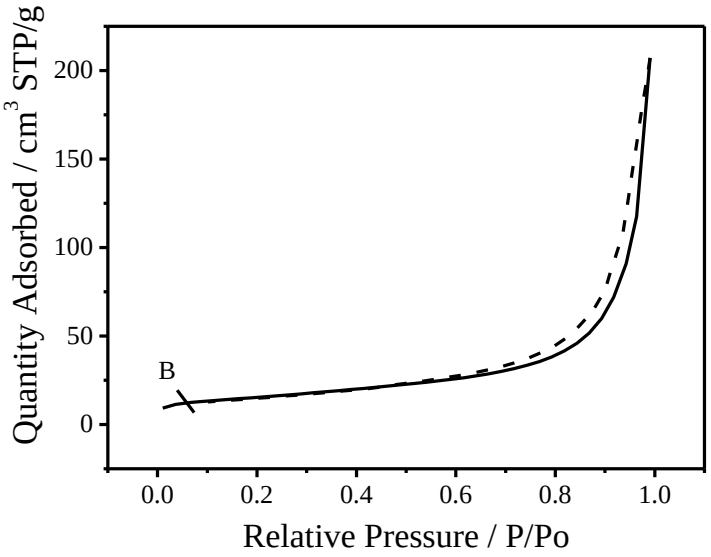

Figure 25. Isotherm for HTCF4h. Adsorption (solid line) and desorption (dashed line)

BJH analysis was used to determine the pore volume and the distribution of the size. HTCB had a peak width 28 nm with a cumulative pore volume of 0.21 cm^3 g^{-1}. HTCFw had pores that were much smaller than batch. The peak width the pore was 12 nm and had a volume of 0.0068 cm^3 g^{-1}. This would support the idea that HTCFw only had mesopores which were the cause of the hysteresis. The lack of macropores resulted in the lower surface area.

The washed flow samples displayed similar distribution to each other and closer to HTCB. For HTC2h the distribution reached a diameter of 21 nm with a volume of 0.15 cm^3 g^{-1}. HTCF4h reached a diameter of 21 nm with a volume of 0.09 cm^3 g^{-1}. The difference between the samples washed for 2 h and 4h was seen in the pore volume. The samples washed for 4 h had the same range as the samples washed for 2 h but the volume for all the pores was reduced. In the x-ray diffraction (above) the crystallite size of the sample was seen to reduce with the longer washing, also

evident was the loss of the (003) reflection. This would suggest that the surface of the sample had been further corroded by the washing process.

Table 10. Information derived from the pore size distribution analysis.

BJH Adsorption cumulative surface area of pores between 1.7 and 300 nm diameter (m^2/g)			
Batch	Flow	2hrs	4hrs
50	5	90	56
BJH Desorption cumulative surface area of pores between 1.7 and 300 nm diameter (m^2/g)			
Batch	Flow	2hrs	4hrs
110	11	111	64

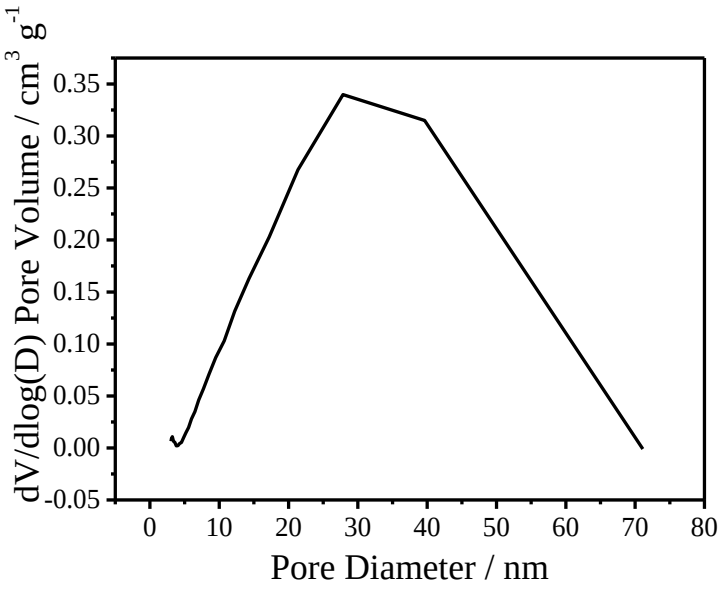

Figure 26. BJH Plot showing the distribution of the pore size for HTCB.

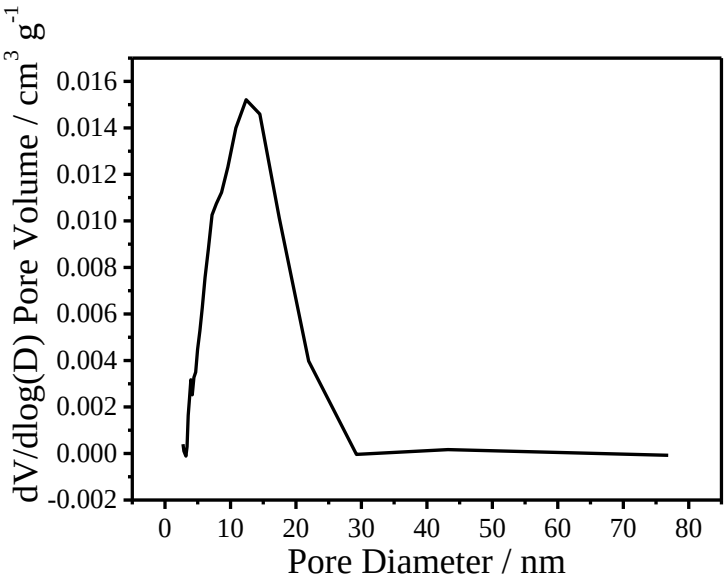

Figure 27. BJH Plot showing the distribution of the pore size for HTCFw.

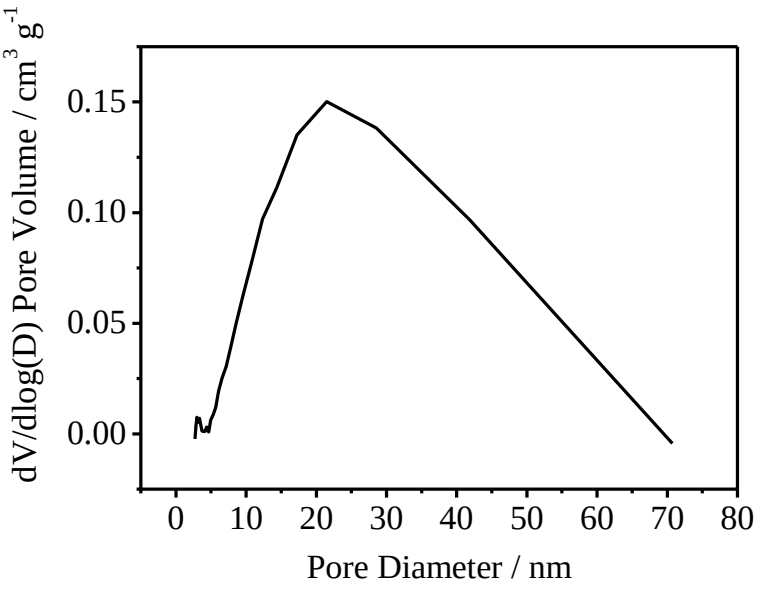

Figure 28. BJH Plot showing the distribution of the pore size for HTCF2h.

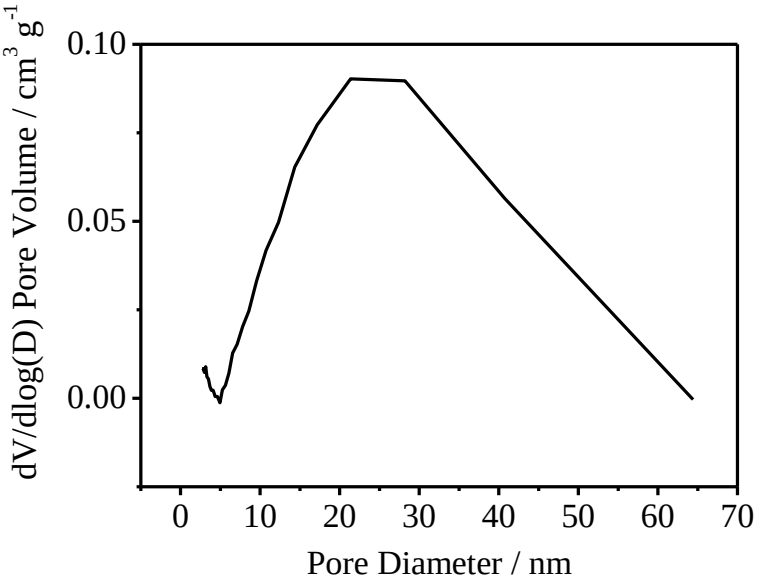

Figure 29. BJH Plot showing the distribution of the pore size for HTCF4h.

Space-time Yield

Productivity of batch and continuous reactors was compared on the basis of obtained mass of dried product using the corresponding batch and continuous optimised protocols. [133] The calculation of STY for the flow process was based on the amount of product collected over the stated period of time at the given total feed flow rate.

$$STY = \frac{mass\ of\ product(kg)}{time(h) \times volume\ of\ reactor\ (m^3)}$$

For the batch method the value of time (h) included the time taken for the reaction, the time taken for ageing. The volume of the reactor (m^3) was only the volume of the batch reactor. For the flow method the value of time (h) included the time taken for the reaction and any time taken to wash the sample. While the volume (m^3) included

the flow reactor and the volume of water needed to quench the reaction. Separate results were calculated to include drying as all samples required a similar time.

Table 11. Space-time yields for both batch and flow processes.

Method	Mass of product (kg)	Reactor volume (m^3)	Reaction Time (h)	STY ($kg\ h^{-1}\ m^{-3}$)
HTCB	0.016 ± 0.0015	0.000763	1.50	14.09 ± 0.97
HTCFw	0.0019 ± 0.0006	0.0001	0.12	147 ± 39
HTCF2h	0.0011 ± 0.0001	0.0001	2.12	5.21 ± 0.49
HTCF4h	0.0009 ± 0.0001	0.0001	4.12	2.18 ± 0.24
Space-time yield accounting for solid handling				
HTCB	0.0166	0.000763	13.50	1.55 ± 0.094
HTCFw	0.0017	0.0001	12.12	1.46 ± 0.39
HTCF2h	0.0011	0.0001	14.12	0.78 ± 0.07
HTCF4h	0.0011	0.0001	16.12	0.65 ± 0.06

For the production of a wet product the flow produced samples were by far more efficient. It achieved a space time yield that was nearly sixty times greater than that obtained in a batch process. These results for flow were dependent on the flow rate of the pump. Due the fast rate of reaction it may be possible to produce higher space time yields with faster flow rates. These results were obtained by the method described in the materials preparation section above. As was expected, the space

time yield for the flow made samples dropped dramatically when washing was introduced, reducing the efficiency to less than the batch samples. It was also of note that the mass yields drop too as product was lost in the washing process. Inclusion of the drying time showed a sharp reduction in the space time yield for all samples. The batch samples became more efficient as the flow samples were slowed down to a more comparable rate.

Conclusion

HTCB is made by a co-precipitation method with a period of ageing involved. With all the materials in the same place particles form by precipitating and dissolving in order to achieve the material with the lowest energy configuration. This arrangement has two aluminium species, in opposite lattices, adjacent to each other (see Figure 27). In this work this position will be referred to as “in phase”. In this arrangement anion affinity has been found to be based on size of the ion and its associated charge. Therefore divalent anions have a higher affinity than monovalent anion and will be more likely to participate in ion exchange reactions linking the lattices together forming the layered structure.[90] This is seen in the CHN analyses where the nitrogen percentage is low relative to carbon. Due to the constant precipitating and dissolution, the material is able to form a meixnerite ($Mg_6Al_2(OH)_{18}\cdot 4(H_2O)$) intermediate.[134] When the material has two aluminium “in phase” with each other, the intermediate then introduces the carbonate ions to form hydrotalcite.[134]

Comparing flow synthesis (HTCFw) to batch preparation (HTCB) reagents have shortened reaction time to precipitate and dissolve to the lowest energy forms. As a

consequence products adopt readily accessible but energetically less favourable forms. In this method, aluminium in the meixnerite intermediate is placed randomly. The aluminium that is “in phase” become so through probability, not because of preference. When the aluminium is “out of phase” bicarbonate (see Figure 30) still binds to aluminium but bicarbonate cannot locally balance its charge with a second aluminium to form the more favourable layer bridging carbonate anion. The presence of bicarbonate is seen in the Raman spectroscopy. Since the amounts of carbonate and hydroxide reagents are fixed to proportions in an ideal structure, this would leave some aluminium without carbonate to bind to. In the absence of the bridging configuration making use of the divalent anion the remaining aluminium takes up the monovalent nitrate anion as shown by the large nitrate peak of the Raman spectroscopy and the CHN which shows a large increase in the amount of nitrate. The loss of the bridging carbonate would result in a less stable layering, which is seen in the broader reflections of the x-ray diffraction pattern. Hydroxide would be more favourable in this position but it is used up in the formation of the lattice. [135, 136] Some aluminium species will be found in the “in phase” arrangement and in these cases the carbonate still bridges the layers together allowing it to retain its crystal structure seen in the XRD.

The above reasoning can be supported by kinetic considerations on the precipitation process. Presence of nitrate shows that part of the metal reagent remained at least partially in nitrate form rather than being full converted to the hydrotalcite solid. Formation of a solid with extensive nitrate residues at short reaction time (continuous preparation) indicates the rate of lattice building being at least as high as the rate to convert nitrate reagents to the hydroxyl intermediates. Comparing samples made with increased starting reagent concentration, shows the highest bicarbonate

band intensity for all the materials prepared was produced by the sample with doubled carbonate concentration. The presence of bicarbonate scales with nitrate residues in the sample. Hence, carbonate is clearly less effective in the conversion of the nitrate precursor to layer building intermediates. The latter observation supports the interpretation that metal nitrates are initially hydroxylated by the hydroxide present in the base. Layer building of metal-oxygen-metal sections in the extended lattice structure is likely to involve condensation of metal hydroxyl units under water release. The role of carbonate obviously relates to coordinating layer stacking, such that aluminium in neighbouring layers are guided to adjacent positions, i.e. thermodynamically more favourable "in phase" arrangement of aluminium. Tentatively, out of layer nitrate located ensuring charge compensation of incorporated aluminium gets replaced by hydroxyl. Formal condensation of the hydroxyl function with H_2CO_3 leads to the formation of a bicarbonate. Bicarbonate is able to undergo further condensation with out of layer hydroxyl at coordinated at aluminium of a neighbouring layer forming thermodynamic favourable "in phase" carbonate bridged aluminium pairs between layers. The outlined stepwise process is obviously kinetically challenging, hence, it seems reasonable that very rapid layer growth and lowered local carbonate concentrations would favour the presence of out of layer nitrate residues. While the topic of structure is usually discussed in regards to ionic clays and double layered hydroxides, what effect a kinetically driven reaction would have on the structure for these materials has yet to be found. That leaves this assessment as an independent theory to explain the observed results.

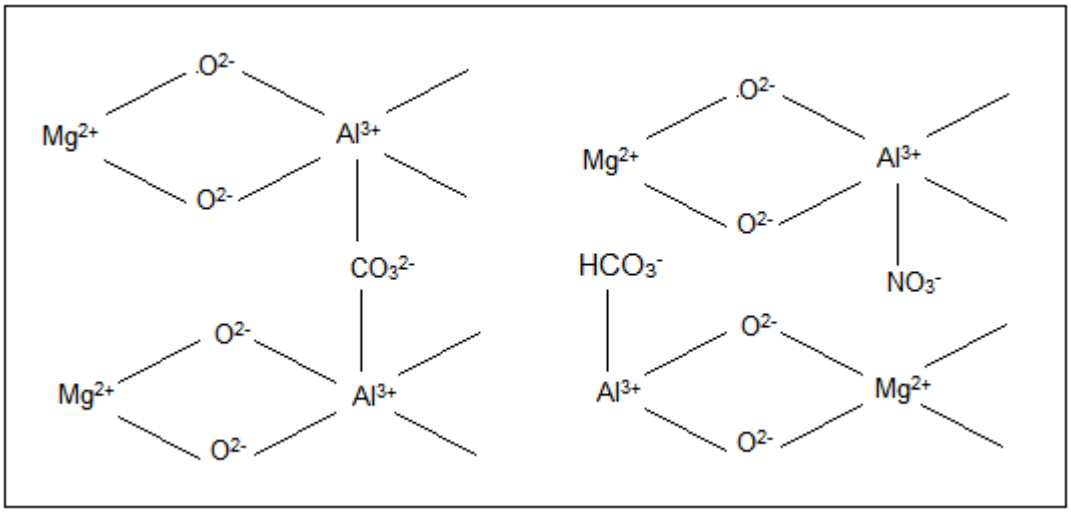

Figure 30. An illustration of the possible anion coordination that occurs when aluminium is both “in phase” (right) and “out of phase” (left).

When the flow sample is washed for two hours (HTCF2h) the dissolution occurs within the materials again. However now it is occurring with a material that is already formed and stable. Dissolution mostly occurs at the larger pores increasing their volume as seen in the BJH and vastly increasing the surface area as seen in the BET. This dissolution also weakens the crystal structure of the lattice accounting for the degrading pattern in the XRD. Nitrate is removed in the washing environment and replaced with hydroxide. The removal of nitrate also greatly increases the surface area by opening up the pores. Since the crystallite sizes do not increase it can be assumed that the rearrangement takes place on a local level with the particle and there is little to no transferral between the particles themselves. This would account for the lower Mg:Al ratio seen in the ICP resulting for the loss of materials from the particles.

Removal of nitrate parallels the depletion of magnesium in the material and transformation of a more mesoporous character to a more macroporous nature of the

material occurs. The most likely explanation is a removal of magnesium from the double layer structure as easily dissolved nitrate. Magnesium removal causes the opening of the pore system leading to enhanced specific surface areas. Furthermore, ^{27}Al NMR indicated the appearance of a shoulder in the peak of octahedrally coordinated aluminium. The latter indicates a slight geometric change to the environment of aluminium possibly caused by magnesium leaving neighbouring positions in the crystal structure. Hence, it is most likely that initial wash leads to a preferred removal of magnesium from the hydrotalcite preserving its structural features with help of alumina pillars allowing explaining the exceptionally high aluminium fractions in the material.

After four hours (HTCF4h) the washing has become counter-productive. As with the samples washed for two hours the BJH shows a wide range of pore diameters with larger volumes however the volumes in general have started to decrease. This would suggest that the dissolution is now affecting the surface of the lattice as well as the pores. This would recreate instability in the lattice layer which is clearly seen in the XRD. It also explains the rebalancing of the Mg:Al ratio in the ICP as aluminium is lost for the lattice as well as magnesium. It is likely that part of the removed aluminium stems from the bridging positions in the lattice. The removal of this aluminium has caused the observed decrease in specific surface area and pore volume by partial collapse of the structure.

Overall the material made in a flow synthesis is more of a hydrotalcite-like material than a true hydrotalcite. Its structure of the lattices and composition of those lattices may well be similar. However the arrangement of the structure and the composition

of the interspatial layer differ and would like be the course of any change in it practical properties.

Chapter 3 – Thermal decomposition and CO_2 adsorption of hydrotalcites synthesised in a continuous process

Literature review

The main driving force behind carbon dioxide capture is the need to find cost-effective solutions to tackle the global issue of climate change. A need to reduce carbon dioxide emissions as the demand for energy continues to increase.[137] There are several methods for solving these problems which include replacing fossil fuels with alternatives (e.g. nuclear), introducing renewables (wind and solar power), increasing the efficiency of fossil fuels and capturing carbon dioxide before its emission into the atmosphere.[79] Renewable sources of energy are still being researched and are still in development, as such complete replacement of fossil fuels seems to be impossible at the present time. The capture of carbon dioxide from a power plant fuel gases is considered to be the effective approach for reducing total carbon dioxide emissions.[79, 84] Until a renewable energy is capable of replacing them, fossil fuels will continue to be needed in the immediate future.[64] To this effect, carbon dioxide capture technologies are required to act as a bridge to a low-carbon energy future.

The three main approaches to carbon capture in large scale industrial plants include pre-combustion, post-combustion and oxy-fuel combustion systems.[64, 137] Pre-combustion systems process the primary fuel in a reactor producing a stream of hydrogen and carbon dioxide. After separation carbon dioxide can be stored or recycled and hydrogen can be used as secondary fuel.[64] Pre-combustion capture is most applicable to integrated gasification combined cycle (IGCC) plants. [137] Post-combustion systems separate carbon dioxide from flue gases produced by

combustion of primary fuel in air.[64] Finally, oxy-fuel combustion systems use oxygen instead of air, which leads to flue gas consisting mainly of water and carbon dioxide, which can be easily separated. [137]

Once captured, carbon dioxide needs to be either stored or recycled. Storage reservoirs need to be sufficiently large and be able to ensure that the carbon dioxide remains trapped inside without the risk of leakage. Geo-sequestration is a process of injecting carbon dioxide into underground geological formations, such as deep saline aquifers, depleted oil fields or un-minable coal beds. Injecting carbon dioxide into declining oil fields has been found to have the benefit of leading to additional oil recovery (enhanced oil recovery), which offsets the cost of sequestration. Injecting into a coal bed can produce a similar side product.[83] Carbon dioxide can be adsorbed on the surface of coal which releases previously adsorbed methane, which can be recovered. The main drawback of geo – sequestration is location of the storage spaces in remote areas, as well as their limited capacities. Saline formations potentially have larger storage volumes and occur more commonly than oil and coal fields. However it is expensive and there are no side products produced to offset the storage cost. [64]

Because of limited storage capacity, storage of captured carbon dioxide is a short term solution. Long term solutions involve recycling carbon dioxide by converting it to hydrocarbons, which can then be reused as fuel. A methanol economy, a hypothetical replacement for the current fossil fuel economy, is based on this, captured carbon dioxide is converted into methanol by reductive conversion, and methanol is further used as fuel. Another involves catalytic conversion of carbon

dioxide directly into hydrocarbons in fuel cell and conversion through stages involving carbon monoxide.[64]

A number of techniques can be used to remove carbon dioxide from fuel gas streams. Gas absorption involves passing a flow of mixed gases over a solvent with a high affinity for carbon dioxide. These gases are then recovered by adding neutralising agents to change the molecular form of the solute gas. Amine-based regenerative chemical absorption processes using aqueous solutions of amine, such as monoethanolamine (MEA), diethanolamine (DEA), diglycol-amine (DGA), *N*-methyldiethanolamine (MDEA) and 2-amino-2-methyl-1-propanol (AMP) have been used for several years for carbon dioxide capture from gas streams in natural gas.[137-140] The down side of gas absorption methods are that they are expensive and energy intensive.

Cryogenic techniques involve separating carbon dioxide from the gas stream by cooling and compression.[141] It involves passing the gas flow over a refrigerated medium and is used in the treatment of biogas.[142, 143] Biogas is produced from the anaerobic respiration of digestion of micro-organisms found in landfills and sewage treatment plants. Biogas consists mainly of methane and carbon dioxide with traces of water, hydrogen sulfide, siloxane, hydrocarbons, ammonia, oxygen, carbon monoxide and nitrogen.[142] For biogas to be converted to biomethane it must be cleaned for these trace components and the calorific value upgraded.[142, 143] Due to the different components of biogas liquefying at different temperature and pressures it is possible to separate out the impurities, producing pure methane from biogas. [142, 143] At high pressure (reported to be approximately 80 bar[143]) and cooled to low temperature (De Hulla *et. al.* reports -175 ^{o}C[143] and Ryckebosch *et. al.* reports -45

^{o}C[142]) carbon dioxide condenses and can be easily removed.[142, 143] The separated carbon dioxide can then be used as a solvent to further purify the methane.[143] The main drawback of cryogenic sorption methods is them being expensive and energy intensive due the required temperature and pressures needing to be maintained.[64]

Membrane filtration involves components being removed from the gas stream by absorption or selective diffusion through a membrane. Different particle sizes permit certain molecules to pass through the membrane while others cannot. Separation of the molecules is driven by a pressure differential set up on either side of the membrane. As well as small molecules, highly soluble molecules will pass through the membrane too.[143] Like the cryogenic techniques described above, membrane filtration is used for the separation of carbon dioxide from the methane found in biogas.[142, 143] Membranes work well on lab scale reactions but when increased to production scale they become expensive. Also it is difficult to make membranes of the necessary size.

Adsorption methods are where molecules of carbon dioxide are concentrated on the surface of a solid. Carbon dioxide acting as an electrophile will be attracted by base sites on a sorbent surface and bind there. The benefit of solid adsorbents for carbon dioxide capture is their chemistry is scalable. If it works on small lab scale reactions then sizing to production scale is a straight forward engineering task. They can be regenerated at a lower energy requirement compared to other methods of carbon capture.[137] This allows for multiple use and long term stability. Their properties can be easily tailored. This makes it a viable option for use at a range of different temperatures.[137] Technology needed for producing these solid adsorbents is developing rapidly, which shall allow for an easy and quick production.

Lithium zirconate is a solid adsorbent that is used for high temperature (450 to 550 ^{o}C [64, 144, 145]) carbon dioxide adsorption. This is accomplished by the compound conversion to lithium carbonate and zirconium oxide. At higher temperature the conversion can be reversed, allowing for the recovery and further use of carbon dioxide.[64, 144] It also allows for continued use of the regenerated starting material. The reaction is highly selective to carbon dioxide making it ideal for removing carbon dioxide from gas streams.[64] The adsorption rate of lithium zirconate has been shown to slow due to the formation of lithium carbonate and zirconium oxide shells around particles of unreacted material. To increase the adsorption rate lithium zirconate is doped with potassium carbonate. The latter increases the adsorption rate by the formation of an eutectic molten carbonate at high temperatures.[145] Kato *et. al.* reports that lithium orthosilicate has similar properties and may surpass the capacity of lithium zirconate. The use of silicon oxide instead of zirconium oxide makes the material lighter and cheaper to produce.[146]

Metal organic frameworks (MOFs) are synthesised by the self-assembly of organic ligands and metal oxides.[147] The resulting materials have large surface areas with large pore volume and regular pore size.[147, 148] The chemical properties of MOFs are tuneable by manipulation of the metal centres or the organic ligand.[147] The tuneable nature of these MOFs gives them a wide variety of potential uses. Zeolites are reported to have a carbon dioxide uptake of 4.7 mmol/g at 1 atm and 298 K [148]

Amines interact with carbon dioxide by forming carbamate and ammonium ions. [149] This functionality can be easily incorporated into any number of inorganic and organic compounds. Reports have shown that this functionality has been effectively used in both solid compounds and ionic liquids.[149] In the case of ionic liquids

carbon dioxide uptake has been shown to be in excess of 0.5 mol of carbon dioxide per mol of ionic liquid.[149]

The possibility of using hydrotalcite as high temperature carbon dioxide adsorbents arose from previous adsorption work carried out on various metal oxides, including MgO, CaO and Al_2O_3.[80, 148] Since then hydrotalcite materials were extensively studied as potentially suitable adsorbents for carbon dioxide.[76-85] In a previous study by Yong *et. al.* it was found that carbon dioxide adsorption was higher at room temperature than at 200 °C. [79] In the study, it was discussed that the different stages of thermal decomposition was the reason behind this. The samples in the study were not calcined beforehand. At 200 °C the sample has been dehydrated but the lattice layers are still intact. By 300 °C the lattice layer have started collapsing through dehydroxylation and decarbonation. The Al^{3+} cation environment moved from octahedral to tetrahedral and that created pores for more carbon dioxide to adsorb.[76, 79]

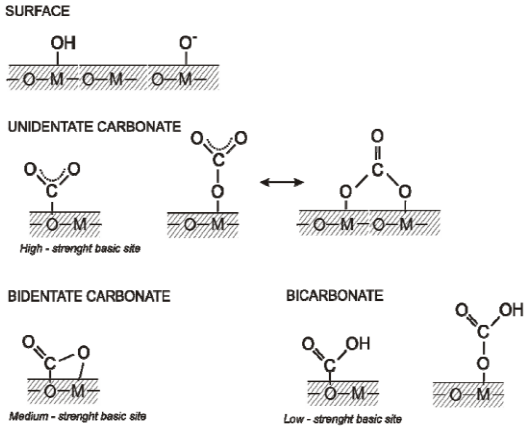

Figure 31. Adsorption sites on metal oxides and CO_2 adsorbed species[64, 150]

Carbon dioxide molecules can adsorb to both negative and positive sites, however as it is an electrophile, are expected to adsorb more strongly on base sites. Adsorption

species of CO_2 on metal oxide surfaces consist of unidentate, bidentate and bi – carbonate (Figure 31). Unidentate carbonate is formed when adsorption takes place on the surface oxygen or on the metal ions with participation of excess oxygen. When adsorption takes place on a hydroxyl group, formation of superficial bicarbonate occurs.[64]

When hydrotalcites are calcined they form a unique mixture of metal oxides that is impossible to achieve by mixing the relative metal oxides together. This mixture of metal oxides was shown to adsorb CO_2 between room temperature and 450 °C. This is done by the conversion of magnesium oxide to magnesium carbonate.[89] By taking the temperatures above 450 °C, CO_2 begins to desorb, allowing regeneration of the mixed oxide and the release of carbon dioxide.[86, 89, 92] These mixed metal oxides have also shown the capacity to be regenerated back to a hydrotalcite by rehydrating the metal oxides through contact with water. A hydrotalcite with better crystalline structure can be better regenerated. This allows the hydrotalcite to be reused multiple times.[89, 92]

In the previous chapter, the synthesis of hydrotalcites was explored in a continuous flow process and compared to a sample made in a batch process. The process discovered that though the lattice layer was formed, the aluminium was “out of phase” with each other between the lattices. This led to the carbonate ions forming bicarbonate instead of creating a bridge between lattices. In this chapter the effect of this organisation, within the material is investigated. In particular, the effect of oxide formation through thermal decomposition and the ability of those mixed oxides to absorb carbon dioxide.

Experimental

Material preparation

The materials used in this chapter were the same materials made in Chapter 2. These materials were hydrotalcites that were synthesised in a batch process (HTCB) and a flow process (HTCFw). Two additional materials were also used. These were hydrotalcites also synthesised in a flow process and washed for 2 h (HTCF2h) and 4 h (HTCF4h). The description of the synthesis used is found above in the materials preparation section of Chapter 2.

Analytical Procedures

Carbon dioxide adsorption calorimetry under flow conditions was performed on the hydrotalcites using a flow-through Setaram 111 differential scanning calorimeter (DSC) and an automated gas flow and switching system, modified through the use of a mass spectrometer detector for the down-stream gas. The analysis was preformed by Rob Brown and Marta Granollers at Huddersfield University.

All samples (18-30 mg) were dryed at 120 °C under dried nitrogen for 3 h then the temperature changed to 30 °C for 1 h. After that 0.5-1 mL pulses of the probe gas (1% CO_2 in N_2) at atmospheric pressure were injected at regular intervals into the carrier gas stream from a gas-sampling valve. The concentration of carbon dioxide downstream of the sample was monitored continuously with the mass spectrometer. The interval between pulses was chosen to ensure that the carbon dioxide concentration in the carrier gas (including that adsorbed and then desorbed after the pulse had passed) returned to zero, and to allow the DSC baseline to re-establish itself.

The net amount of CO_2 irreversibly adsorbed from each pulse was determined by comparing the MS signal during each pulse with a signal recorded during a control experiment through a blank sample tube. Net heat released for each pulse, corresponding to irreversible adsorption of CO_2, was calculated from the DSC thermal curve. From this the molar enthalpy of adsorption (ΔH_{ads}) was obtained for the CO_2 adsorbed from each successive pulse. The ΔH_{ads} values were then plotted against the amount of (irreversibly) adsorbed CO_2 per gram of the catalyst, to give a ΔH_{ads} /coverage profile for all samples.

Thermogravimetric analysis (TGA) is a method of thermal analysis which gives insight into changes in physical and chemical properties of materials are measured as a function of increasing temperature, or as a function of time. TGA can provide information about physical properties such as second order phase transitions, including vaporisation, sublimation, adsorption, absorption, and desorption. Likewise TGA can give information on the chemical properties of a material, including chemisorption and decomposition. The TGA instrument continuously weighs a sample as it is heated. As the temperature increases various components of the sample are decomposed and the weight percentage changes. In DTA, the material under study and an inert reference are made to undergo identical thermal cycles, while recording any temperature difference between sample and reference.

Thermogravimetric analysis was preformed on a Polymer Laboratories STA 1500. Samples weighing 13-15 mg were placed into a crucible along side an empty crucible for a comparison. The sample was heated to 500 °C and a rate of 10 °C min^{-1} in an inert gas. Once calcined the sample was allowed to be cool to 30 °C, where

the gas was changed to carbon dioxide for 10 min until the sample was saturated the gas. The gas was reverteed back to the inert gas and temperature returned to 500 °C. This process was repeated three times.

Results and Discussion

X-Ray Diffraction

For all the samples (Figure 32-34) except HTCF4h, the peak corresponding to diffraction reflection (003) shifted to higher 2Θ while losing intensity before it disappeared completely by 385 °C. This shift and disappearance of the (003) was not seen in the pattern for HTCF4h (Figure 35) due to it not being present in this diffraction pattern (see Chapter 2 for an explanation as to why this happens). This temperature was in the decarbonation region visible in the TGA and DTA. The (006) reflection lost intensity at a much lower temperature, disappearing by 180 °C which was in the temperature range that the loss water can be seen in the TGA and DTA. Within the same temperature range attributed to water loss, the two reflections around 60° became broader. They had merged to a single reflection by 180 °C. The significant broadening of reflection above this temperature was attributed to the formation a periclase crystalline structure.[74, 89] A periclase crystalline structure refers to the cubic form of the magnesium oxide. Through dehydroxylation and decarbonation the lattice collapsed by 375 °C and after which metal oxides started to form.[89, 92] For the HTCB and HTCFw only two reflections were seen that are representative of the mixed oxides. Both of the flow samples that were washed displayed a degree of degradation in the diffraction pattern that was better shown in Chapter 2. The degradation followed through the decomposition of the samples and was especially noticeable at low 2Θ.

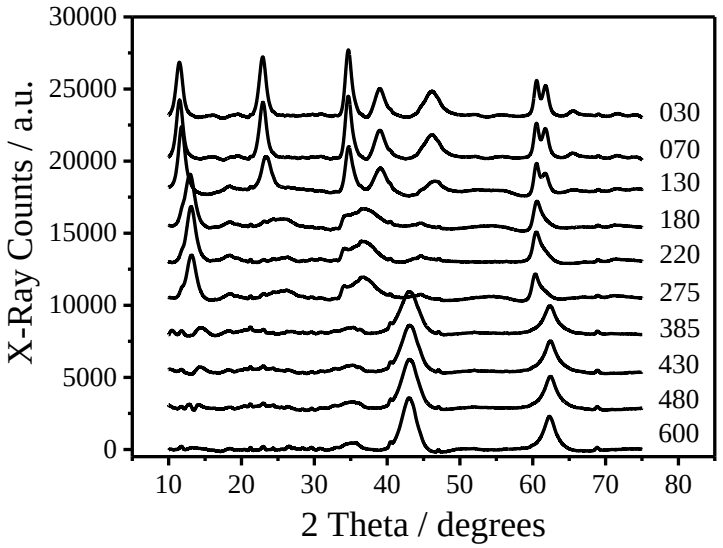

Figure 32. *In situ* XRD pattern of HTCB, showing the decomposition of the structure as temperature increases. The numbers in the legend correspond to the temperature (°C) at which patterns were recorded.

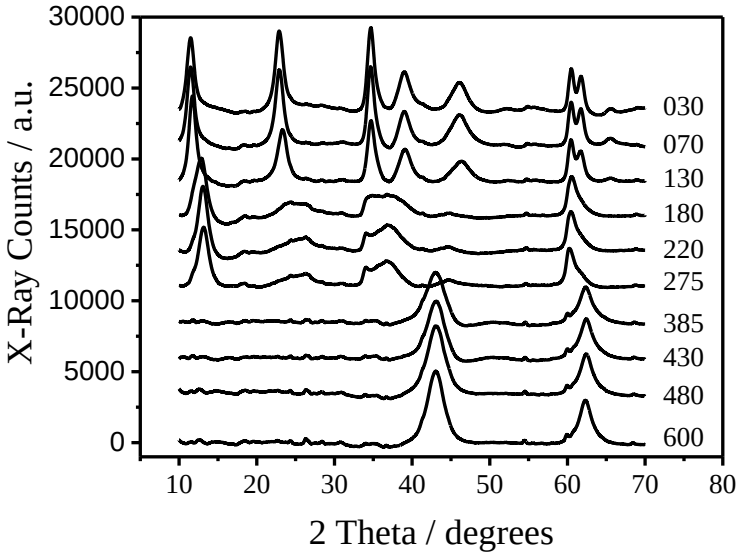

Figure 33. *In situ* XRD pattern of HTCFw, showing the decomposition of the structure as temperature increases. Numbers in the legend corresponds to the temperature (°C) at which patterns were recorded.

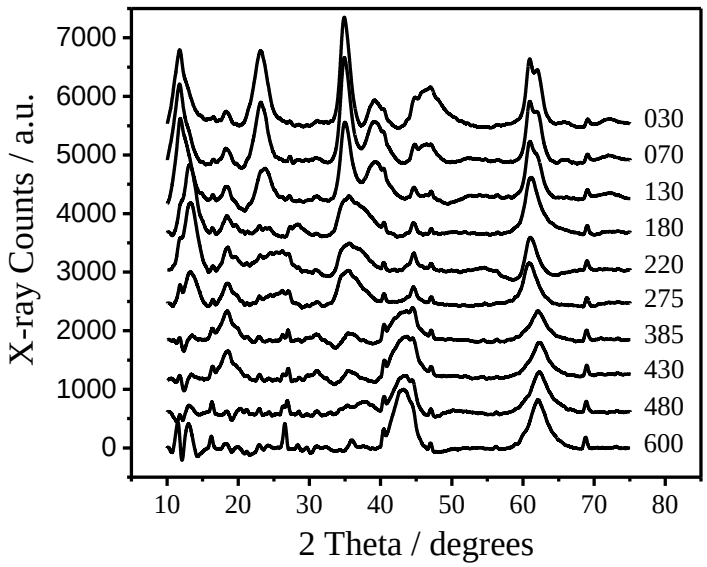

Figure 34. *In situ* XRD pattern of HTCF2h, showing the decomposition of the structure as temperature increases. Numbers in the legend corresponds to the temperature (°C) at which patterns were recorded.

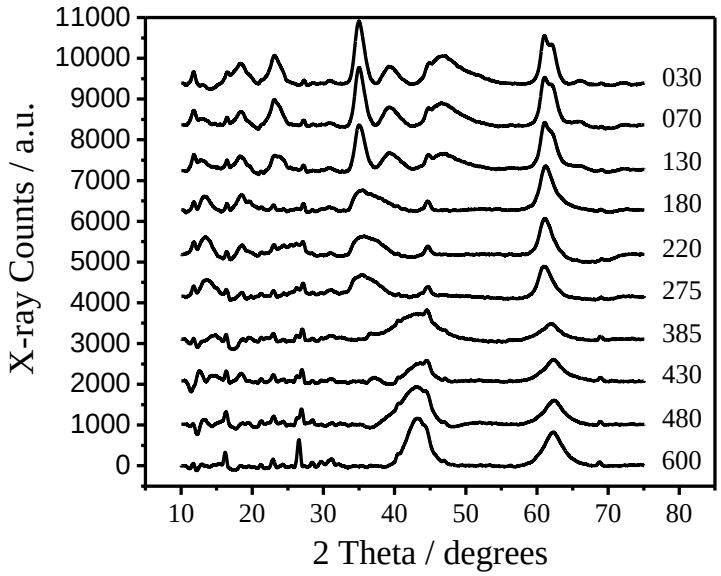

Figure 35. *In situ* XRD pattern of HTCF4h, showing the decomposition of structure as temperature increases. Numbers in the legend corresponds to the temperature (°C) at which patterns were recorded.

Raman Spectroscopy

The bands at 480 and 551 cm^{-1} represented the Al-O-Al band and the Al-O-Mg band as discussed in Chapter 2. As the temperature increased these bands persisted and had a continued presence well beyond the collapse of the lattice structure. With dehydroxylation and decarbonation already occurring at this point it would suggest that the remaining structure have taken a different form. At high temperature two component oxides will fuse together to form a spinel material ($MgAl_2O_4$ or $MgO{\cdot}Al_2O_3$).[151] Due to the repulsion of positive charges Al^{3+} within the lattice remain at a distance from each other, yet as discussed in the previous chapter the aluminium ions that align in different layers will form the interlayer connection with

the carbonate ion. It can be assumed that when decarbonation and dehydroxylation took place carbon dioxide was released from the bridging bond leaving two aluminium atoms linked by an oxygen atom. This would allow the formation of the spinel and explain why the metal-oxygen-metal bands were still visible at high temperature. These two bands eventually disappeared by 600 °C suggesting that the fused oxides separated into individual components. The carbonate bands shifted slightly during heating and endured longer than the metal linkage band. There was a loss of intensity during the stages of decomposition involved in the initial decarbonation. They endured as the decomposition process involved the formation of magnesium carbonate. This can be seen as the band moved back to higher wavelengths at higher temperature, after the second stage of decomposition involving dehydroxylation and decarbonation. The presence of the band at the end of the process would suggest that some magnesium carbonate remained until the end.

As discussed in Chapter 2 the flow samples are made under kinetic control. Any aluminium ions that were "in phase" became so through random probability, not by design with factors such as stability being considered. While some carbonate did bridge the interspatial layer, the rest bound with an additional hydrogen atom to form bicarbonate ion. This would suggest that as decarbonation took place the formation of an aluminate ion (AlO_2^-) [152] was more likely. This was further indicted by the metal-oxygen-metal band disappearing by 385 °C. This would suggest the flow material decomposed into a mixed oxide form without the formation of a spinel structure. This would back up what is seen in the Al^{27} NMR, with the aluminium clustering in the unwashed flow sample. The carbonate peaks behaved in same manner as in the spectrum for the batch material except the remaining carbonate peak was of greater intensity. This could be due the additional magnesium available

to form magnesium carbonate during the decarbonation stage because of the lack of spinel formation. It should also be noted that the peak above 700 cm^{-1} and the shoulder seen on the 1050 cm^{-1} peak were, according to Böckelmann and Schlecht *et. al.*, indicative of nano-sized MgO which offered further suggestion that there was a separation of MgO and Al_2O_3. However, since the Raman spectrometer was being used qualitatively rather than quantitatively, this could not be verified from this analysis.

The flow samples that had been washed showed a similar spectra to the batch sample. The bands representing the metal vibrations endured untill higher temperatures, suggesting the decomposition to form spinel. Spinel is part of the spinel group of minerals of the formula $A^{2+}B^{3+}{}_2O^{2-}{}_4$. In the case of spinel, the formula is $Mg^{2+}Al^{3+}{}_2O^{2-}{}_4$. Unlike the previous two samples, the carbonate bands completely disappeared by the end of the decomposition. As discussed in Chapter 2, both the washed flow samples were aluminium rich due to the washing process removing magnesium from the structure. It could be interpreted, stable carbonates result from magnesium be removed from aluminium. Hence, aluminium could have had the role of a modifier preventing too stable carbonate formation. Please note that the latter was pretty consistent to the microcalorimetry below. Washing would have initially led to preferential dissolution of nano sized MgO.[153]

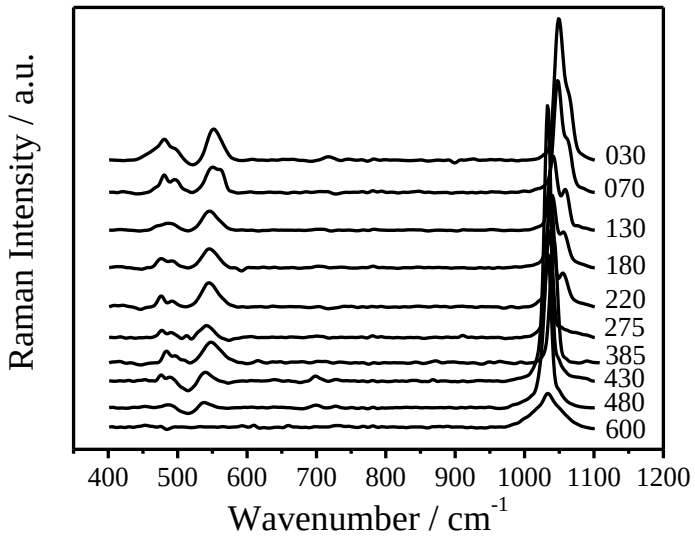

Figure 36. *In situ* Raman spectrum of HTCB. Numbers in the legend correspond to the temperature (°C) at which patterns were recorded.

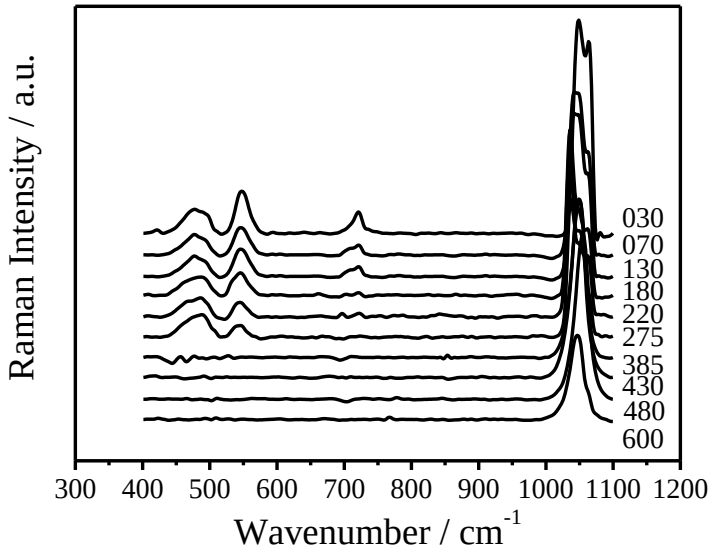

Figure 37. *In situ* Raman spectrum of HTCFw. Numbers in the legend correspond to the temperature (°C) at which patterns were recorded.

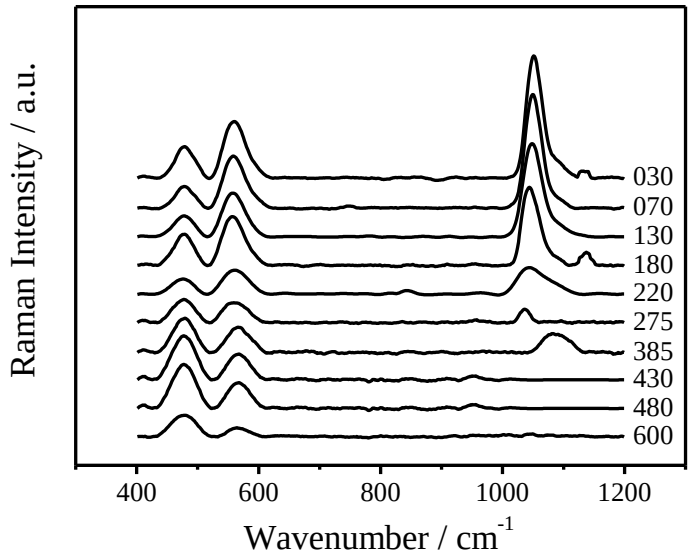

Figure 38. *In situ* Raman spectrum of HTCF2h. Numbers in the legend correspond to the temperature (°C) at which patterns were recorded.

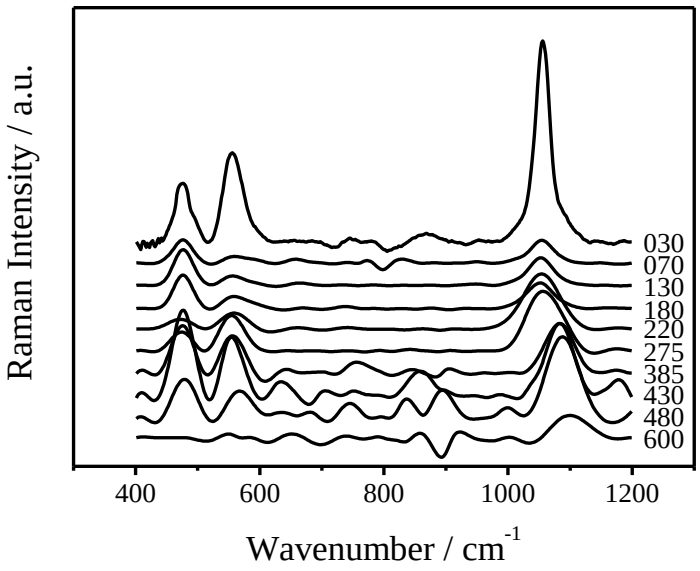

Figure 39. *In situ* Raman Spectrum of HTCF4h. Numbers in the legend correspond to the temperature (°C) at which patterns were recorded.

Microcalorimetry

All the samples, except HTCFw, displayed a similar pattern seen for microcalorimetry of magnesium oxide (see Figures 40 and 42) but with more base sites. [74, 150] They displayed a plateau of chemisorption in the area that was associated with strong sites. These plateaus were found respectively around 98 (HTCB), 105 (HTCF2h) and 110 kJ mol^{-1} (HTCF4h). These values covered a wide range of surface coverage; this indicated that a large portion of the oxide surface was acting homogeneously and the carbon dioxide was interacting with the oxides through chemisorption in a similar manner throughout the material. Busca *et. al.* found through an infrared study that the chemisorption of carbon dioxide on magnesium oxide was mainly bidentate (see Figure 31) adsorbed species, with a small part unidentate.[1] This could be accounted for by the layers being bridged by the carbonate in the original structure. As the hydrotalcite thermally decomposed, carbon dioxide was released, leaving behind oxygen bridging the aluminium in the lattice. As the lattice collapsed, the presence of bridged aluminium facilitated the formation of a spinel structure comprised of magnesium aluminium oxide ($MgAl_2O_4$) being formed. [74, 89, 92, 98, 154]

The flow samples showed a similar curve to alumina. [150] This pattern indicated that the oxide surface was acting with heterogeneity and the carbon dioxide was interacting with the surface in a variety of ways. This was likely due to the formation of the individual oxides of magnesium and aluminium in the thermal decomposition of the original hydrotalcite structure. Due to aluminium not being linked by carbonate ions, when the lattice collapses with aluminate (AlO_2^-) [152] and magnesium oxide being formed. Microcalorimetry was also performed of the

samples HTCFc, HTCFo and HTCFco to see if this trend extended to other unwashed flow samples which it did.

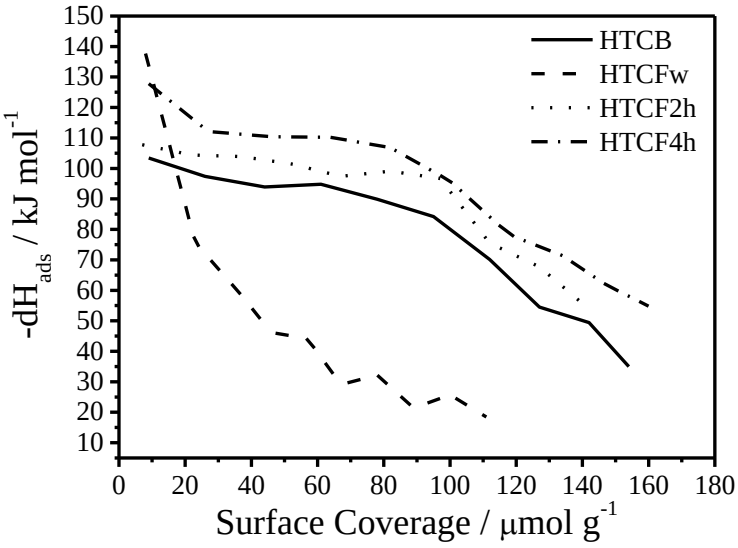

Figure 40. Microcalorimetry of HTCB, HTCFw, HTCF2h and HTCF4h

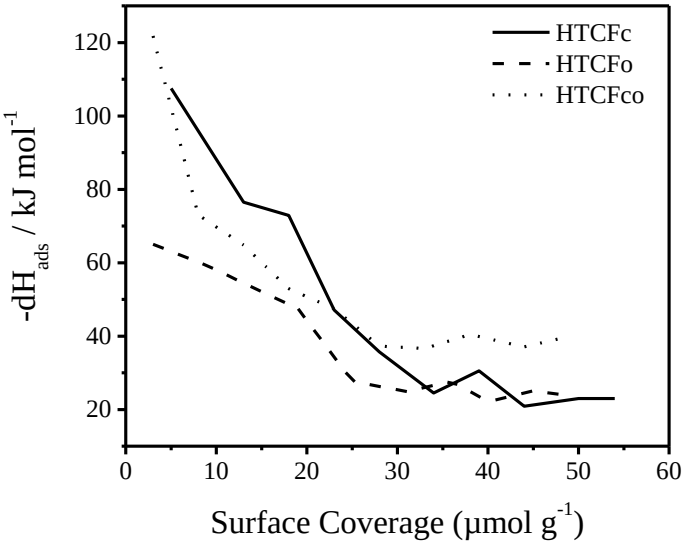

Figure 41. Microcalorimetry of HTCFc, HTCFo and HTCFco

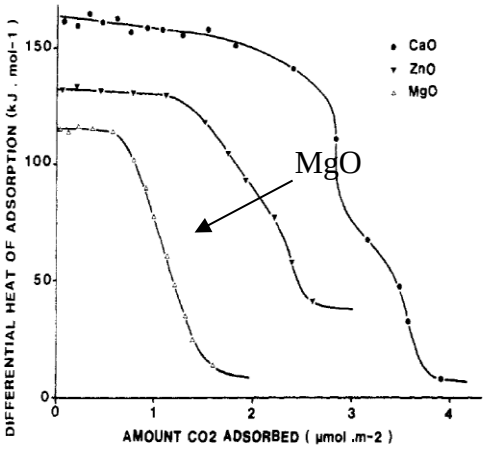

Figure 7. Differential heats of adsorption of CO_2 as a function of the coverage for CaO, ZnO, and MgO.

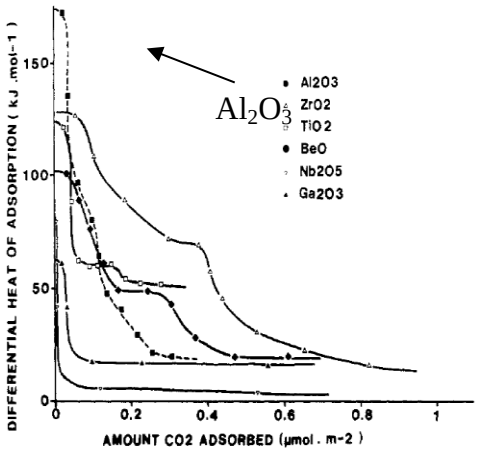

Figure 9. Differential heats of adsorption of CO_2 as a function of coverage for group A–B oxides.

Figure 42. Microcalorimetry of magnesium oxide and aluminium oxide [150]

Thermogravimetric Analysis / Differential Scanning Calorimetry

The TGA curves showed weight loss occurring in three distinct stages. Weight loss between ambient temperature to 250 ^{o}C can be attributed to the loss of external surface water and water found in the interspatial layer.[74] Rey *et. al.* reports that evidence of a partial dehydroxylation occurred simultaneously. [98] The second region, between 250 to 430^{o}C showed dehydroxylation of the lattice layer. This area had also been attributed to a significant amount of decarbonation as carbon dioxide was released from the counter anions. The precise temperature that the two processes occurred within is unknown.[89] The third region, at temperatures above 430^{o}C, was attributed to the loss of any remaining volatile species, including the decomposition of mineralised magnesium carbonate to form magnesium oxide and carbon dioxide. The masses lost during calcination were consistent with values found in the literature. [76, 92, 98]

The DTA scan showed two definite endothermic peaks. A broad curve appeared at the beginning of the scan in the range of the water removal.[116] The broad curve displayed by the samples showed two distinct areas of loss. Surface water was removed first, and then water from within the lattice, needing more heat, was removed. For the HTCB the weight loss and energy show a peak that was greater for the second band. The HTCFw showed a reverse of this suggesting that there was less water in the interspatial layer of the material. In the CHN discussed in Chapter 2 it was found that the flow samples have additional ion content in the form of nitrate. The extra ions would reduce the space in layer leaving less room for any water. As the nitrates were washed out, more water is allowed to enter the interspatial layer. This was further seen as the second peak increased with washing suggesting that there was more water to be lost.

The next large peak seen was the evolution of carbon dioxide by the interspatial carbonate anions [76, 116] in the range that the lattice collapses (see XRD below). For the samples that were washed this second peak splits to show two peaks. Forano *et. al.* states that the first of these was the dehydroxylation of the aluminium. The second peak represented the dehydroxylation of magnesium and decarbonation of the interspatial carbonate anions. [116] Both these peaks were shallow relative to the water loss peak. Forano *et. al.* also reported similar patterns that were due to smaller Mg:Al ratios.[116] This was further confirmed by the ICP discussed in Chapter 2. HTCF2h had the most pronounced shoulder in the peak and this sample showed a Mg:Al ratio of 1.7:1 instead of the expected 3:1. HTCF4h had a ratio of 2.1:1 and displayed a shoulder that was softer than the shoulder seen for HTCF2h.

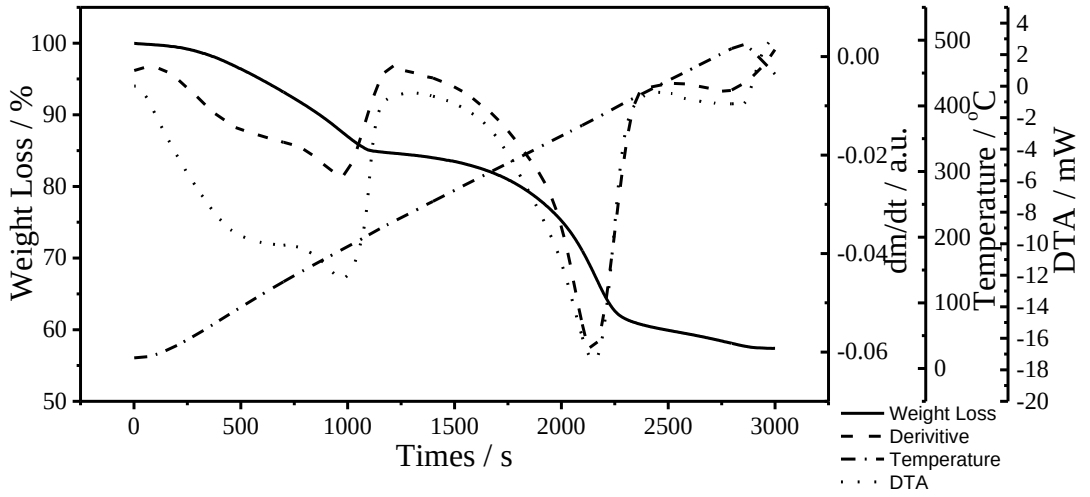

Figure 43. Thermogravimetric analysis and differential temperature analysis of HTCB.

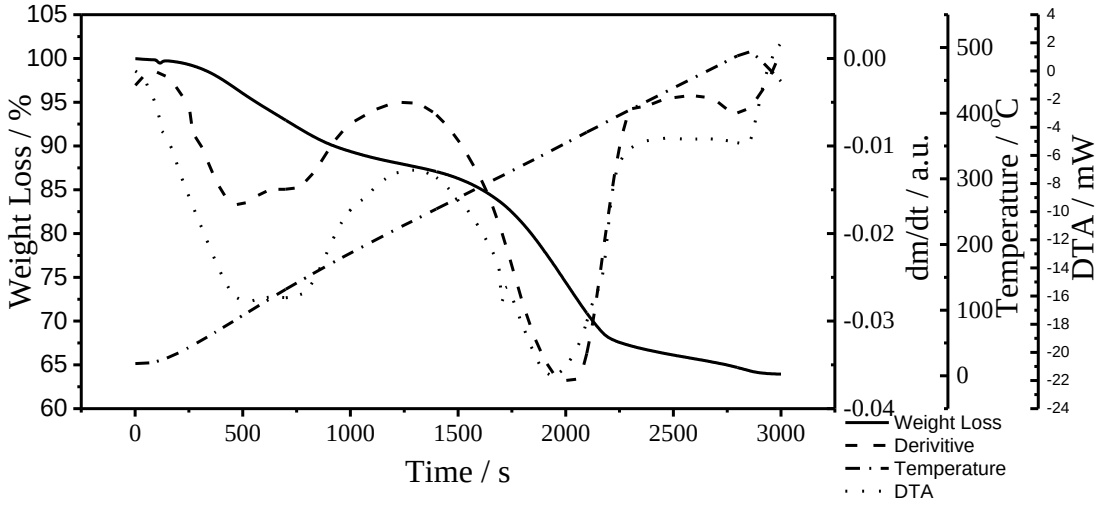

Figure 44. Thermogravimetric analysis and differential temperature analysis of HTCFw.

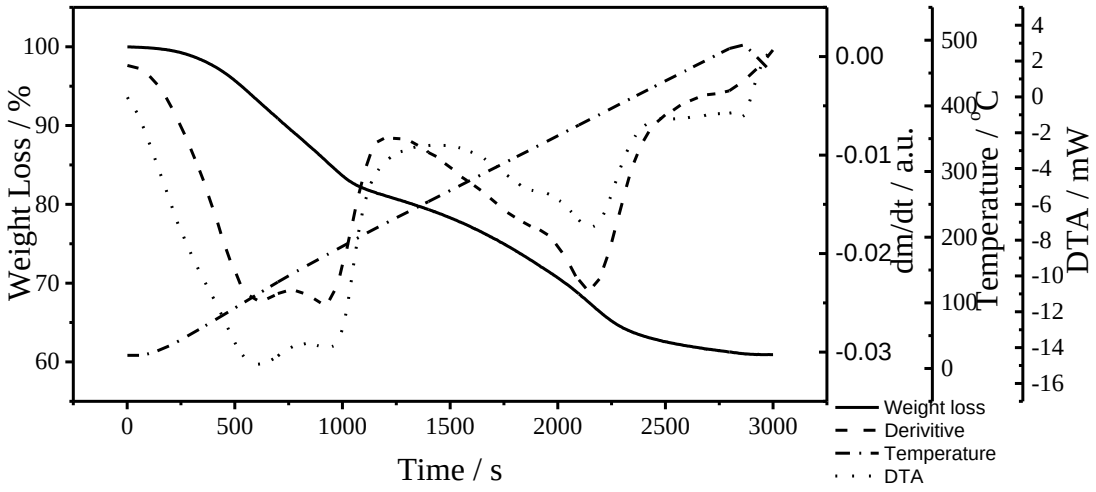

Figure 45. Thermogravimetric analysis and differential temperature analysis of HTCF2h.

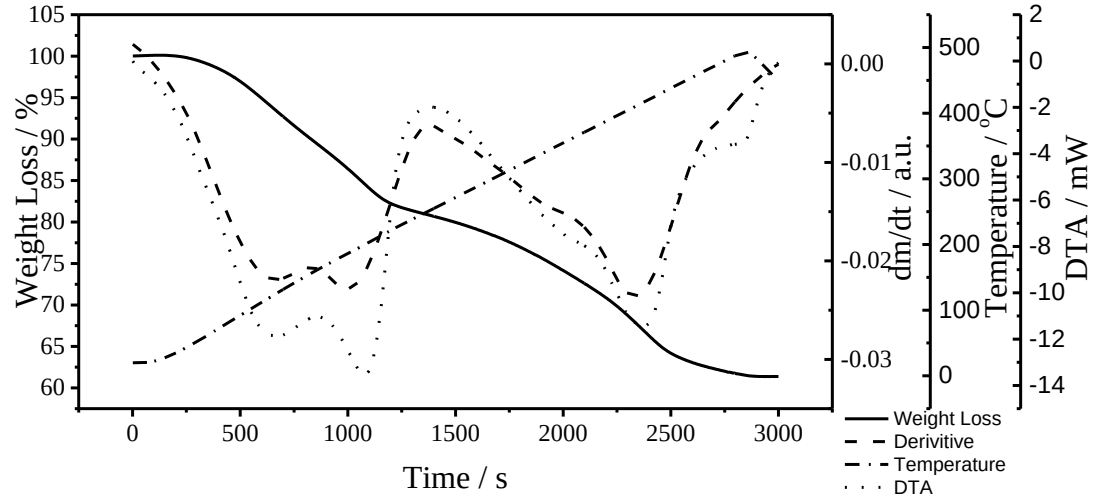

Figure 46. Thermogravimetric analysis and differential temperature analysis of HTCF4h.

For CO_2 uptake measurements, all the samples, except for HTCF4h, displayed a similar pattern. The first and second cycles took up a similar amount of CO_2, while the third cycle showed a drop in uptake. These three samples all showed a similar uptake of CO_2. The sample that was washed for four hours showed an uptake in the first cycle that was nearly double the uptake of the other three samples. The second cycle had a lower uptake and the third displayed a slight increase.

Table 12. Maximum CO_2 uptake of the hydrotalcite samples.

	Maximum CO_2 Uptake (mmol/g)		
	Cycle 1	Cycle 2	Cycle 3
HTCB	0.26	0.25	0.18
HTCFw	0.22	0.22	0.19
HTCF2h	0.25	0.24	0.19
HTCF4h	0.41	0.18	0.22

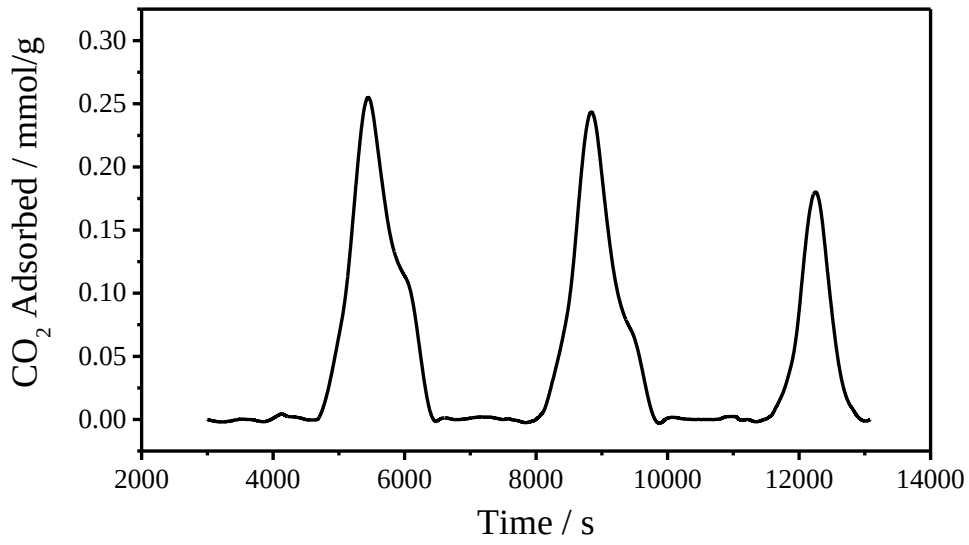

Figure 47. Carbon dioxide adsorption of materials synthesised in HTCB.

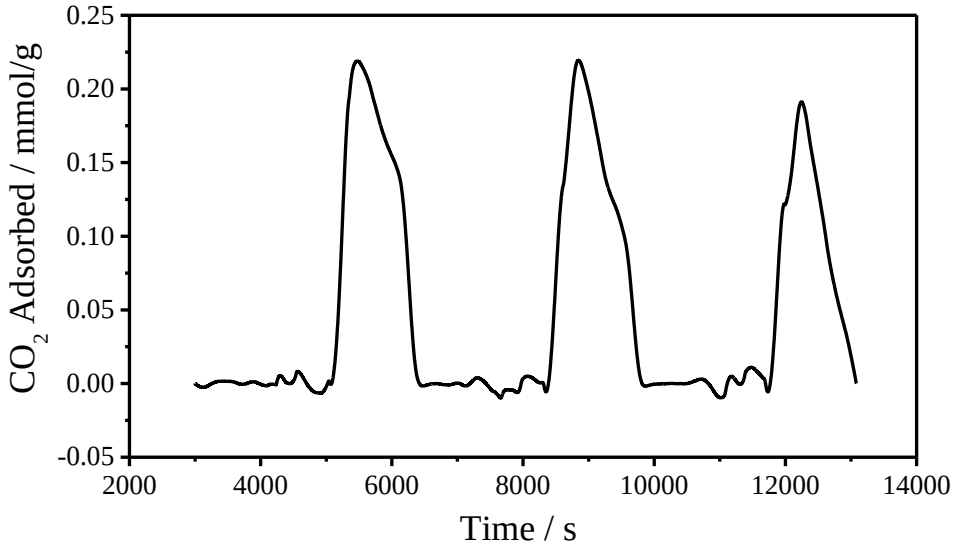

Figure 48. Carbon dioxide adsorption of materials synthesised in HTCFw

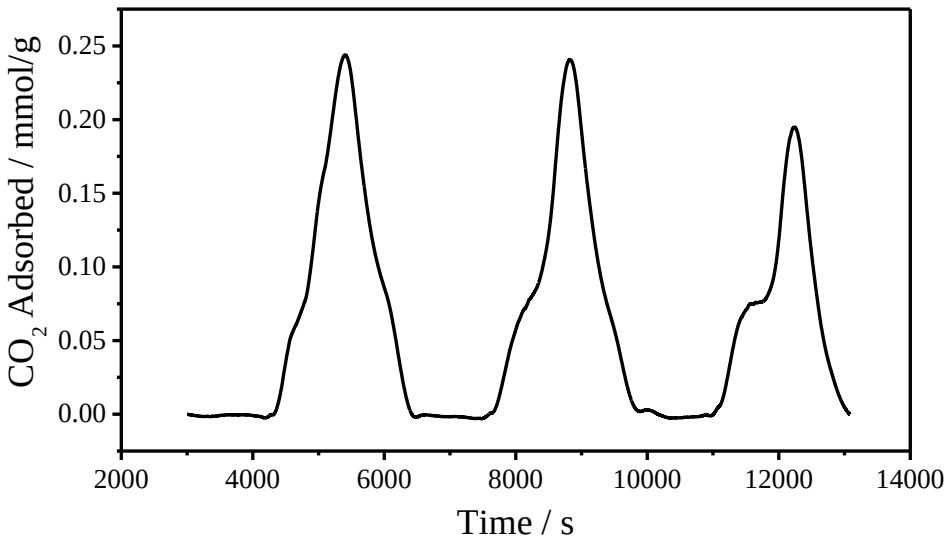

Figure 49. Carbon dioxide adsorption of materials synthesised in HTCF2h

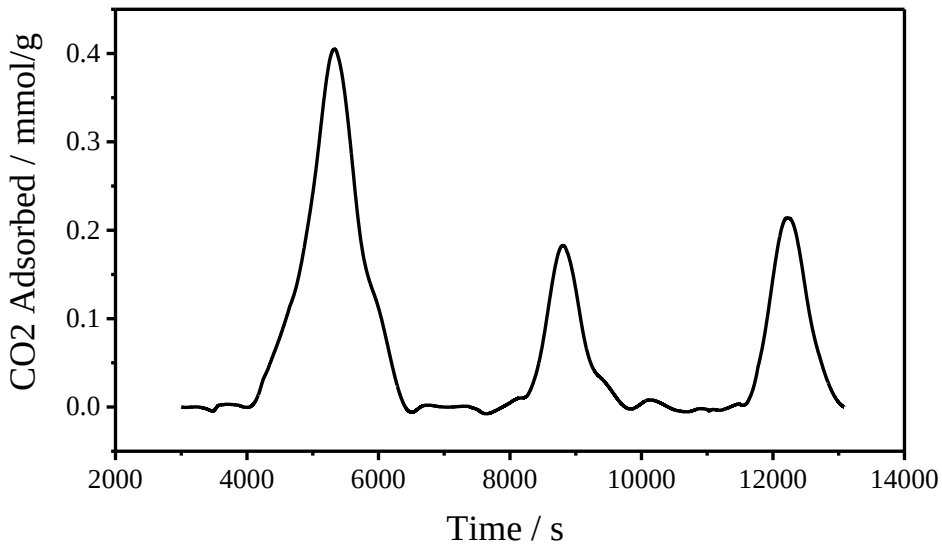

Figure 50. Carbon dioxide adsorption of materials synthesised in HTCF4h

Conclusions

When HTCB, HTCF2h and HTCF4h are calcined, they break down in a similar manner. Once dehydroxylation has occurred and the decarbonation is starting the lattice begins the break down to form a magnesium/aluminium spinel. This is seen in the microcalorimetry as a pattern similar to that for magnesium oxide. The spinel binds with the carbon dioxide in a homogeneous manner, converting the magnesium oxide element of the spinel structure to magnesium carbonate. Base sites of HTCB and HTCF2h are impeded by carbonate anions that have not been decomposed during the calcination process, giving similar amounts of CO_2 adsorption. HTCF4h does not have this problem, allowing for more base sites to be available for the first cycle of adsorption. Not all of these base sites are recovered and some are lost. It is unknown with any certainty why this happens and warrants further investigation.

HTCFw decomposes much faster than the other samples. This suggests the carbonate bridges provide an increase in thermal stability. The loss of the metal-oxygen-metal vibration bands in the Raman spectroscopy shows that the decomposition does not form a magnesium/aluminium spinel recorded in other studies and would appear to allow the formation of aluminium oxide independent of magnesium oxide. The formation of aluminium oxide is also seen in the microcalorimetry. The pattern seen is similar to aluminium oxide and that carbon dioxide binds heterogeneously. This would suggest that carbon dioxide is interacting with both aluminium oxide and magnesium oxide. It can also be seen in the Raman that magnesium carbonate still exist by the end of the decomposition once again impeding the base site.

It would be of interest in further studies to calcine the samples to a higher temperature to attempt to drive of the remaining carbonate. This should open up

more base sites for adsorption to interact with. When compared to other studies of CO_2 sorbents, the materials looked at during this project do not come close to replicating the values reported. In general the materials from this project requires ten times the mass to adsorb 1 mol of CO_2 as reported for zeolites and twice the mass as reported for hydrotalcites. After the project samples, the material with largest required mass is the hydrotalcite from the literature. With some tuning of the experimental procedures, it may be possible to get a value close to this literature value. The initial adsorbsion cycle of HTCF4h does produce value close to the literature value, however returns to the masses required for the other samples.

Table 13. A table showing literature value from the mass of known sorbents required to adsorb 1 mol of carbon dioxide

Sorbent	Kg/mol		
MEA	0.061 [155]		
$CaCO_3$ (crushed stone)	0.1 [156-160]		
K_2O (potash)	0.0942 [161]		
Na_2CO_3 (soda ash)	0.106 [162, 163]		
Li_2CO_3	0.0739 [164, 165]		
Active carbons	0.5 [161, 162, 166]		
Zeolites	0.2 [161, 162, 166]		
Hydrotalcites	2.0 [167]		
Fe_2O_3 (iron ore)	0.160 [168]		
Cobalt	0.059 [169]		
Copper	0.1271 [169]		
Nickel	0.0587 [169-172]		
Manganese	0.055 [169]		
HTCB	3.8	4.0	5.5
HTCFw	4.5	4.5	5.3
HTCF2h	4.0	4.2	5.3
HTCF4h	2.3	5.5	4.5

Chapter 4 – Catalytic activity of nickel doped hydrotalcites synthesised in a continuous flow process

Literature Review

Hydrotalcites and their decomposed products have found many applications, including in catalysis.[86] During calcination of hydrotalcites an intricate mixture of oxides is formed, unattainable by simple mixing of the relevant bulk metal oxides together. The oxides catalytic activity can attributed to the presence of base sites.[86, 89]

Michael addition reactions involve base catalysed C-C bond coupling reactions. [74] While these liquid phase reactions are conventionally catalysed by soluble bases, environmental concerns have moved the focus to solid catalysts. [74, 173] Choudary *et al.* found that rehydrated hydrotalcites were an efficient and selective catalyst for Michael additions. [174] Yet Prescott *et al.* found that uncalcined and calcined hydrotalcites also highly selective for Michael additions of 2-methylcyclohexane-1,3-dione, 2-acetylcyclopentanone and 2-acetylcyclohexanone to methyl vinyl ketone. [74] While the activity of pure MgO was found to surpass the hydrotalcites in activity it was also found that they produced consecutive reactions.[74]

Within the chemicals and petroleum industries many toxic compounds are produced. Among these are phenol and its halogenated derivatives, the most hazardous of these being chlorophenol and *p*-cresol. [108, 175] Work has been done to produce a catalyst that can be used to remove the chemicals from contaminated water by Advanced Oxidation Processes (AOP). [176] AOP uses high reactivity hydroxyl ($OH^{*)}$ radicals combined with UV light [177] to drive the oxidation process to achieve complete

mineralisation of the organic pollutant. Calcined hydrotalcite has been shown to be a catalyst that has a high capacity for the photo-decomposition of chlorophenol and *p*-cresol as well as other organic pollutants such as benzene and phenolic compounds. [108]

Hydrotalcite has also been used as a catalyst in the synthesis of biodiesel by the methanolysis of sunflower oil. The untreated samples have been found to be catalytically inactive, but the calcined and the rehydrated samples have been shown to have good catalytic activity. Samples calcined at 500 ^{o}C have been shown to achieve 50% conversion after 24 hrs at 60 ^{o}C. The samples rehydrated in boiling water were shown to have better catalytic activity than the calcined samples.[96]

Hydrotalcites have also been used as precursors of catalyst supports in the polymerization of olefins using Ziegler catalysts. [178] Once the hydrotalcite is calcined, it is sieved to obtain a particle fraction between 2 and 100 microns. This fraction is partially or completely chlorinated with chlorine or phosgene to obtain a mixed chloride or oxychloride which is used in turn as a support for the active phase, which is prepared from a mixture of titanium or vanadium chloride and an alkylaluminium compound.

Hydrotalcite-like compounds can be made with any divalent and trivalent cations. Due to this, along with higher stability and longer lifetimes, catalysts prepared from hydrotalcites for redox reactions contain a large amount of transition metal (66-77%). These have been claimed, in many cases to have higher activity with respect to catalysts prepared by other more conventional techniques (such as impregnation or precipitation). [63]

Hydrotalcites may be doped with additional metals. This can be done to improve a catalytic effect [179] or to improve the material's thermal stability. One example is with hydrotalcites that were doped with zirconium. This is usually done to improve the basicity of the calcined product. The basicity of the lattice layer decreases as a result of lowering the partial charge on the oxygen atoms. Once calcined the basicity of the mixed oxide increases due to the formation of Zr^{4+}-O^{2-} acid-base pairs. [180] The lattice layers of hydrotalcite are usually comprised of Mg^{2+} and Al^{3+} cations or other bivalent and trivalent cations with similar ionic radii. The introduction of Zr^{4+}, with its comparatively larger ionic radius, induces a distortion of the brucite-like sheets and a heterogeneous distribution of charges. [180]

With the decrease of easily accessible fossil fuels, coupled with the rising demand for these fuels, chemicals and energy they provide, there is an increasing interest in renewable sustainable sources. [181-185] Biomass is being studied for its potential as a suitable candidate in this movement.[181, 184-186] The interest in biomass is due to it being mainly comprised of carbon, hydrogen and oxygen atoms making it a suitable source for the production of conventional and new chemicals and fuels.[181] Of these elements hydrogen is an important raw material.[187, 188] It is a clean fuel that can be used in fuel cells and internal combustion engines.[182, 187, 188] Currently the process of producing hydrogen is with catalytic reforming of methane, light hydrocarbons and naphtha.[182, 183, 187-189] This process uses non-renewable material and is accompanied by high CO_2 emissions.[182]

To create a renewable process of catalytic steam reforming the use of bio oils has been researched.[182, 183, 187, 189] Bio-oil is produced by the fast pyolysis of biomass and can be converted to hydrogen via catalytic steam reforming.[181, 182, 184, 187-189]

While this still produces CO_2, if integrated over a long-term growth cycle, the gases omitted during the process can be absorbed by plants used for the biomass feedstock creating carbon neutral net emissions.[182-184, 186]

Bio-oil is a mixture of simple aldehydes, ketones, phenols, alcohols and acids as well as more complex carbohydrate- and lignin-derived oligomeric materials emulsified with water.[181, 182, 187-189] With the addition of water, a water rich phase containing mostly carbohydrate-derived compounds can be separated out and this can be converted to hydrogen by steam reforming.[182, 187, 188] The majority of catalysts used in steam reforming are composed of Ni and Al, with Ni as the main active agent.[181, 185, 187-189] Ni based catalysts are also used for gasifying tar compounds and for CO_2 reforming of natural gases.[185, 187] Noble metals are more effective than Ni for steam reforming and less susceptible to carbon formation but due to their cost are not commonly used in an industrial application.[185, 187]

Steam reforming starts with hydrocarbons dissociatively adsorbing on the nickel sites,[187] while water dissociatively adsorbs on the aluminium sites which hydroxylates the surface.[187] Metal-catalysed dehydrogenation of the hydrocarbons forms adsorbed fragments at the nickel sites.[187, 189] Hydroxide then migrates to the nickel sites and is activated by the temperature, where it forms intermediates that lead to the forming carbon oxides.[187, 189]

An unwanted side effect of this process is the formation of carbon on the catalyst surface, leading to catalyst deactivation.[181-183, 185, 187, 189] There are different types of carbon formation; whisker like, encapsulating film and pyrolytic carbon, though all have the same consequences of deactivating the catalyst.[187] There are two strategies to inhibit this carbon formation. One strategy is to enhance steam adsorption on the

catalyst with the objective of gasifying any carbon or carbon precursors formed on the catalyst surface.[187, 189] Another strategy involves modifying the catalyst surface with the presence of other metals.[187, 188]

The use of magnesium has shown to enhance steam adsorption capability in nickel catalysts.[187, 189] Solid solutions of NiO/MgO have been reported to stabilize nickel compounds and prevent catalytic sintering.[183, 185, 187] Nickel aluminate has been shown to be highly active and resistant to deactivation.[190] Magnesium has also been used to form a magnesium/aluminium spinel that significantly changes Ni/Al_2O_3 catalytic properties.[187, 189]

In Chapter 2 it was discussed that thermally decomposed hydrotalcites that were made in a flow process were synthesised with kinetic control rather than thermodynamic control. In Chapter 3 it was discussed that the thermal decomposition of the hydrotalcites made in a continuous flow process do not appear to breaks down to form a spinel as batch synthesised hydrotalcites do. The flow synthesised material instead breakdown in to a mixture of aluminium and magnesium oxide. The continuous flow process provides three opportunities to add nickel to hydrotalcite. Doping would involve adding the nickel to the starting reagents. Nickel can be added to the collecting water and incorporated into the material though ion exchange in the washing process. Finally nickel can be added to hydrotalcite by impregnation once the hydrotalcite has been dried. The aim of this chapter is to explore these different methods of introducing nickel to hydrotalcite and creating a novel Ni/Al catalyst that is stabilised by magnesium. Their effectiveness in catalytic steam reforming will be the focus of study.

Experimental

Materials Preparation

The samples prepared under flow conditions were made using a system comprising of a peristaltic pump (Ismatec ISM597D) fitted with 3-stop 0.51 ID mm PVC tubes and a Y-mixer (PEEK 0.5 mm). The reactor comprised a 2 cm long 0.51 mm ID empty tube. The short length was due to the solid nature of the resulting product. As the hydrotalcite formed it slowed down in the tube. This caused a backup and eventually a blockage. The short reactor length prevented this from happening. However if the slurry was left just to collect in a dish it would reacted with itself to produce an unusable polymer. This was prevented by allowing the reactor output to collect in a crystallising dish of moving water (Figure 5). The two feed solutions were pumped at a rate of 1.5 mL min^{-1} at ambient temperature. The first solution contained magnesium and aluminium nitrates dissolved in water. The second solution contained sodium carbonate and sodium hydroxide dissolved in water. Due to the inability of monitoring the pH and the fast rate of reaction it was decided that the hydroxide would be added by stoichiometric formula, as the other reagents are added. Following filtration through a Buchner flask the product was dried in air at 85 ^{o}C for 12 h.

It was attempted for all samples to attain similar amounts of nickel in the material. The material made by ion exchange (here after referred to as WP1-IE) had nickel nitrate added to the water of the collecting dish. This sample was used as the standard for nickel concentration to be achieved with the other samples. When doping the hydrotalcite, the nickel nitrate was added to the solution of magnesium and aluminium nitrate. When nickel was doped in the starting reagent (the sample

now referred to as WP1-D1) the concentration of nickel was found to be low. Another doped sample was made with double the amount of nickel in the starting material (the sample will now be referred to as WP1-D2). Impregnated samples had nickel treatment occur after the material had been dried (WP1-E) by re-slurrying in a nickel solution. This was repeated on a sample that had been calcined at 500 ^{o}C for 12 hrs (WP1-Ec) and on a sampled that had been washed for 2 hrs prior to drying (WP1-Ew).

Table 14. Composition of reagents for the nickel hydrotalcite catalysts

<table>
<tr><th rowspan="2">Sample</th><th colspan="5">Molar ratios of the ions used as a reagents</th></tr>
<tr><th>Mg^{2+}</th><th>Al^{3+}</th><th>Ni^{2+}</th><th>CO_3^{2-}</th><th>OH^-</th></tr>
<tr><td>WP1-IE</td><td rowspan="6">3</td><td rowspan="6">1</td><td rowspan="5">0.3</td><td rowspan="6">0.5</td><td rowspan="6">8</td></tr>
<tr><td>WP1-E</td></tr>
<tr><td>WP1-Ec</td></tr>
<tr><td>WP1-Ew</td></tr>
<tr><td>WP1-D1</td></tr>
<tr><td>WP1-D2</td><td>0.6</td></tr>
</table>

Procedures of analysis

ICP-OES were performed by Exeter Analytical using a PE Optima 5300 Dual View ICP-OES Spectrometer. Samples were weighed to 6mg and placed into plastic microwave tubes and mixed with 5ml nitric acid Analar grade and 1ml hydrogen peroxide Analar grade. The samples were digested using an Anton Paar Multiwave 3000 microwave digester. The microwave method typically lasted for an hour and a half. A maximum temperature of 200°C is achieved. When solutions were clear the samples are transferred to 50ml centrifuge tubes 0.5ml of internal standard (yttrium) added to each tube. The solutions were aliquoted to 50ml with de-ionised water. The samples were run against calibration standards of known concentrations. Standards containing 10, 30 and 50ppm of Al, Mg and Ni were used in this analysis. A calibration curve was constructed from the standards against which the intensity readings of the samples could be read.

Analyses of carbon, hydrogen and nitrogen were performed by Exeter Analytical using a CE 440 Elemental Analyser. Samples were weighed around 1-2 mg and placed into a high temperature furnace. Once combusted in oxygen the products were passed through oxidation reagents to produce carbon dioxide, water, nitrogen and nitrogen oxides. The gases were then passed over copper to remove excess water and reduce the nitrogen oxides to elemental nitrogen. The detection of the combustion products was produced by using thermal conductivity.

Specific surface area and porosity of materials were studied by cryogenic adsorption of nitrogen. The samples were added to sample tubes which were then fitted with a glass filler rod and a seal frit. They were prepared by heating from room temperature to 150 C at 10 C/min whilst evacuating at a rate of 5 mm Hg/s, until a

pressure of 10 um Hg was achieved. The temperature was then increased to 200 C (at 10 C/min) and held for 1 hour. The sample was then cooled and the sample tube backfilled with nitrogen, and weighed to obtain the dry mass used in subsequent calculations. The cold and warm free space was measured automatically by filling the sample tube with helium prior to analysis.

The sample tube was immersed in a bath of liquid nitrogen, and fitted with an isothermal jacket to maintain the level of the cryogen around the tube. Full nitrogen adsorption isotherms were collected.

BET analysis was performed on adsorption data in the relative pressure range 0.06 to 0.26. BJH analyses were carried out on the adsorption from 0.29 – 1.00, and desorption data from 0.92 – 0.1. These determinations were performed by Ben Douglas in the Department of Chemistry, University of Warwick. The instrument is a Micromeritics ASAP 2020 Accelerated Surface Area and Porosimetry System, and the software is ASAP 2020 v3.03.

X-ray diffraction patterns were collected using a Bruker D8 Advance X-Ray Diffractometer, operating in step scan mode, with Co Kα radiation (1.78897Å). Patterns were collected in the range 5 to 75° 2θ with a step size of 0.02° and a rate of 0.2s per step. Samples were crushed into a powdered form. The reflection positions were refined and calculated using the Celref v3.[92]

For the catalytic testing 0.3 g of the catalyst was added to 1 cm^3 silicon dioxide (quartz sand). The gas stream was 97.5 % inert helium (He), 0.5 % ethanol (C_2H_5OH) and 2 % water (H_2O).

Results and Discussion

X-Ray Diffraction

Formation of hydrotalcite was checked for by X-ray diffraction. Hydrotalcite has a unique diffraction pattern that can be easily identified. All the nickel hydrotalcites exhibited the typical diffraction patterns corresponding to hydrotalcite. They displayed slimmer symmetric reflections in the low 2θ range and at high 2θ values the reflections became weaker and less symmetric.[92] The indices of reflection (003) and (006) were clearly identifiable with reflections at 11.1° and 22.7° respectively.[86] The reflections of (009) and (102) were overlapped producing a broader signal at 34.5°.[86, 92] The (105) reflection was found at 38.6° and reflection (108) was found at 45.8°. [86] Two reflections of (110) and (113) could easily be identified at 60.3° and 61.6°. [86, 92]

The intensities of the peaks were different but the information of the structure is gained from the width of the peaks, rather than the height. It should be noted that only WP1-E and WP1-Ew had any definition in the (110) and (113) reflections.

Table 15. Table of the reflections seen in the diffraction patterns of nickel-hydrotalcite catalysts.

Sample	Reflections hkl						
	(003)	(006)	(009)	(105)	(108)	(110)	(113)
WP1-IE	11.7	23.1	35.1	39.5	47.1	61.6	
WP1-D1	11.6	22.8	34.4	38.5	45	61.2	
WP1-D2	11.5	22.8	34.7	38.4	44.5	61.2	
WP1-E	11.3	22.7	34.6	38.4	44.6	60.6	61.3
WP1-Ec	11.1	22.3	34.5	38.4	44.6	60.9	
WP1-Ew	11.2	22.6	34.5	38.4	44.6	60.5	61.8

Table 16. Table of the cell parameters and crystallite sizes of the nickel-hydrotalcite catalysts.

Sample	Cell Parameters (nm)			Crystallite Size (nm)
	a	b	c	
WP1-IE	0.31	0.31	2.26	3.34
WP1-D1	0.32	0.32	2.28	3.72
WP1-D2	0.32	0.32	2.31	4.19
WP1-E	0.32	0.32	2.35	4.75
WP1-Ec	0.32	0.32	2.38	5.03
WP1-Ew	0.32	0.32	2.37	5.64

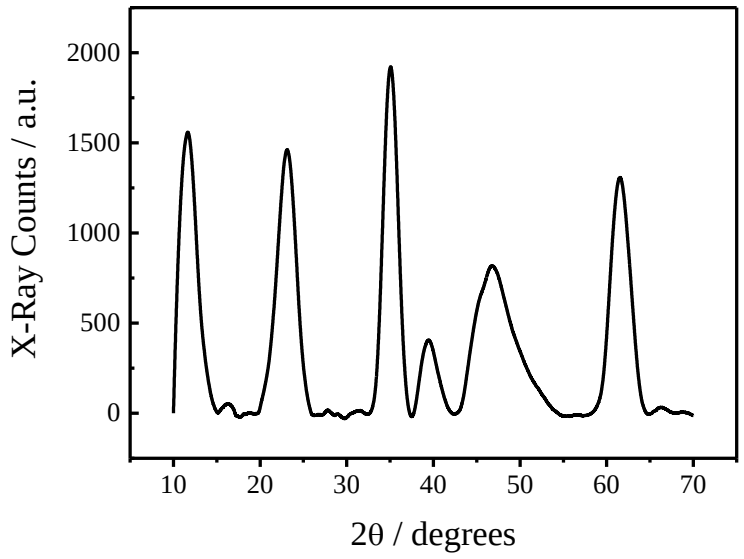

Figure 51. X-Ray diffraction pattern of the Mg-Al-Ni hydrotalcite with the nickel being added by Ion Exchange (WP1-IE)

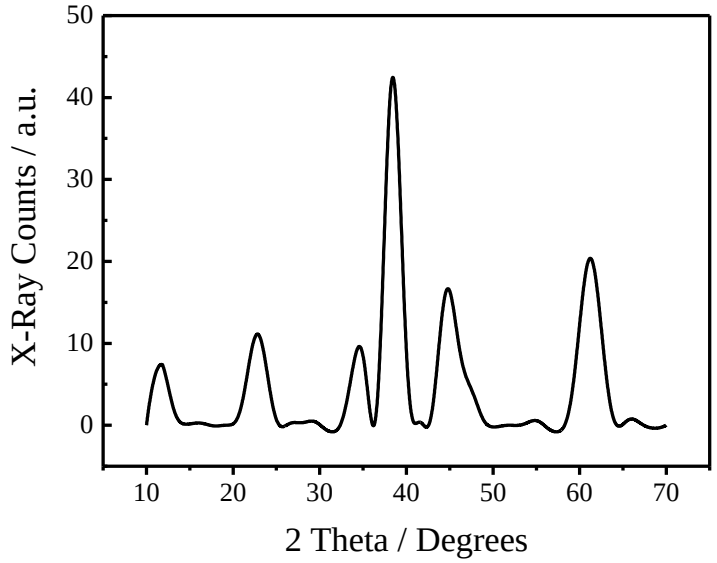

Figure 52. X-Ray diffraction pattern of the Mg-Al-Ni hydrotalcite with the nickel being added by doping (WP1-D1)

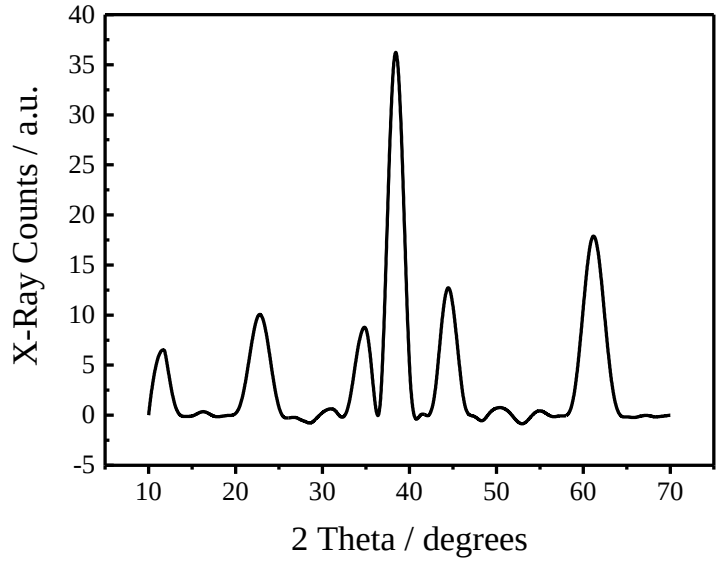

Figure 53. X-Ray diffraction pattern of the Mg-Al-Ni hydrotalcite with the nickel being added by doping (WP1-D2)

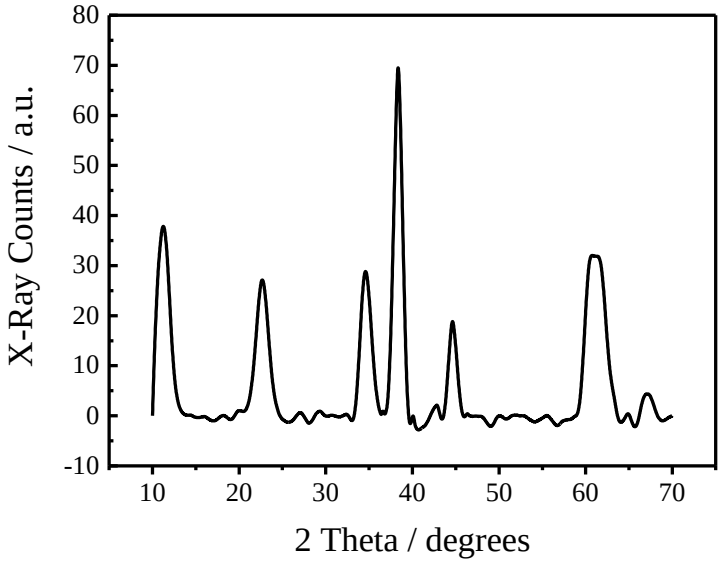

Figure 54. X-Ray diffraction pattern of the Mg-Al-Ni hydrotalcite with the nickel being added by impregnation (WP1-E)

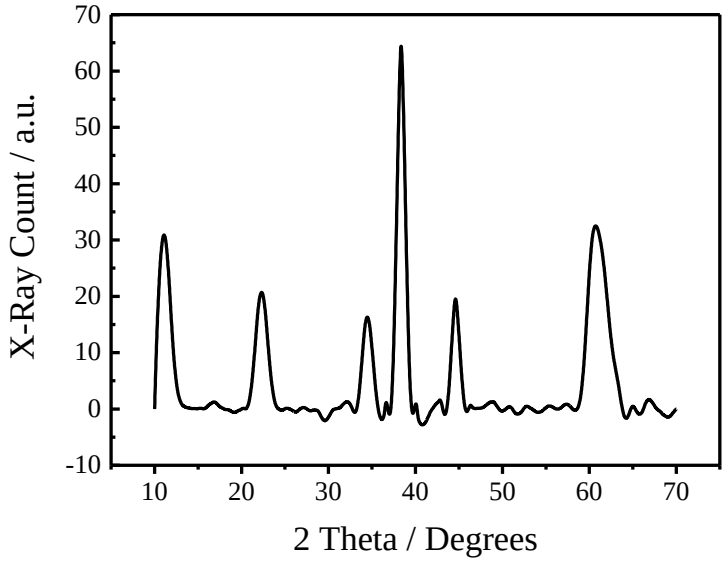

Figure 55. X-Ray diffraction pattern of the Mg-Al-Ni hydrotalcite with the nickel being added by impregnation (WP1-Ec)

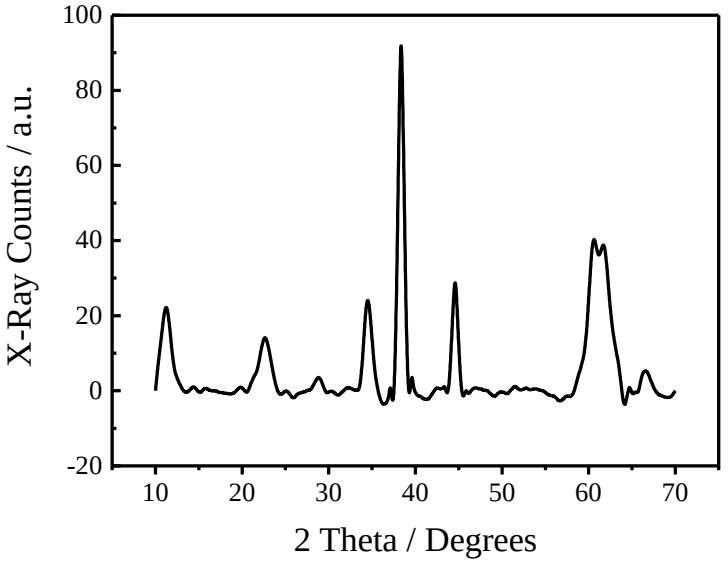

Figure 56. X-Ray diffraction pattern of the Mg-Al-Ni hydrotalcite with the nickel being added by impregnation (WP1-Ew)

Inductively coupled plasma – optical emission spectroscopy (ICP-OES) / Carbon, Hydrogen and Nitrogen analysis (CHN)

WP1-IE had nickel added to the washing water and was washed for 2 h, a similar method used to create the HTCF2h with pure water. This gave a metal ratio similar to HTCF2h. The carbon concentration was lower than it was for the HTCF2h and the nitrogen was higher. This was likely due to the addition of nickel as nickel nitrate.

WP1-D1 and D2 were not washed for any extended period of time, in the manner of HTCFw, the nickel being added to the hydrotalcite in the starting reagents. The doped hydrotalcite had a similar metal ion ratio as HTCFw. The amount of carbon was lower than would be expected again, just as the nitrogen was higher. This again can be attributed the use of nickel nitrate for doping. It was seen clearly that when the nickel nitrate is doubled in WP1-D2 the carbon content decreased by roughly the same amount as the nitrogen increased. As all other reagents, except the nickel nitrate, were kept constant the change in percentage value can be attributed to the increased presence of nickel nitrate.

WP1-E was an unwashed dry powder when it was returned to water to be washed in a nickel solution. It would appear that metals in WP1-E have been washed out as magnesium content was significantly less than aluminium. Even when accounting for the uptake of nickel, the amount of M^{2+} was far too low. This was likely due to the small pore volumes seen in Chapter 2 of the unwashed flow samples. This would mean that the interaction of the nickel would be only on the surface of the particle. The carbon content was significantly lower than would be expected. It was likely that the washing replaced the bicarbonate found in unwashed flow samples with the nitrate in the nickel nitrate.

WP1-Ec was also a dry powder that was calcined at 500 ^{o}C before being added to a nickel solution. Hydrotalcites are known to return to their original structure from their mixed oxides form when rehydrated. This allowed the uptake of nickel into the structure when the lattice layer reformed. This would give the sample characteristics closer to batch prepared material. The carbon content was low for two reasons. The calcination process of hydrotalcite goes through decarbonation driving off the carbon as carbon dioxide. Normally this can be replaced during reforming with the carbon dioxide in the air being sufficient. In this case the nitrate was already present in the reforming taking the place of the carbonate in the layer.

WP1-Ew was a dry sample that was washed for 2 h before being dried. After it had been dried before it was added to the nickel solution. Due to reforming of the sample in the washing process, the carbonate becomes a bridging carbonate instead of being in the bicarbonate form found in the unwashed samples. The sample was dry when added to nickel but the sample was in a more stable form, so neither the metals or the carbon were easy to replace with nitrate.

Table 17. Table showing the different component of each catalyst by percentage

	ICP			CHN		
	Mg (%)	Al (%)	Ni (%)	C (%)	H (%)	N (%)
WP1-IE	13.41	12.34	8.29	1.50	3.29	1.34
WP1-D1	14.55	7.26	4.71	1	2.46	4.74
WP1-D2	12.46	6.37	8.31	0.67	2.43	5.06
WP1-E	8.30	18.37	5.94	0.13	3.01	3.47
WP1-Ec	13.44	18.23	9.01	0.40	2.36	2.10
WP1-Ew	16.78	8.54	6.87	1.30	3.05	2.82

Table 18. Table showing the metal ratios found in each of the catalysts.

	Ratio of the metals (Mg:Al:Ni)	Ratio of the metals (M^{2+}:M^{3+})
WP1-IE	1.1:1:0.7	1.8:1
WP1-D1	2:1:0.7	2.7:1
WP1-D2	2:1:1.3	3.3:1
WP1-E	0.5:1:0.3	0.8:1
WP1-Ec	0.7:1:0.5	1.2:1
WP1-Ew	2:1:0.8	2.8:1

Surface area and pore size distribution analysis

The samples displayed a Type IV isotherm like the standard hydrotalcites discussed in Chapter 2. [76, 132] All the samples except for the doped samples (WP1-D1 and WP1-D2) had larger surface area which would indicate that the material had macropores but the hysteresis also indicates that the material had mesopores in its structure. The small surface area of WP1-D1 and WP1-D2 would indicate that the material is a non-porous material rather than the macroporous material. This smaller surface area is analogous to the HTCFw samples made in Chapter 2 which also exhibit a small surface area.

Table 19. BET surface area of Ni-HTC samples

Sample	BET Surface Area ($m^2 g^{-1}$)
WP1-IE	88
WP1-D1	8
WP1-D2	9
WP1-E	48
WP1-Ec	20
WP1-Ew	23

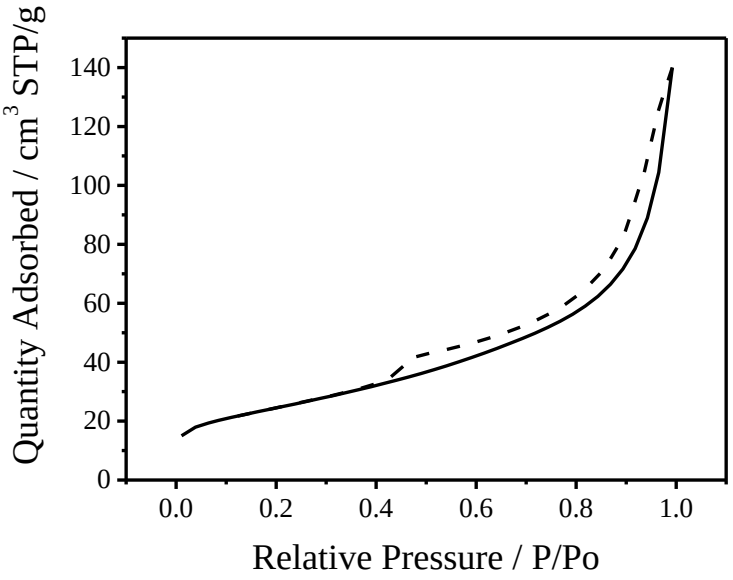

Figure 57. Isotherm for WP1-IE. Adsorption (solid line) and desorption (dashed line)

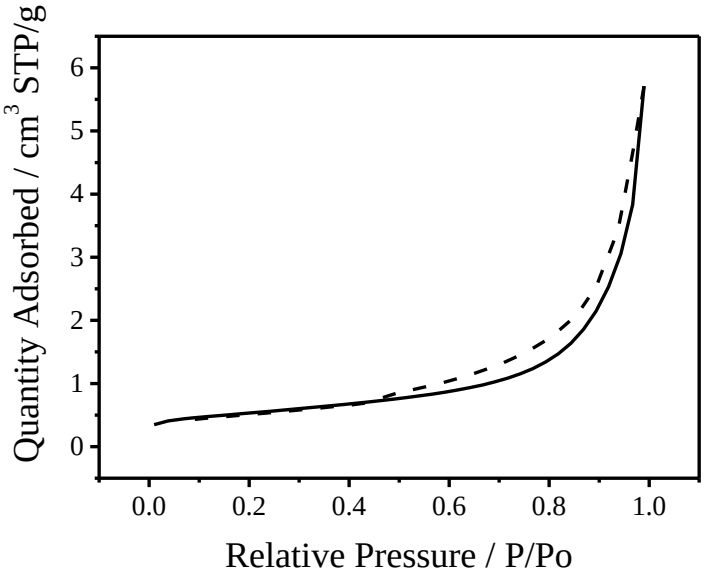

Figure 58. Isotherm for WP1-D1. Adsorption (solid line) and desorption (dashed line)

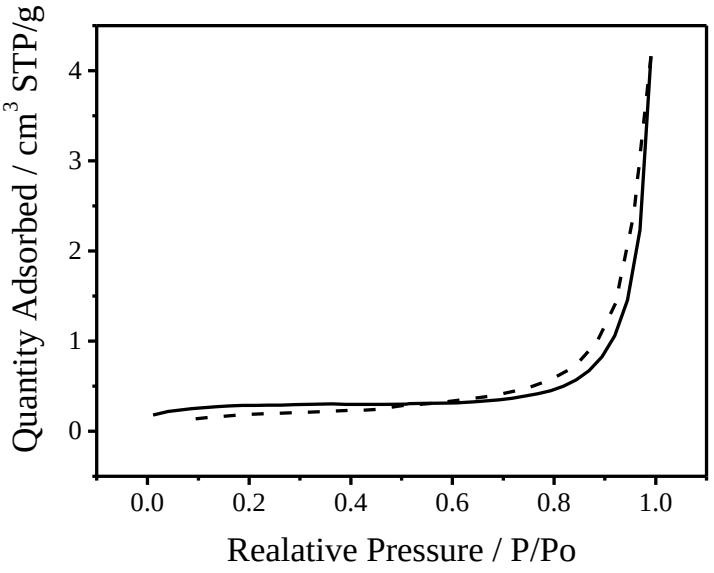

Figure 59. Isotherm for WP1-D2. Adsorption (solid line) and desorption (dashed line)

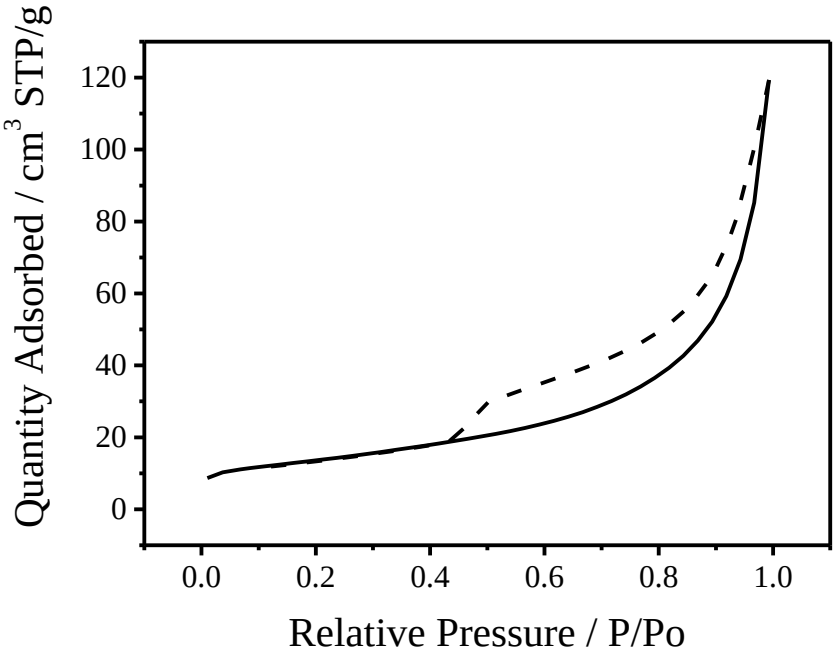

Figure 60. Isotherm for WP1-E. Adsorption (solid line) and desorption (dashed line)

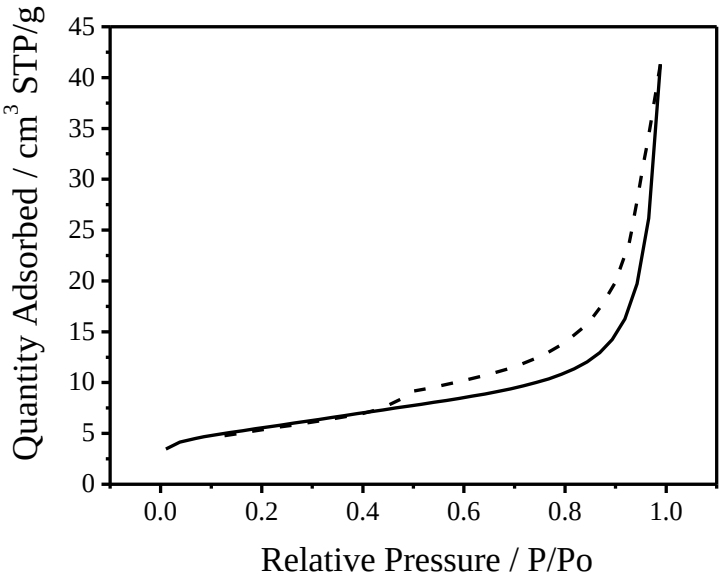

Figure 61. Isotherm for WP1-Ec. Adsorption (solid line) and desorption (dashed line)

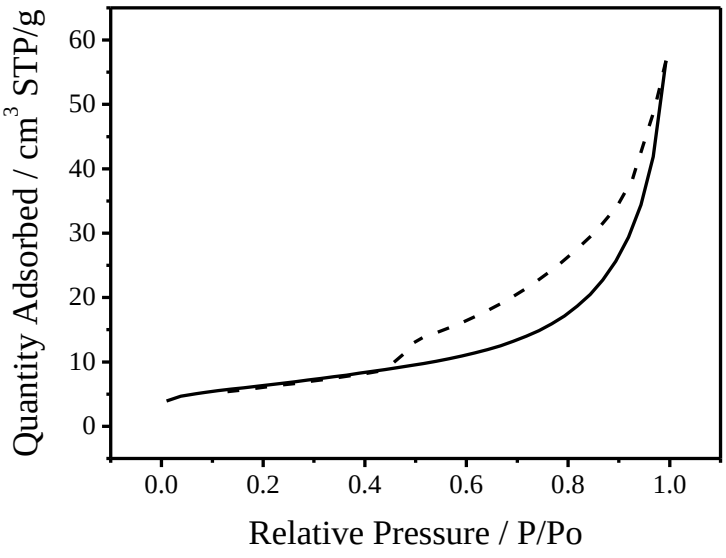

Figure 62. Isotherm for WP1-Ew. Adsorption (solid line) and desorption (dashed line)

The BJH method was used to determine the pore volume and the distribution of the size. Sample WP1-IE displayed two peaks indicating that pores of two sizes had a

prevalent existence within the structure. The first peak showed a pore diameter of 5 nm with a pore volume of 0.121 cm^3 g^{-1}. The second peak had a diameter of 41 nm with a pore volume 0.127 cm^3/g. The presence of two pore diameters was likely due to nickel within in the lattice. It was seen in Chapter 2 that when a flow made sample was washed it is able to rearrange to a more favourable configuration. This would require a certain amount of dissolution and re-precipitation. This process would not be taking place on an atomic level as parts of the lattice would already be in the low energy state with the aluminium "in phase" as described in Chapter 2. The re-precipitation of the material would allow for the incorporation of nickel into lattice with an uneven distribution. The smaller pore size had been recorded before in the interaction of nickel and alumina in a lattice [191] while the larger pores are more like the pore distribution seen in hydrotalcite.

Samples WP1-D1 and WP1-D2 had pores that were much smaller than the other samples, much like the unwashed sample HTCFw of Chapter 2. For WP1-D1 the peak width the pore was 14 nm and had a volume of 0.016 cm^3/g. For WP1-D2 the peak width the pore was 17 nm and had a volume of 0.01 cm^3/g. This would support the idea that unwashed flow samples only had more inclination to form mesopores, than to form macropores resulting in the lower surface area. The nickel catalysts had a larger surface area than HTCFw of Chapter 2 due to the larger nickel atoms being included in the lattice layer, distorting it and increasing the pore volume. This was evident by an increase in pore size distribution corresponding with an increase in the content of nickel seen in the ICP analysis.

Samples WP1-E and WP1-Ew had similar distribution patterns. The peak width of the pores was 23 nm for WP1-E with a volume of 0.07 cm^3/g. WP1-Ew had a peak

width of 20 nm with a volume of 0.044 cm^3/g. The WP1-E sample was an unwashed flow material prior to impregnation with nickel so would be expected to have the smaller pores, yet the pores of washed WP1-Ew were smaller. The pore sizes for both catalysts were significantly smaller than HTCFw and HTCF2h. It would suggest that the addition nickel material impregnated on the surface of the particles filling the pores.

WP1-Ec had been an unwashed flow sample that had been calcined, before impregnation with nickel. Due to the calcination the material had been rendered to the mixed oxide form of the material before being added to the nickel solution. These mixed metal oxides had also shown the capacity to be regenerated back to a hydrotalcite structure by rehydrating the metal oxides through contact with water. [89, 92] It was through this regeneration that the nickel became incorporated into the structure. As the structure that was made in continuous flow was destroyed, a new structure was formed from the rehydration of mixed oxides in the batch process environment. The pore size distribution of this material resembled that of HTCB in Chapter 2. The peak pore diameter was 42 nm and the pore volume 0.034 cm^3/g.

Table 20. Summary of the pore distribution from the BJH analysis.

	Pore Diameter (nm)	Pore Volume (cm^3/g)
WP1-IE	5	0.121
	41	0.127
WP1-D1	14	0.002
WP1-D2	17	0.010
WP1-E	23.2	0.070
WP1-Ec	41.56	0.034
WP1-Ew	19.5	0.044

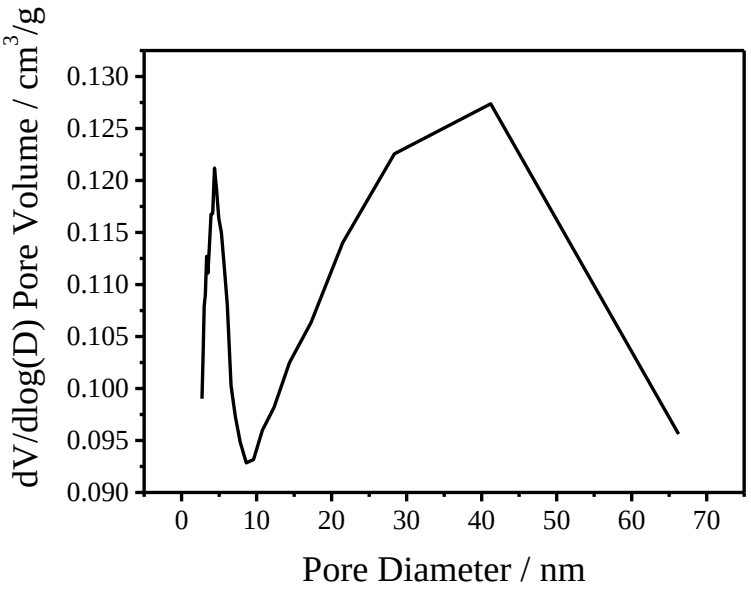

Figure 63. BJH analysis of the pore distribution of WP1-IE

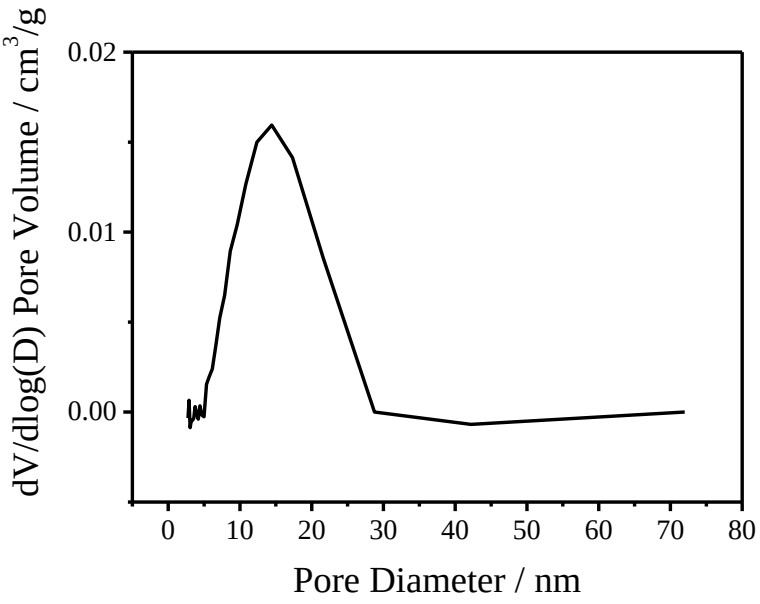

Figure 64. BJH analysis of the pore distribution of WP1-D1

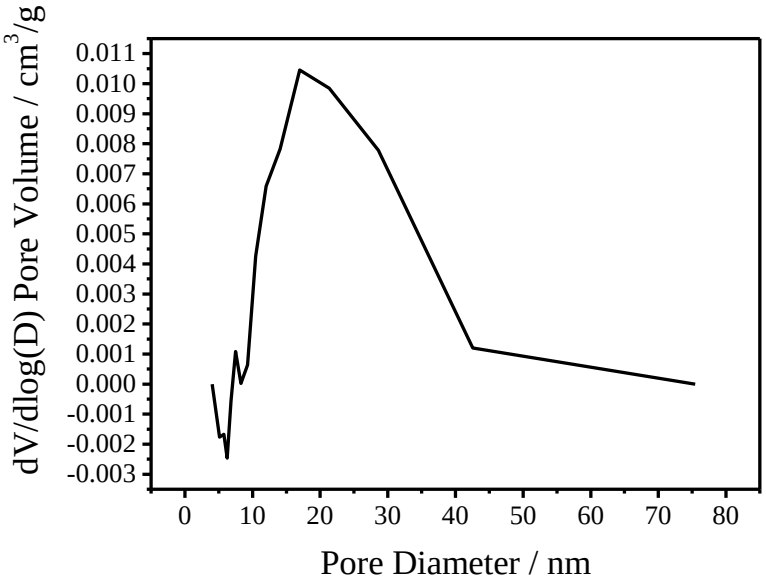

Figure 65. BJH analysis of the pore distribution of WP1-D2

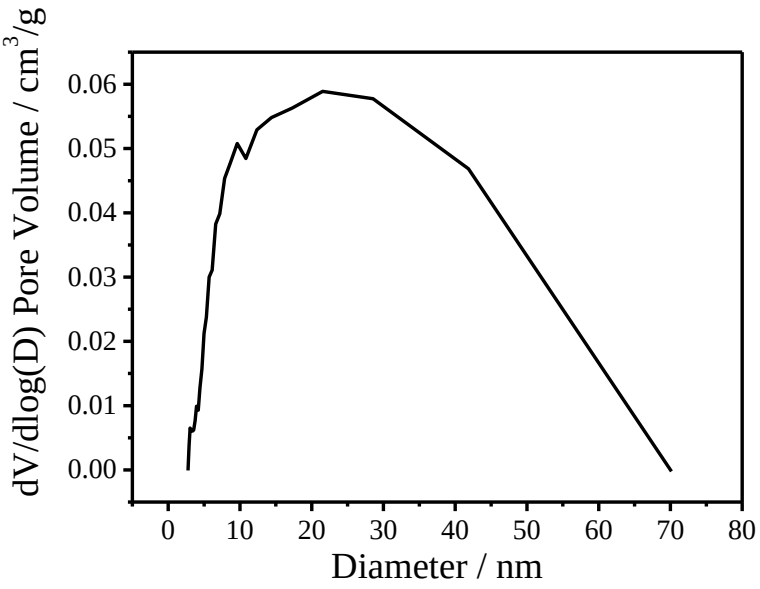

Figure 66. BJH analysis of the pore distribution for WP1-E

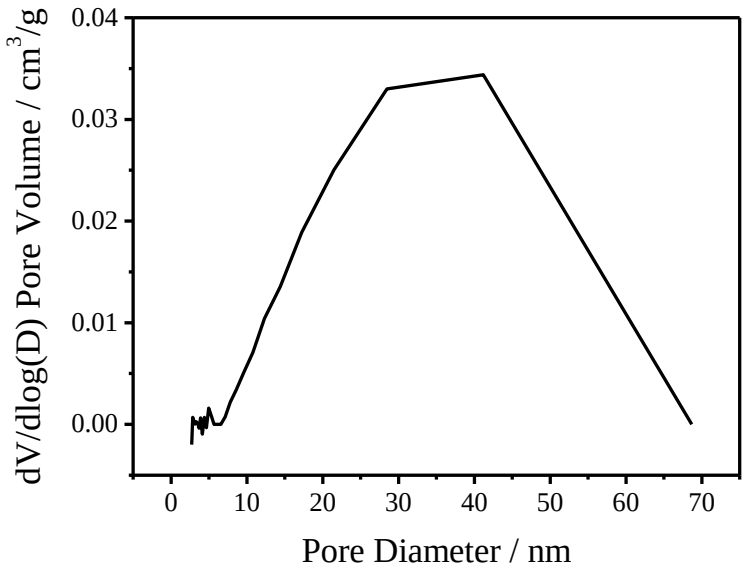

Figure 67. BET analysis of the pore distribution of WP1-Ec

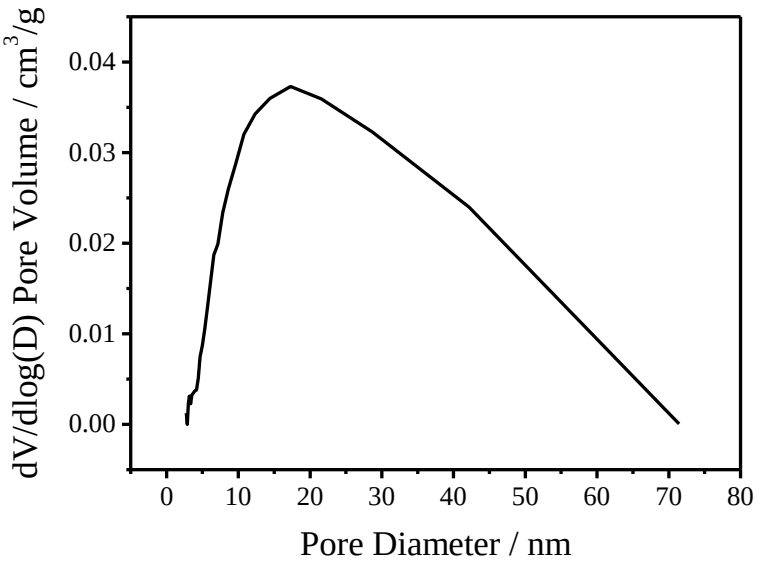

Figure 68. BJH analysis of the pore distribution of WP1-Ew

Thermogravimetric analysis

As with the hydrotalcites made in Chapter 2, the TGA curves of these materials showed weight loss occurring in three distinct stages. Weight loss between ambient temperature to 250 °C can be attributed to the loss of external surface water and water found in the interspatial layer, along with a partial dehydroxylation occurring simultaneously.[74, 98] The DTA scan showed two definite endothermic peaks. A broad curve appeared at the beginning of the scan in the range of the water removal.[116] The broad curve displayed by the samples showed two distinct areas of loss. Surface water was removed first, and then water from within the lattice, needing more heat, was removed.

The second region, between 250 to 430 °C showed dehydroxylation and the decarbonation of the lattice layer.[89] The large peak, seen in the DTA, was the evolution of carbon dioxide by the interspatial carbonate anions [76, 116] in the range

that the lattice collapses (see XRD above). For the samples WP1-D2 and WP1-Ec, this second peak had a shoulder indicating two unresolved peaks. Forano *et. al.* states that the first of these was the dehydroxylation of the aluminium. The second peak represented the dehydroxylation of magnesium and decarbonation of the interspatial carbonate anions. [116] The third region, at temperatures above 430 °C, was attributed to the loss of any volatile species and the decomposition of mineralised magnesium carbonate.[76, 92, 98]

For the nickel hydrotalcites the DTA showed a fourth area found in 730 and 800 °C region. It had been reported, in the literature, that this was the temperature region that nickel oxide and nickel aluminium spinel ($NiAl_2O_4$) final separate [192, 193] WP1-D1 and WP1-D2 had a weight loss that accompanied this region though none of the literature reported a weight loss in this area. It was only seen for the doped samples which had so far behaved in a similar fashion to HTCFw. If this tread continued WP1-D1 and WP1-D2 would not form a nickel aluminium spinel, but form nickel and aluminium oxide. At these temperatures it has been seen that these oxide will reduce to form nickel aluminide (NiAl).

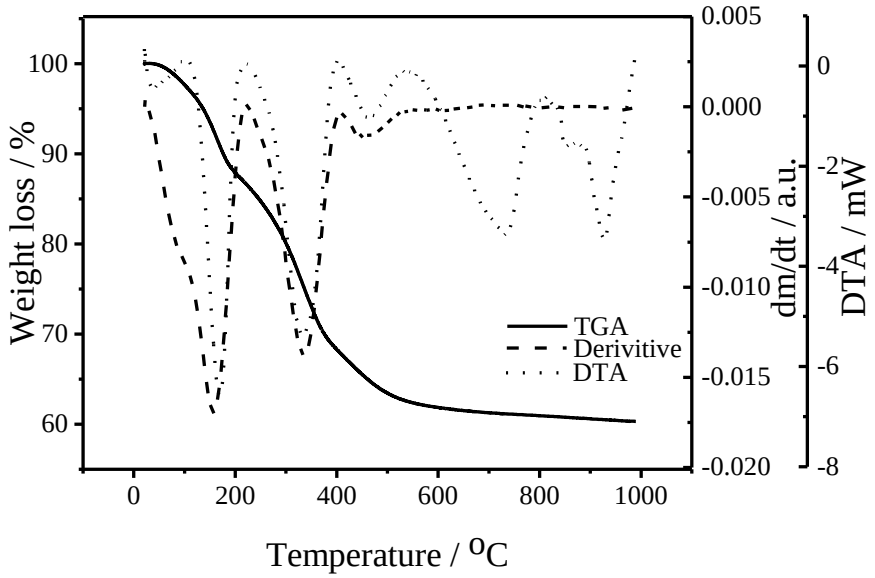

Figure 69. TGA and DTA data for Mg-Al-Ni hydrotalcite made with the nickel being added by Ion Exchange (WP1-IE)

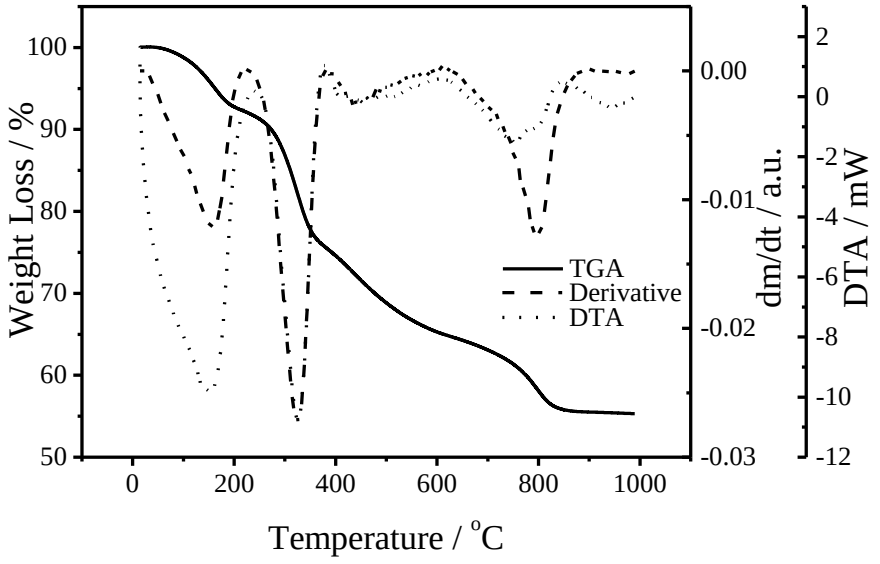

Figure 70. TGA and DTA data for Mg-Al-Ni hydrotalcite made with the nickel being added by doping (WP1-D1)

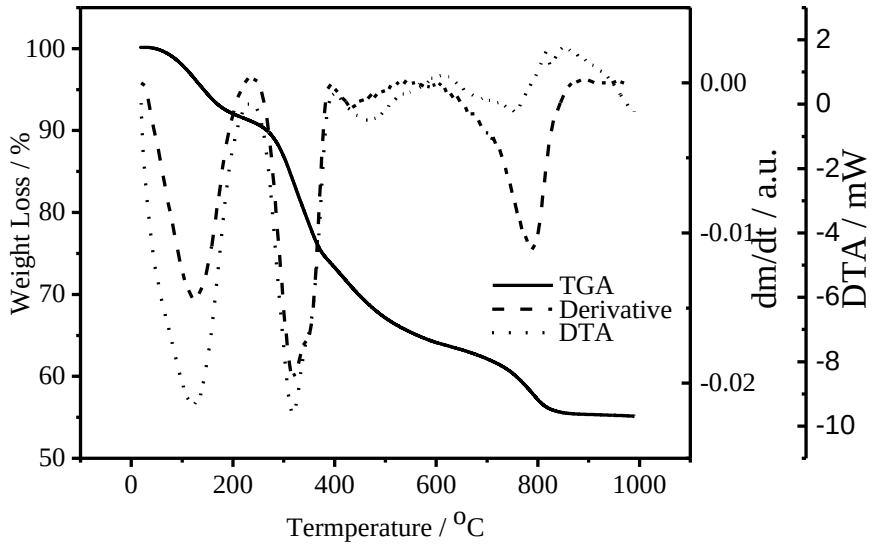

Figure 71. TGA and DTA data for Mg-Al-Ni hydrotalcite made with the nickel being added by doping (WP1-D2)

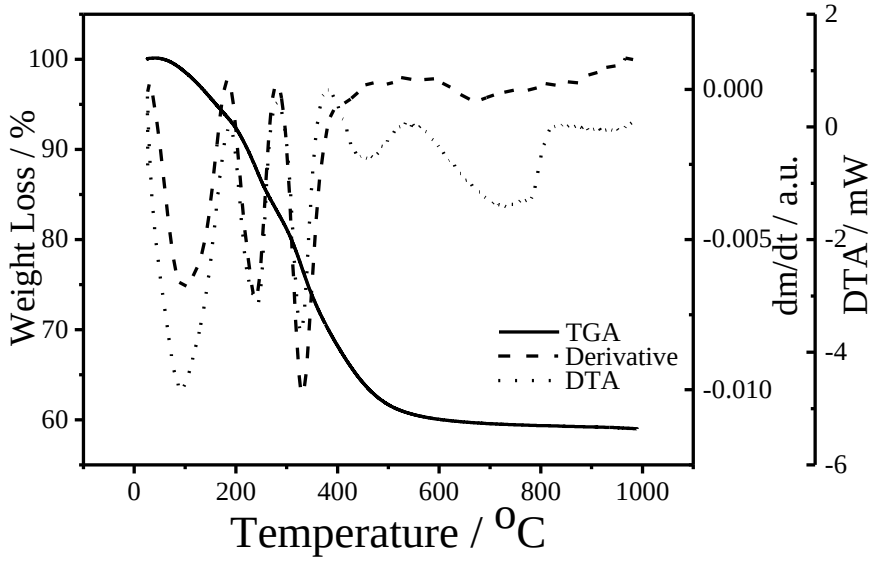

Figure 72. TGA and DTA data for Mg-Al-Ni hydrotalcite made with the nickel being added by doping (WP1-E)

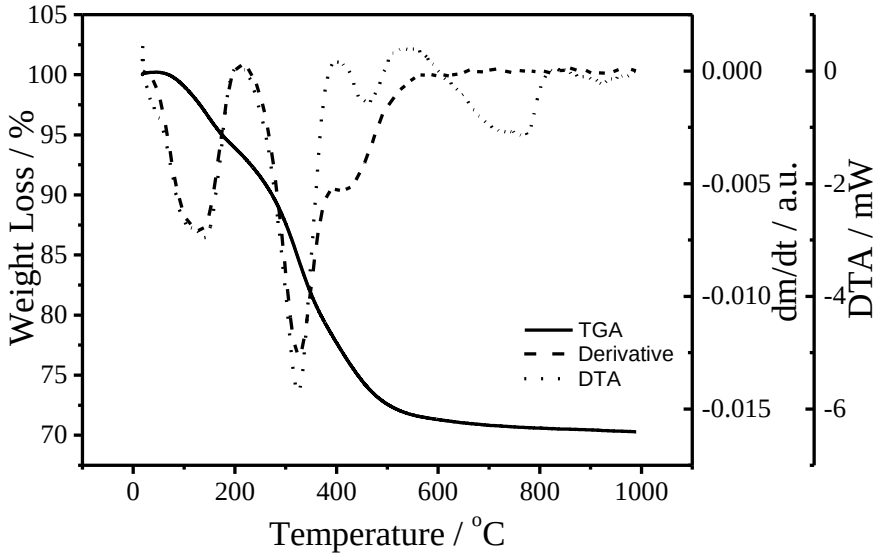

Figure 73. TGA and DTA data for Mg-Al-Ni hydrotalcite made with the nickel being added by doping (WP1-Ec)

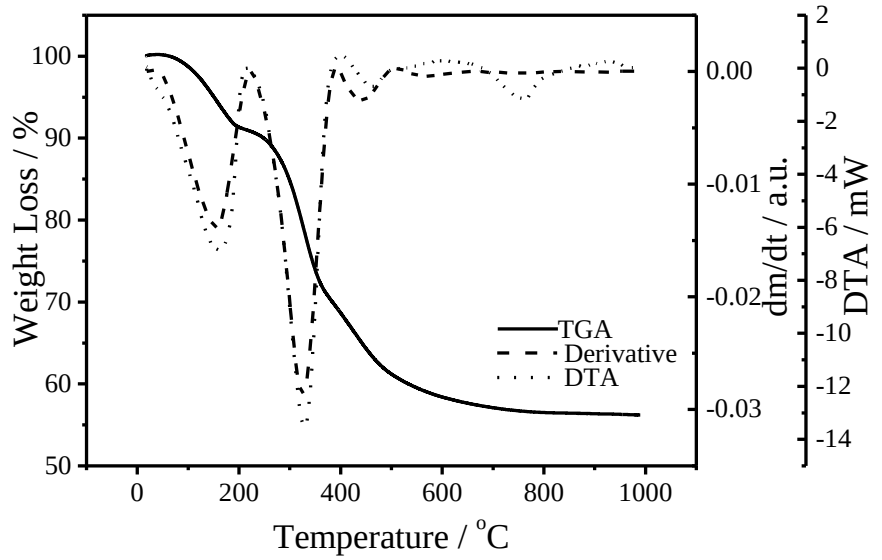

Figure 74. TGA and DTA data for Mg-Al-Ni hydrotalcite made with the nickel being added by doping (WP1-Ew)

Catalytic Testing

Of the samples made, two were used for catalytic testing. This was due to the samples having similar nickel content. The samples used were WP1-D2 and WP1-Ec. Both samples tested showed to be catalytically active.

Reducibility of the catalyst was monitored by temperature programmed reduction (TPR). This is a technique used to find the most efficient reduction conditions. The oxidised catalyst precursor was submitted to a programmed temperature rise while a reducing gas mixture was flowed over it. The maximum temperature peak of WP1-D2 was seen at 507 °C. It has been reported that it was at this temperature that only metal oxide will be reduced.[194, 195] WP1-Ec however displayed two maximum peaks at 538 and 1266 °C. While the first maximum temperature peak is the reduction of the metal oxides displayed in WP1-D2 the second was attributed to the reduction of a Ni/Al spinel. [195] As proposed in Chapters 2 and 3, unwashed flow samples that were produced by kinetic control, reduce to a mixed oxide form due to the lack of Al-O-Al bonds linking the lattice layers together. WP1-D2 was a doped sample that was synthesised in this manner. It was unwashed and subjected to kinetic control only. WP1-Ec was synthesised in the same manner, however the sample was calcined prior to being added to a nickel solution for the impregnation process. The rehydration process would have caused the mixed oxides to regenerate the original hydrotalcite structure incorporating the nickel in the process. This process was performed in batch and the formation of the structure became subject to thermodynamic control. It had been discussed that material produced by thermodynamic control will form a spinel through the linking oxygen bridges. The TPR profile adds support to this theory.

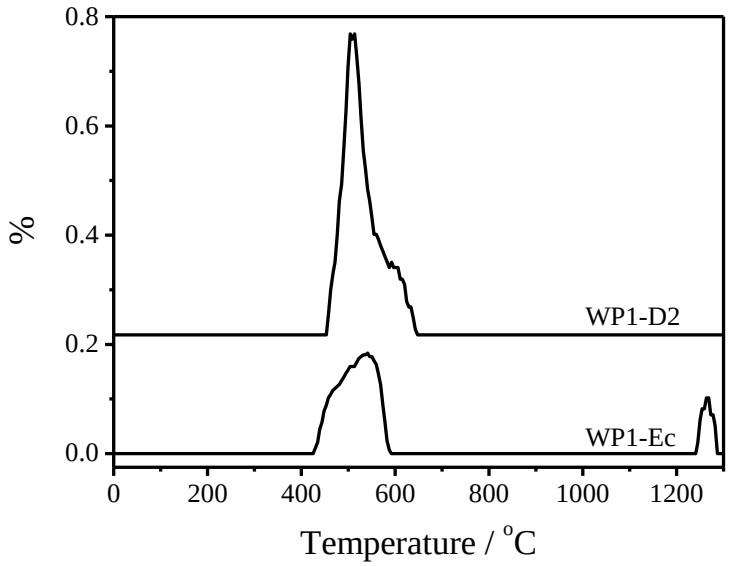

Figure 75. Reduction of catalysts WP1-D2 and WP1-Ec.

The catalyst WP1-D2 displayed a better activity than WP1-Ec. WP1-Ec took longer to reach its maximum activity but still did not reach the same level of activity as WP1-D2. At around 700 °C WP1-D2 produced a large amount of methane without decreasing the quantity of hydrogen produced. It was unclear why this happened and something that *in situ* spectroscopy could possibly better account for. It is around this temperature that the fourth weight loss region is found in TGA of WP1-D2. It was suggested that the only nickel material that would remain at those temperature would be nickel aluminide (NiAl). This could also be the case here. Since the nickel aluminide is a metal alloy it was already in the reduced state and would not be seen in the TPR. It has been reported that an increased metallic quality in the catalyst facilitates the cleaving of the carbon-carbon bond. WP1-Ec did not show any of the additional loss of weight in this temperature range but the DTA does show the arrangement and separation of metal oxides and spinel forms. Spinel is known to be

inactive unless when reduced. Lower activity of WP1-Ec may be due to not all the nickel being reduced because of this spinel form.

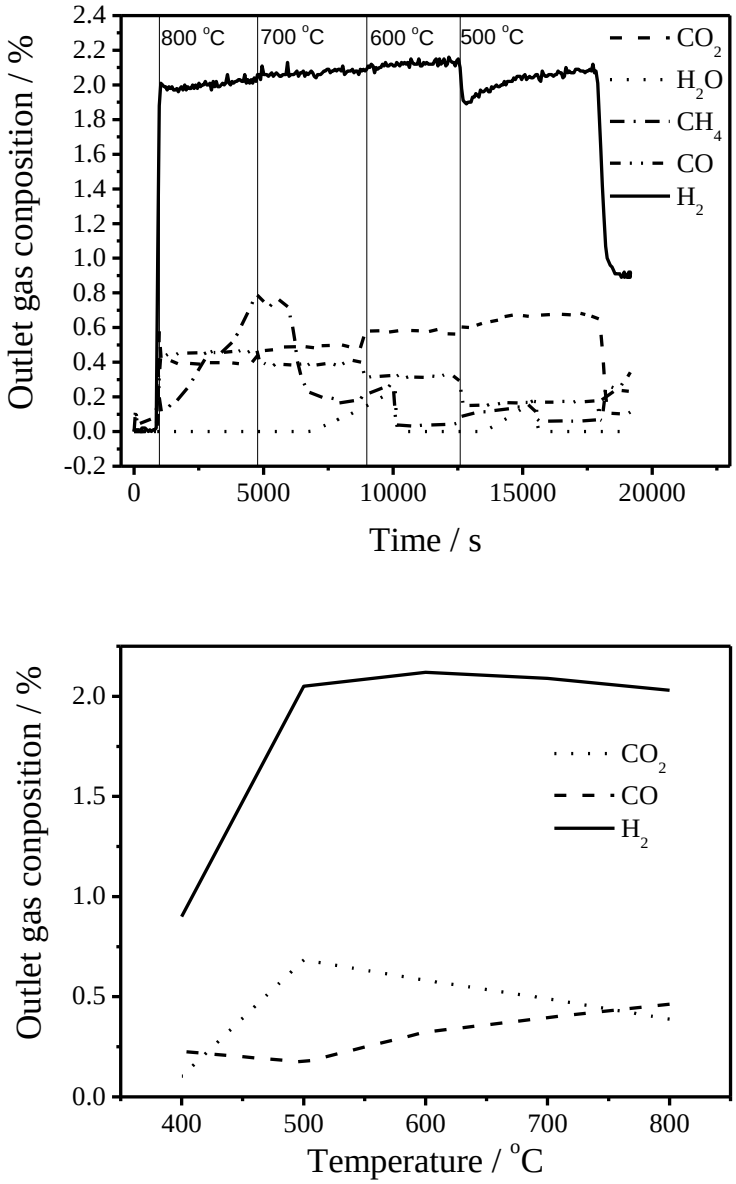

Figure 76. Hydrogen release from the catalyst WP1-D2 over time.

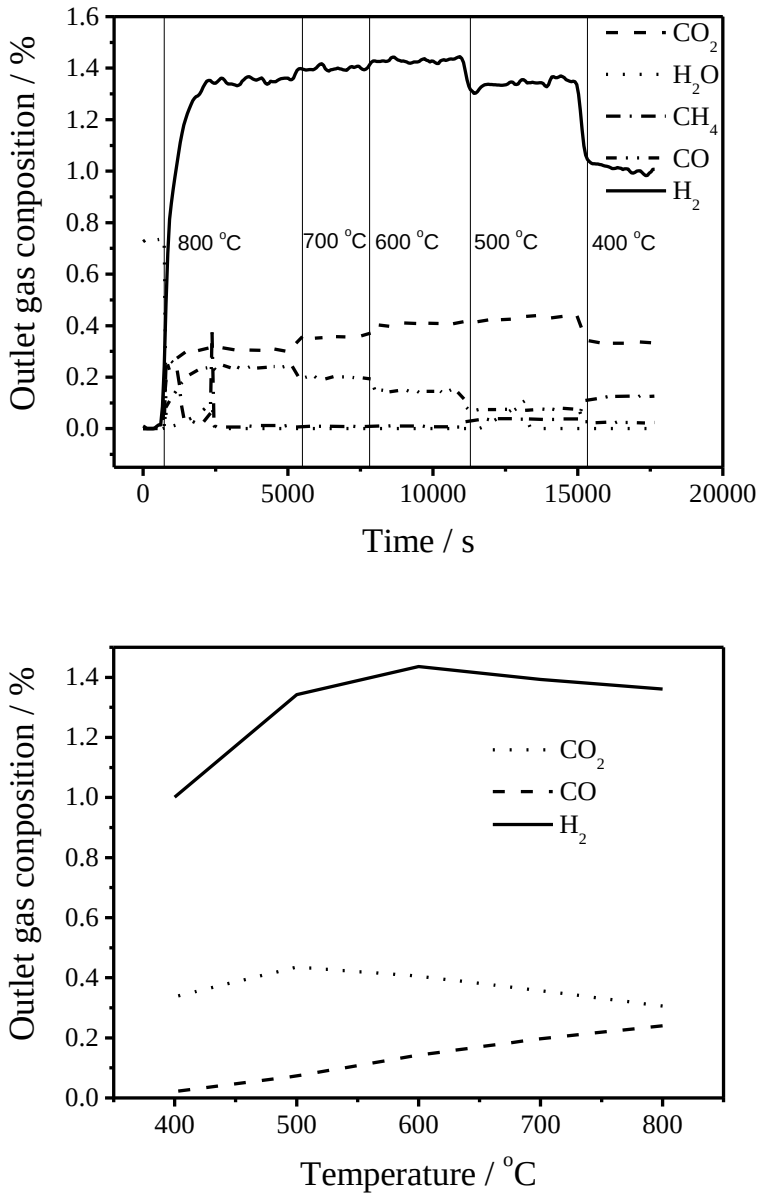

Figure 77. Hydrogen release from the catalyst WP1-Ec over time.

When compared with other catalysts used for ethanol steam reforming, the results show 100% conversion of ethanol with a high selectivity to hydrogen. This was particularly evident when looking at another Ni/MgO-Al_2O_3 catalysts[197] which had the same components as the hydrotalcite catalyst produced during the project. While this catalyst had a 100% conversion of ethanol, its selectivity to hydrogen was lower and a greater amount of unwanted products were also produced.

Table 21. A table comparing the conversion (%) of ethanol and the selectivity (%) of different catalysts.

	X EtOH (%)	Selectivity (%)							
		H_2	CO	CO_2	CH_4	C_2H_4	C_3H_6	CH_3CHO	Me_2CO
WP1-D2	100	70	6	23	2	-	-	-	-
WP1-Ec	100	70	2	26	2	-	-	-	-
Co/MgO [196]	29	55	<1		2	2	4	28	-
Co/Al_2O_3 [196]	100	<1	-	<1	<1	99	-	-	-
Co/SiO_2 [196]	87	50	3	4	2	3	<1	38	-
Co/TiO_2 [196]	16	47	-	4	<1	13	-	34	-
Co/V_2O_5 [196]	100	54	-	16	1	20	<1	6	3
Co/ZnO [196]	100	71	-	20	<1	<1	<1	<1	7
Co/La_2O_3 [196]	85	63	-	22	1	1	<1	<1	12
Co/CeO_2 [196]	94	70	-	21	<1	2	<1	<1	6
Co/Sm_2O_3 [196]	86	65	-	21	2	7	<1	-	5
Ni/Al_2O_3 [197]	100	60	5	19	-	16	-	-	-
$Ni/MgO-Al_2O_3$ [197]	100	59	5	18	2	16	-	-	-
$Ni/ZrO-Al_2O_3$ [197]	100	55	1	22	-	22	-	-	-
$Ni/CeO-Al_2O_3$ [197]	100	57	3	21	2	18	-	-	-
$Ni/LaO-Al_2O_3$ [197]	95	58	3	22	4	13	-	-	-

Et = ethyl (CH_3CH_2), Me = methyl (CH_3), - = data that is not given

Conclusions

Structural information from X-ray diffraction clearly shows that a hydrotalcite structure is formed in the synthesis. It also shows that nickel is incorporated into the structure rather than form alternative products. This incorporated nickel caused a loss of definition in the diffraction pattern due to the large size of the atom distorting the lattice. ICP showed that the best M^{2+}/M^{3+} ratio is produced by the doped samples WP1-D1 and WP1-D2. This ratio is seen as favourable in the production

hydrotalcites. However hydrotalcites are made with other ratios, which are why the lower metal ratios of the samples that used washing at some stage of the synthesis still produce a hydrotalcite structure. The washing process is considered the reason for the loss of metal in the materials.

In Chapter 2 it was observed that unwashed materials produced in a continuous flow process result in a low surface area in the BET analysis while the washed samples exhibit larger areas. The trend continues with Ni modified samples. Doped samples, being unwashed, have the smaller surface areas presented by any of the samples. The samples that have the larger surface areas have been washed at some point in their synthesis, whether it was directly after synthesis as a washing stage or after drying during the nickel impregnation process. The exception to this is WP1-Ec. This is likely because of the calcination process experienced by the sample prior to the impregnation process. The calcination destroyed the lattice structure and rendered the hydrotalcite to its mixed oxide form. This mixed oxide is well known for being able to rehydrate back to the original structure.

Cryogenic nitrogen adsorption reveals Type IV isotherms for all the samples shows the presence of micropores. Since Type IV isotherms are observed for nonporous and mesoporous materials it can be assumed that those samples with larger surface areas have mesopores and micropores. The samples of smaller surface area have only micropores. These pore sizes also reflect the findings of Chapter 2. The smaller pore sizes belonging to the unwashed doped samples and larger pores to the samples that have experienced washing. It was discussed in Chapter 2 that the larger pores of repercussion of the washing process.

For most of the samples the thermal decomposition in the TGA shows standard three tiered cascade of hydrotalcite decomposition, except for the doped samples. The doped samples exhibit a fourth weight loss region. This fourth region is thought to be nickel oxide and aluminium oxide reacting to form a nickel aluminide alloy (Ni_3Al). Though this theory does explain the results obtain it is still only speculation and will require an *in situ* spectroscopy to confirm what is happening. Chapter 3 suggested that the product of continuous flow processes do not reduce to a spinel form as is reported about the batch produced counterparts. This was thought to be due to the formation of bicarbonate ions instead of carbonate ions. WP1-Ec, once calcined and reformed in the nickel impregnation, is a material produced by thermodynamic control. When reduced a peak at high temperature is evident of the spinels structures. WP1-D2 is a material produced by kinetic control and the reduction shows no spinel presence. The formation of nickel aluminide would not be seen in the reduction as the metal alloy is already in a reduced state.

There is another source of evidence of the increased metallic nature of WP1-D2. At the temperature of fourth weight loss region witnessed in the TGA WP1-D2 produces considerable amounts of ethane. The cleaving of a carbon-carbon bond is done with a metallic catalyst. Overall the WP1-D2 was catalytically more active than WP1-Ec. This is likely because the spinel were inactive due to not being fully reduced.

The performance of the catalyst showed a greater selectivity for hydrogen than other catalyst in literature. It also demonstrated the unique properties of the calcined mixed oxide, as a catalyst with similar components demonstrated a lower performance than the hydrotalcite.

This area of the project is still ongoing through the BioGo project. The catalytic activity of the other samples is still required; with priority given to WP1-IE as it has similar nickel content to WP1-Ec. Spectroscopy of the doped samples would be required to establish what happens to the samples during the fourth weight loss region.

Chapter 5 - Zirconium Basic Sulfates

Literature Review

In previous chapters it has been discussed that the hydrotalcite made in a continuous flow process was subject to a kinetic control rather than the thermodynamic control seen in the batch process. The properties of the material prepared under kinetic control could be changed to resemble those of a thermodynamic control material through washing, but not to the same extent that it would have it was simply made in batch. Due to hydrotalcite becoming solid as soon as it was formed it was not possible to explore whether the kinetic material could be aged to a thermodynamic material in flow. This project was part funded by MEL Chemicals who were interested in investigating the possibility of producing zirconium basic sulfate in a continuous flow process. In their batch process they were able to be able to produce a 5 and 1 μm particles by altering the concentration of the starting reagents. While MEL Chemicals were unable to discuss the exact method of their batch process they were interested if particle size could be controlled in a continuous flow process. With this particle growth being a result of thermodynamic process and the particles in question being practical to work with, it gave a scenario to investigate.

Particle size increases due to a material preference to be at a lower energy state. Larger particles with lower chemical potential will grow as smaller particles with higher chemical potentials dissolve. The driving force behind this is the reduction of the total surface energy of the system.[198] Chemical potential is dependent on a number of factors: concentration, temperature and pressure. Pressure does not play a role in the particle size in the batch synthesis of hydrotalcites as it is kept constant. In a batch reactor, the heating process is dependent on surface area of the heated

surface, not volume of the reactor. While both the volume and the surface area are increased during the scaling up, the scale is usually related to a linear dimension. Because volume increases to the power of three and the surface area by the power of two, a difference is produced in the scaling up that leads to uneven heating, creating hot spots with in the mixture.[15] As temperature increases the chemical potential drops, therefore within these hot spots are particles which have a lower chemical potential than those particles in the lower temperature areas of the reactor. In a co-precipitation batch reaction the reactant are added slowly into the batch reactor slowly building up the concentration of the product. The chemical potential of the particles increases as the concentration increases and this encourages the dissolution of the particles at a higher chemical potential. This allows for the re-precipitation of materials on particles of lower chemical potential allowing the particle to grow. This in turn lowers the chemical potential further and with it the surface energy. This is further encouraged by the mixing of larger batch reactors. As the size of the batch increases, the mixing efficiency decreases, thus creating concentration gradients.

A basic zirconium sulfate is categorised as a complex containing zirconium and sulfate ions in a ratio greater than 1:2. [199-201] The zirconium in this compound is in the +4 oxidation state, making it coordinate in an eight pointed polyhedron in the form of a dodecahedron. [202] The central atom of the dodecahedron is a zirconium atom bound to eight coordinating oxygen atoms. In zirconium basic sulfate, four of these coordination points belong to the sulfate ions acting as sulfate bridges.[201]

Zirconium basic sulfate is used as a precursor to producing zirconia. Zirconia is produced from zirconium oxychloride solution in hydrochloric acid that is caused to precipitate with ammonia. [202] Yet to obtain a substantially pure zirconium-bearing

species from an impure oxychloride solution, basic sulfate solutions are used as a precursor. [202]

When zirconium basic sulfate is added to cetyltrimethylammonium bromide (CTMA-Br) it forms hexagonal phase zirconium oxide [203]. This can be further stabilised by H_3PO_4 acidic treatment. These materials have shown some properties that closely mimic those of MCM-41.[204]

The synthesis of the zirconium basic sulfates is achieved by the continuous addition of zirconium oxychloride to sulfuric acid.[201, 205, 206] This method is used as it forms a precipitate in a good yield. [206] The Zr^{4+}/SO_4^{2-} ratio is given to be between 5:2 and 5:3.[202, 207] At this range and higher the amount of Zr^{4+} ions lost in the filtrate is 0.05%. At lower ratios than this, the percentage of lost Zr^{4+}rises.[202] The synthesis is usually done at elevated temperature.[201, 205] The product may also require ageing in a heated environment as it is reported that at temperatures above 70 °C the product will spontaneously precipitate.[206, 208]

Experimental

Methods of Preparation

Zirconium oxychloride was pumped together with sulfuric acid under flow conditions at a ratio of 5:3. The system comprised of a peristaltic pump (Ismatec ISM597D) fitted with 3-stop 0.51 mm ID PVC tubes and a Y-mixer (PEEK 0.5 mm). The reactor was a PVC tube with 1 mm ID and 2 m in length (Figure 79). The maximum flow rate was found to 0.2 ml min^{-1}; any faster was not enough time for precipitation to occur.

The samples in series 1 were prepared in the manner described above. The reactor for this series of samples was kept in a single length and the temperature was held constant at 80 °C for all samples as this was a common temperature in literature. Concentration of zirconium oxychloride was varied at 100%, 50% and 25 %.

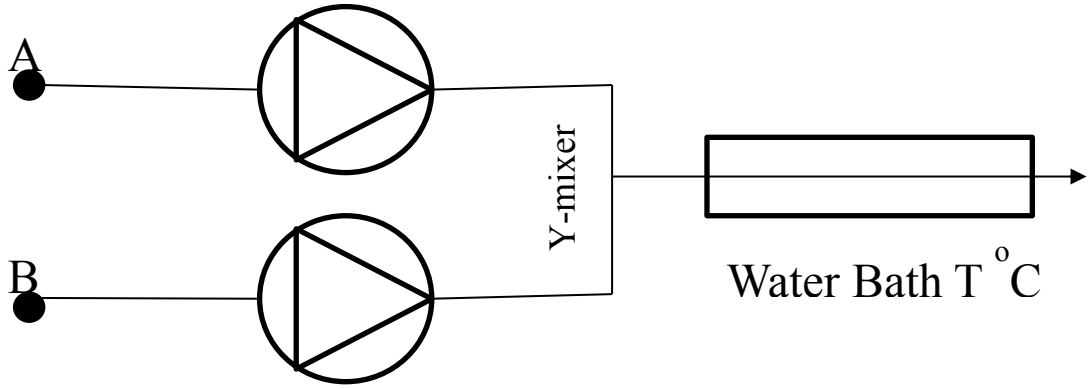

Figure 78. An illustration of the equipment set up used for series one.

Table 22. Table of conditions used for series one

Concentration	**Zr^{4+}:SO_4^{2-} Ratio**	**Temperature °C**
100 %	5:3	80
50 %		
25 %		

In series two the samples were made in the manner described above with the reactor being kept as a single length like the series one samples (Figure 79). The temperature was altered between 40 and 90 °C for each sample but the temperature decided upon was kept constant throughout the reaction.

Table 23. Table of conditions used for series two.

Temperature	Concentration	Zr^{4+}:SO_4^{2-} Ratio
40 °C	100 %	5:3
50 °C		
60 °C		
70 °C		
80 °C		
90 °C		

From the previous samples it was found that 80 °C was the best for precipitation. The experiment of series two was repeated, this time with the reactor split into two lengths of 1 m and the latter length being kept constant at 80 °C (Figure 81). This was done to try and create a small number of seeds at one temperature. Those seed would drop in chemical potential at the higher temperature facilitating their growth by adsorbing the unreacted zirconium still in solution.

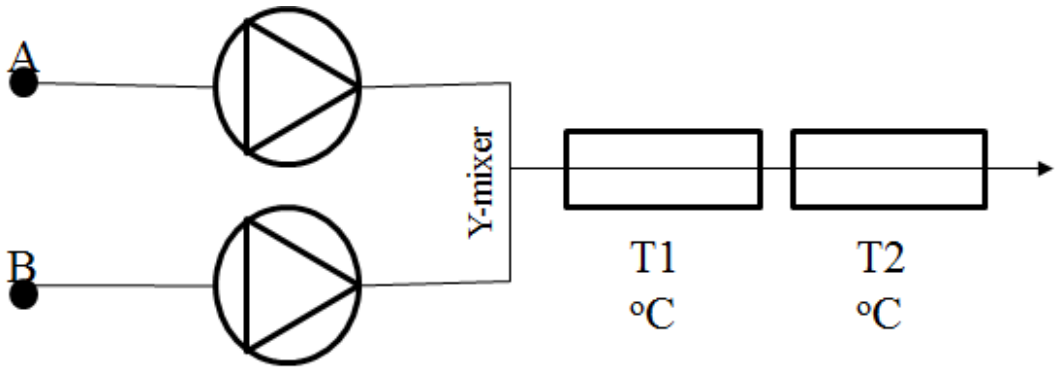

Figure 79. An illustration of the equipment set up used for series three.

Table 24. Table of conditions used for series three

Temperature	**Concentration**	**Zr^{4+}:SO_4^{2-} Ratio**
40/80 °C	100 %	5:3
50/80 °C		
60/80 °C		
70/80 °C		
80/80 °C		
90/80 °C		

In series four of experiments the temperature was kept the same for both temperatures. T1 was 90 °C and T2 was 80 °C. This time the number of moles of Zr was added in two stages. The idea being that the smaller amount will form nuclei in the first stage and the remaining amount will precipitate around the seeds that have already formed. The smaller amount added to the sulfuric acid and heated to 90 °C while the remaining amount was added by a second pump (beaker C) and added to the rest of the reaction just before the change in temperature through a Y-mixer (PEEK 0.5 mm). The Zr from beaker C was heated to 80 °C before joining the main reaction.

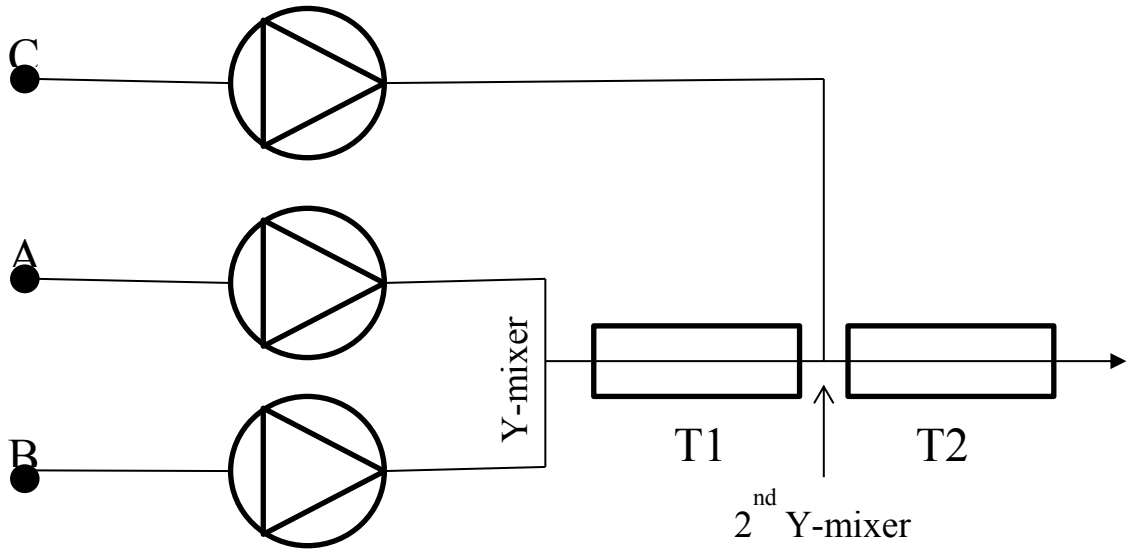

Figure 80. An illustration of the equipment set up used for series four.

Table 25. Table of conditions used series four.

Percentage of Zr in Jar 1	**Percentage of Zr in Jar 2**	**Concentration**	**Zr^{4+}:SO_4^{2-} Ratio**	**Temperature °C**
10	90	100 %	5:3	90/80
20	80			
30	70			
40	60			
50	50			

Procedures of analysis

The yield of precipitation was determined by EDTA titration using xylenol orange. Once the precipitate was separated, the remaining liquor was used for titration. Xylenol orange indicator (pH range 3.2 – 4.4) was added to the liquor and titrated against 0.1 M EDTA solution until the pink solution turned yellow. The number of moles of zirconium detected in the titration was subtracted from number of moles added at the beginning of the experiment. [199]

Infra-red spectroscopy was used qualitatively in order to be certain of the production of the basic sulfate. A Bruker Alpha FT-IR Spectrometer (Platinum ATR) was used with the ZBS wet cake placed directly on the sampling area.

Microscopy was done on a Polyvar microscope at x50 magnification and pictures taken on an Olympus digital camera. The samples were prepared by adding 0.01 g of wet sample to 5 ml of water. Sonification and stirring were used to separate and disperse the particles. The solution was applied to a slide and left for 12 hrs at ambient temperature to allow the water to evaporate. This method was employed as it gave the best separation of the particles. Other methods were attempted but resulted in the particles agglomerating during the drying process.

Results and Discussion

EDTA Titration

All three samples in series one were produced at respectable yields. The actual masses of ZBS could not be exactly calculated due being unable to dry the product

completely. The drying process causes particle to agglomerate and obscure the result of the particle size.

Table 26. Yields of ZBS as found in the titration of series one.

Concentration	**Yield (%)**
100 %	89.2
50 %	87.9
25 %	88.8

For series two yields at 40 and 50 °C produced very small quantities of ZBS as the temperature was too low for precipitation. 60 and 70 °C produced better yields but were far from acceptable. The only respectable yields came from the higher temperatures of 80 and 90 °C.

Table 27. Yields of ZBS as found in the titration of series two.

Temperature	**Yield (%)**
40 °C	7.8
50 °C	2.3
60 °C	16.6
70 °C	25.3
80 °C	89.3
90 °C	88.3

All samples in series three produced respectable yields as the final length of the reactor was above the precipitation temperature. A trend can be seen in the yields, with the samples made with a lower starting temperature producing a higher yield.

Table 28. Yields of ZBS as found in the titration of series three.

Temperature	**Yield (%)**
40/80 °C	89.4
50/80 °C	89.1
60/80 °C	88.6
70/80 °C	88.8
80/80 °C	87.4
90/80 °C	88.4

As all the samples in series four were produced at temperatures above the temperature required for precipitation the yields were all of acceptable values.

Table 29. Yields of ZBS as found in the titration of series four.

Percentage of Zr in Jar 1	**Percentage of Zr in Jar 2**	**Yield (%)**
10	90	89.2
20	80	89.8
30	70	89.6
40	60	88.4
50	50	88.8

Infrared Spectroscopy

The spectra produced by series one showed peaks at 1211, 1099 and 1010 cm^{-1} that were the adsorption band assigned to bidentate sulfate ions co-ordinating to Zr^{+4}.[209, 210] The peaks at 3217 and 1631 cm^{-1} were peaks associated with hydroxide ions.[209, 211] The greater intensity of the sulfate bands showed the sulfate bridges mentioned in the literature.[201]

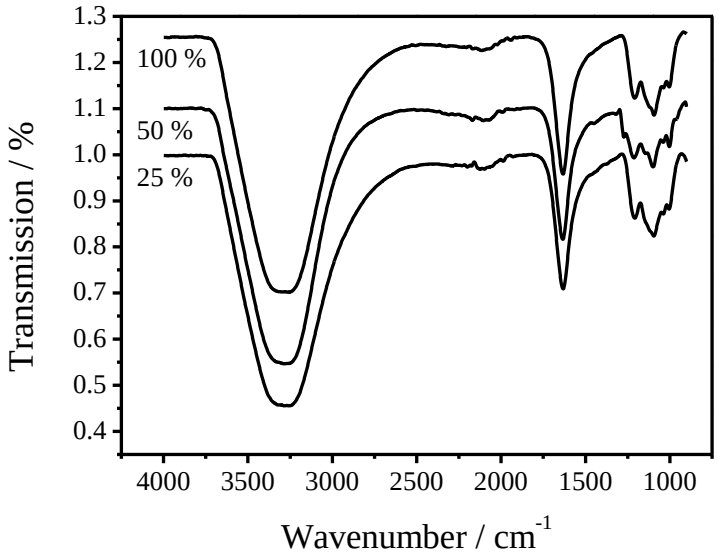

Figure 81. Infra-red spectra of series one ZBS produced at different concentrations.

Spectroscopy of series two showed some weakening of the sulfate band at 1010 cm^{-1} in the samples made at 60 and 70 °C. Due to the temperature not being sufficient for full precipitation it was likely these materials were not as stable as those at 80 and 90 °C.

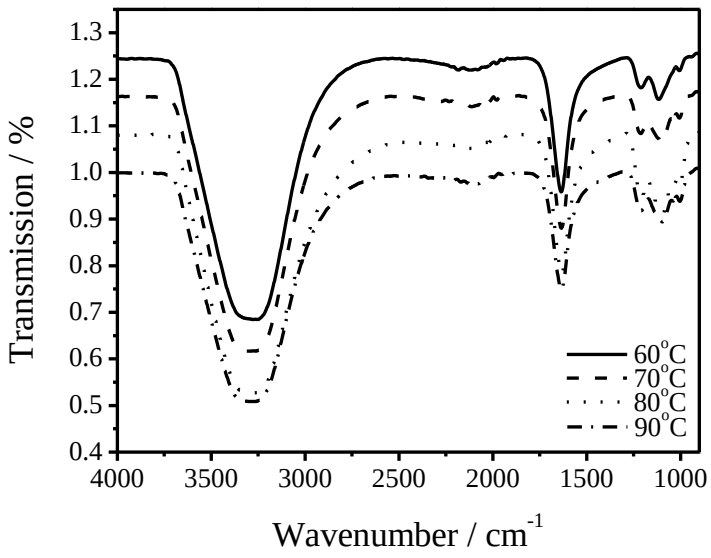

Figure 82. Infra-red spectra of series two ZBS produced at different temperatures.

All samples in series three produced the expected spectrum with all the bands in the expected places.

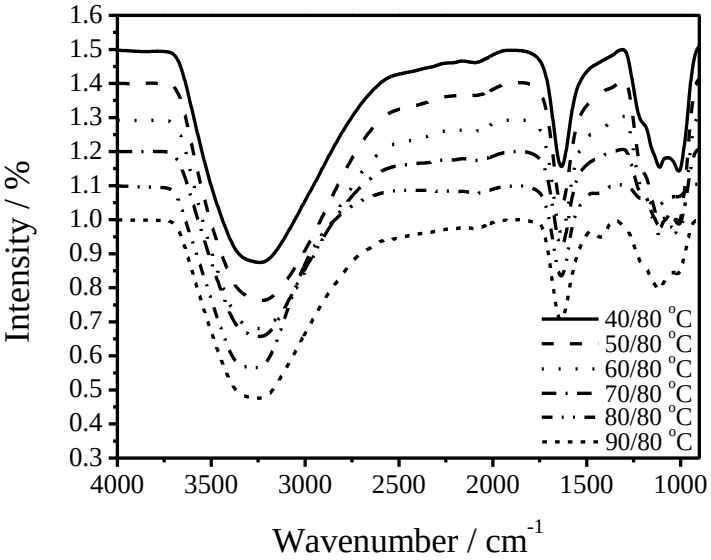

Figure 83. Infra-red spectra of series three ZBS produced using dual temperature control.

As with the yields, the series four samples produced spectrum that displayed all the required bands at the necessary wavelengths.

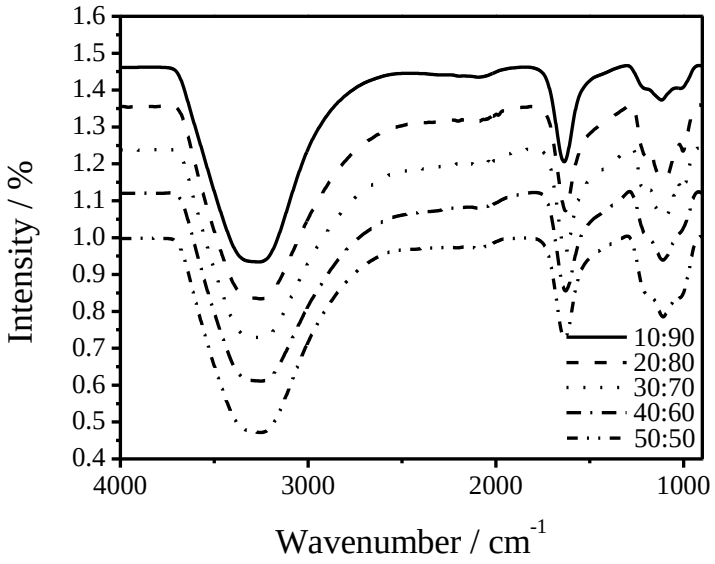

Figure 84. Infra-red spectra of series four ZBS produced at different varied concentration.

Microscopy

While images from all the samples were taken, all except the image below (see Figure 85) are to be found in the Appendix. Using the ImageJ software, measurements of the particle dimensions were taken and put into a histogram as seen below. From these measurements it can be seen that the produced samples had a range of particle sizes, though the largest distribution of particles were below 1 μm and the majority of particles were below 2 μm. With such a preference for the smaller particles, the particle measurements of 4 and 5 μm were more likely agglomerates of these smaller particles than larger particles.

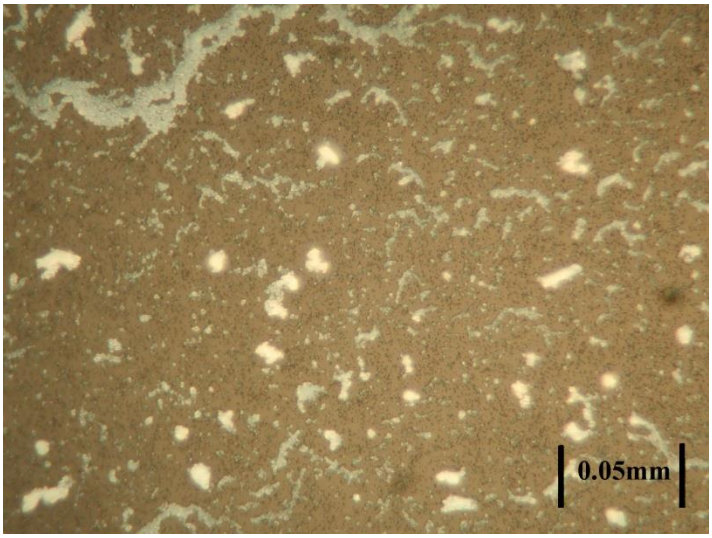

Figure 85. Image from the microscopy of series one 100 %

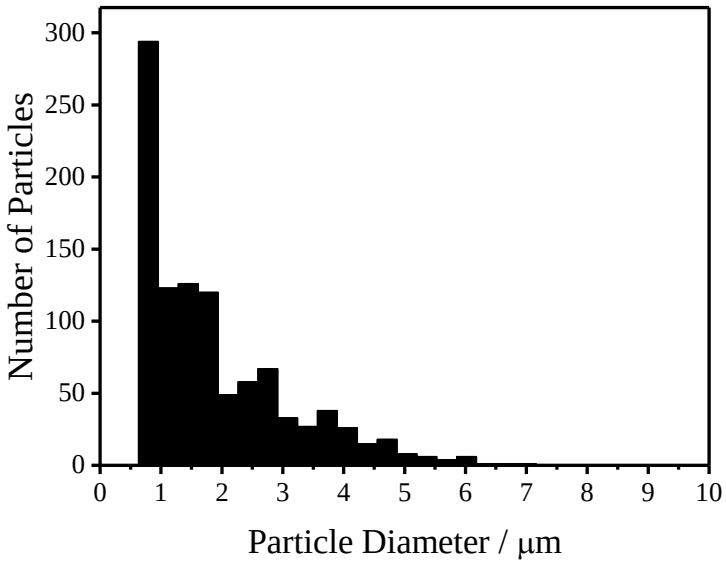

Figure 86. Histogram illustrating particle size distribution of series one ZBS produced with 100 % concentration of zirconium oxychloride.

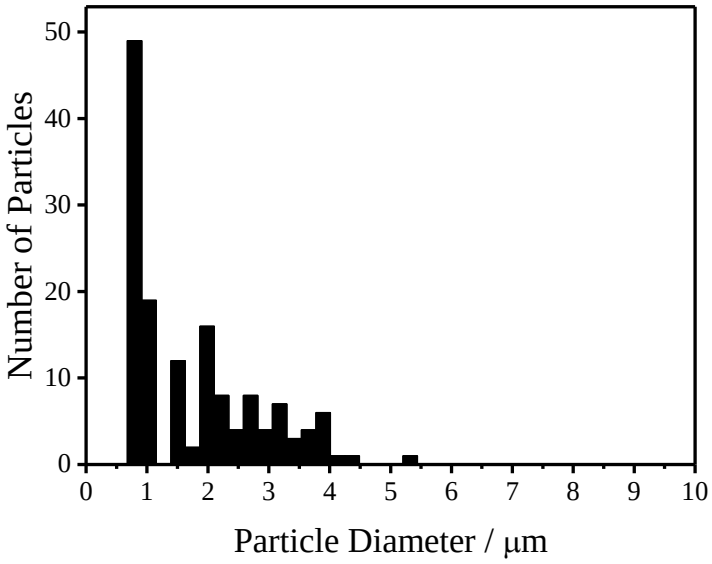

Figure 87. Histogram illustrating particle size distribution of series one ZBS produced with 50 % concentration of zirconium oxychloride.

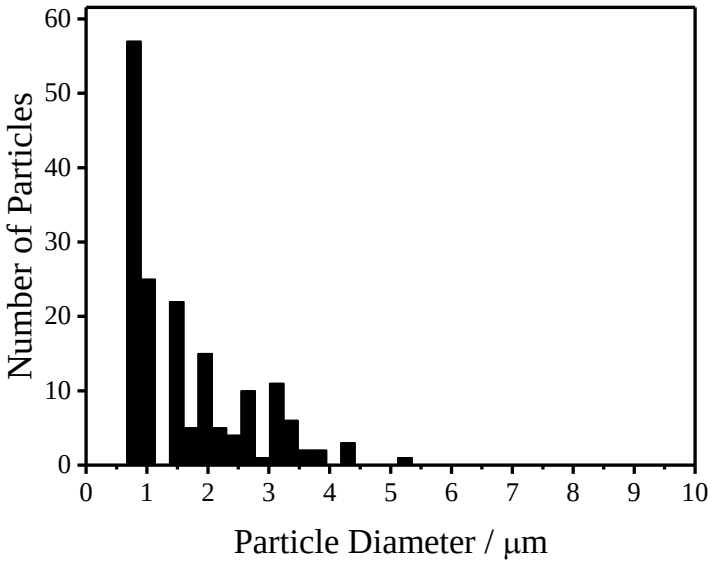

Figure 88. Histogram illustrating particle size distribution of series one ZBS produced with 25 % concentration of zirconium oxychloride.

The series two histograms of the particle size distribution showed the same preference to the smaller particles as the histograms showed in the series one samples. Samples made at 80 and 90 °C displayed a higher number of larger particles but these were likely agglomeration of the smaller particles that the ImageJ software could not separate.

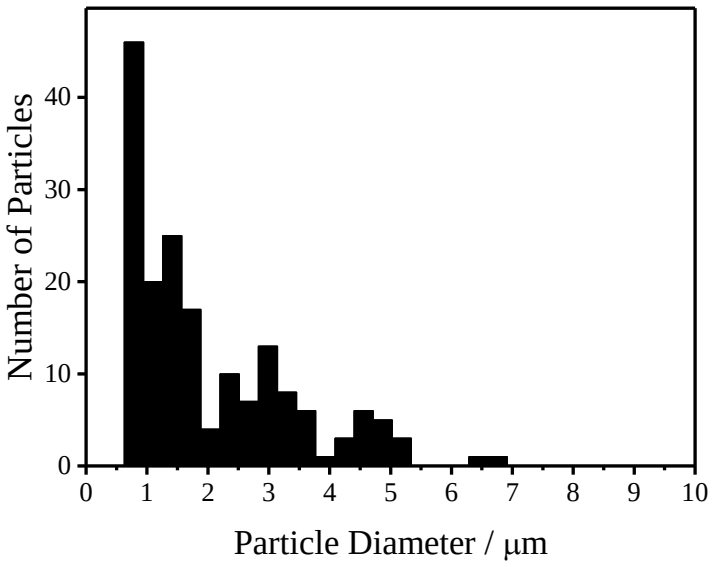

Figure 89. Histogram illustrating particle size distribution of series two ZBS produced at 60 °C.

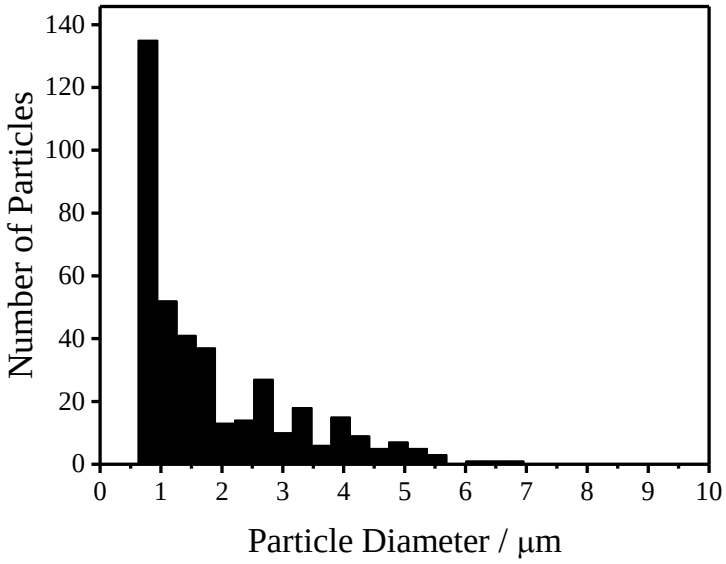

Figure 90. Histogram illustrating particle size distribution of series two ZBS produced at 70 °C

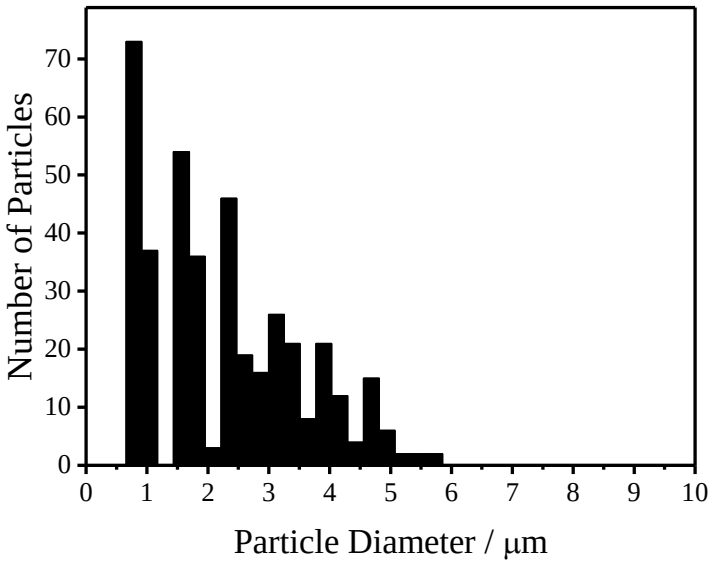

Figure 91. Histogram illustrating particle size distribution of series two ZBS produced at 80 °C

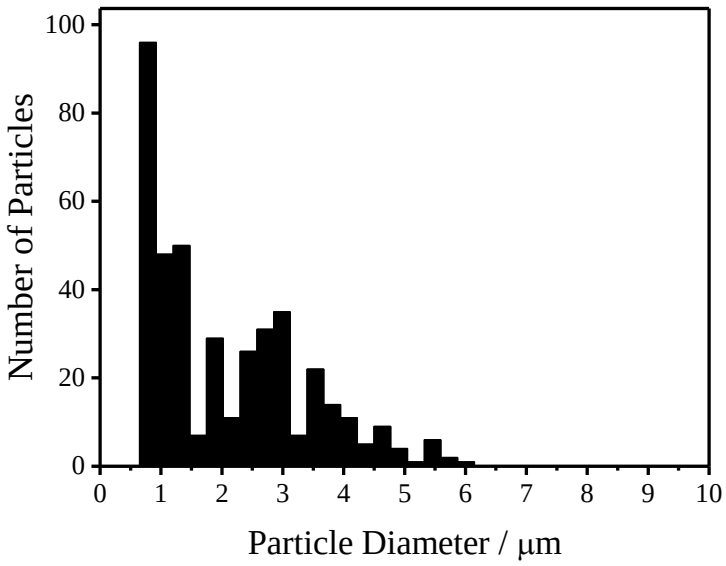

Figure 92. Histogram illustrating particle size distribution of series two ZBS produced at 90 °C

As seen before the dual temperature process of series three produces smaller particles and agglomerations at larger sizes.

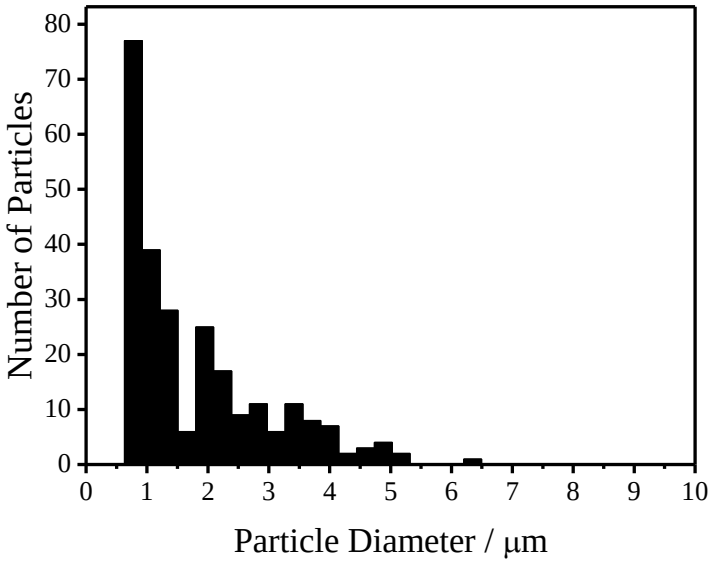

Figure 93. Histogram illustrating particle size distribution of series three ZBS produced at 40/80 °C

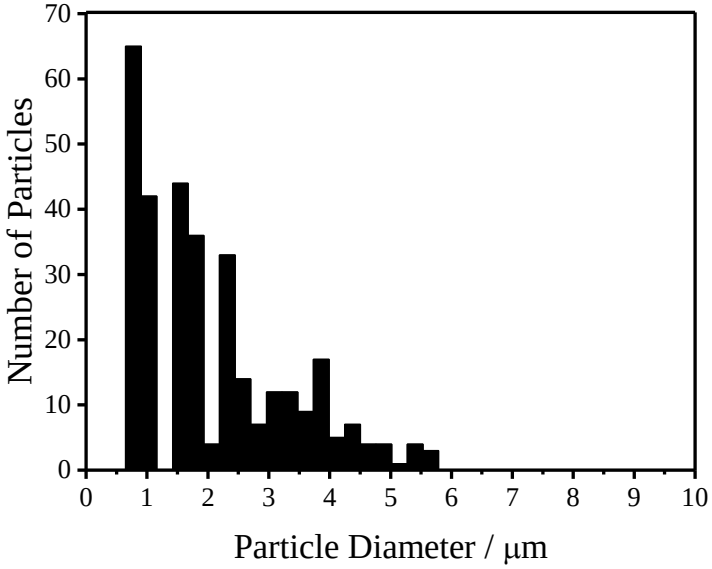

Figure 94. Histogram illustrating particle size distribution of series three ZBS produced at 50/80 °C

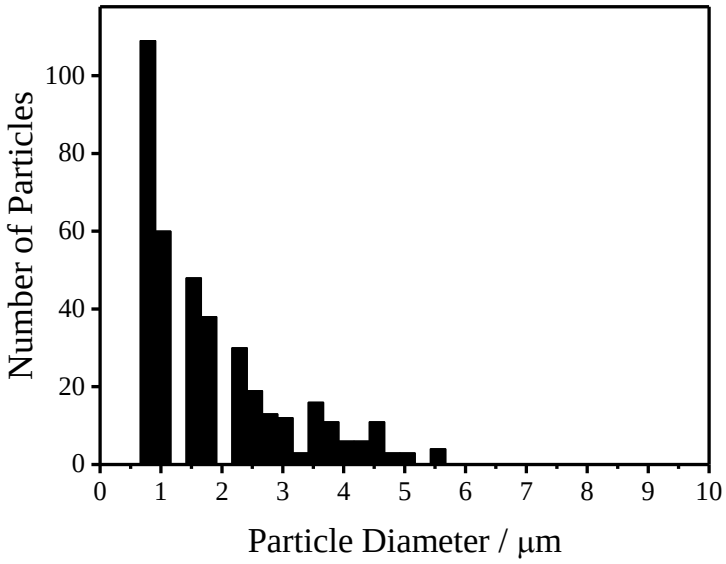

Figure 95. Histogram illustrating particle size distribution of series three ZBS produced at 60/80 °C

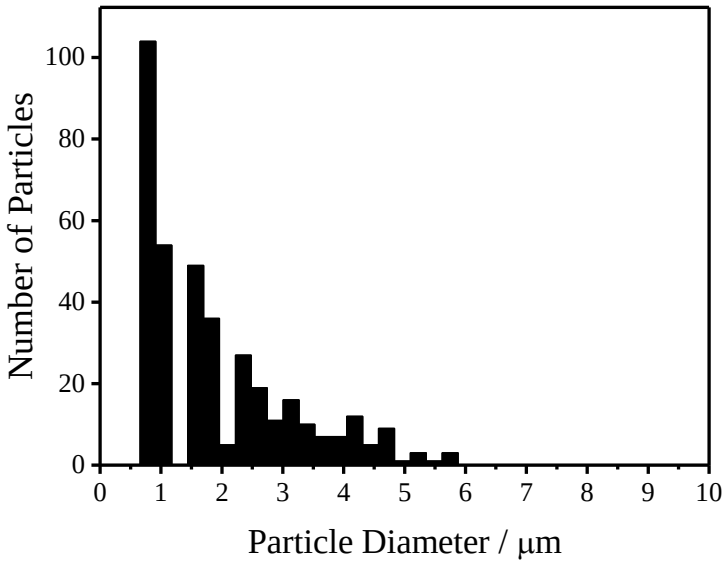

Figure 96. Histogram illustrating particle size distribution of series three ZBS produced at 70/80 °C

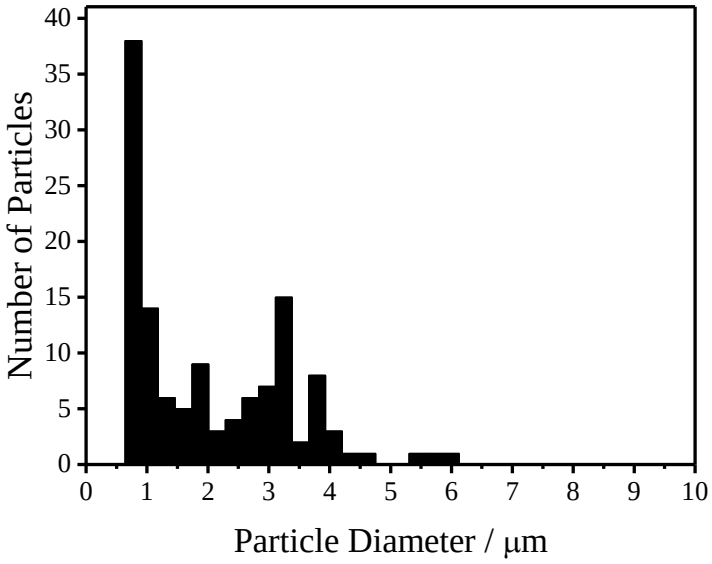

Figure 97. Histogram illustrating particle size distribution of series three ZBS produced at 80/80 °C

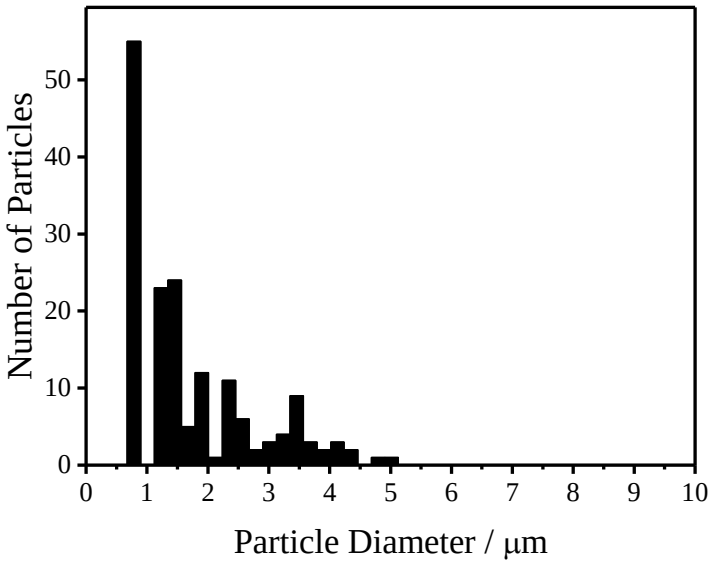

Figure 98. Histogram illustrating particle size distribution of series three ZBS produced at 90/80 °C

The histograms of series four showed, once again, a preference for smaller particles with no indication of any increase in overall particle size.

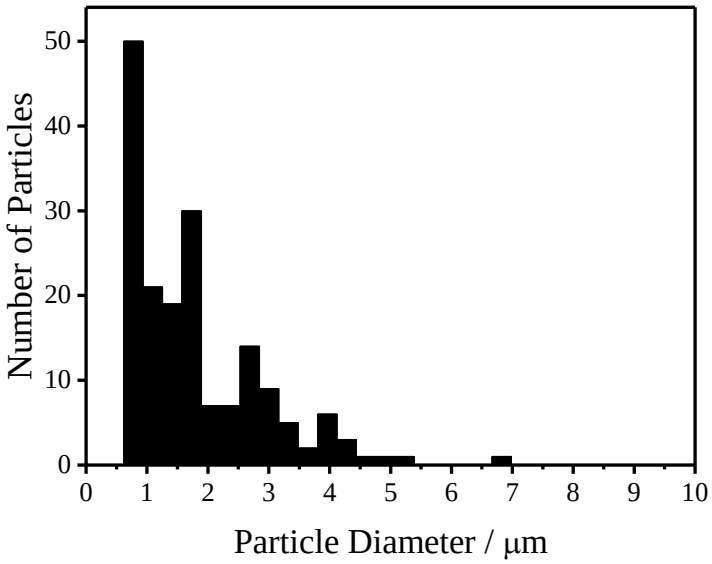

Figure 99. Histogram illustrating particle size distribution of series four ZBS produced with 10:90 molar ratio split.

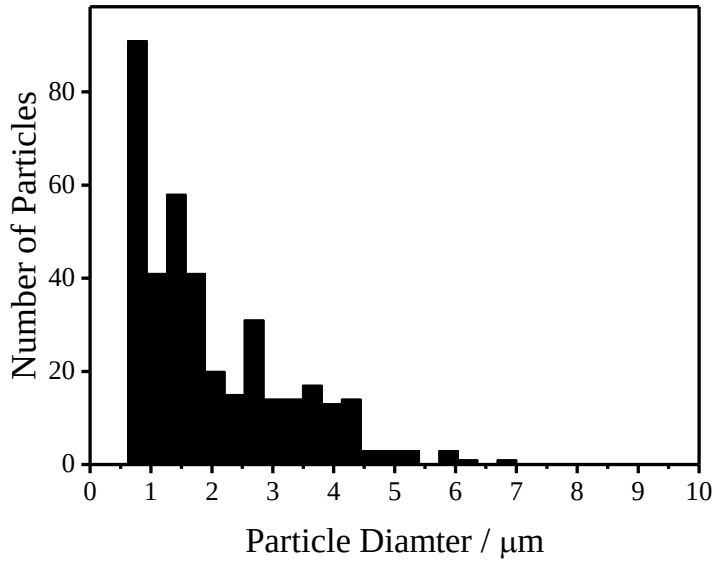

Figure 100. Histogram illustrating particle size distribution of series four ZBS produced with 20:80 molar ratio split.

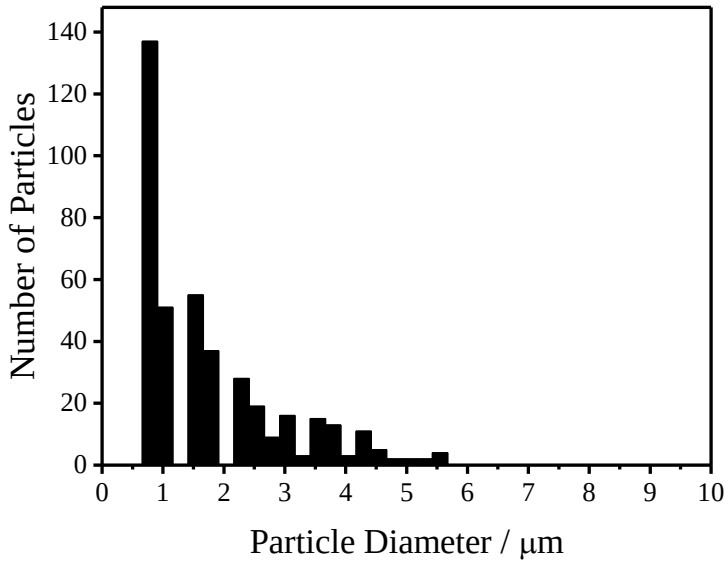

Figure 101. Histogram illustrating particle size distribution of series four ZBS produced with 30:70 molar ratio split.

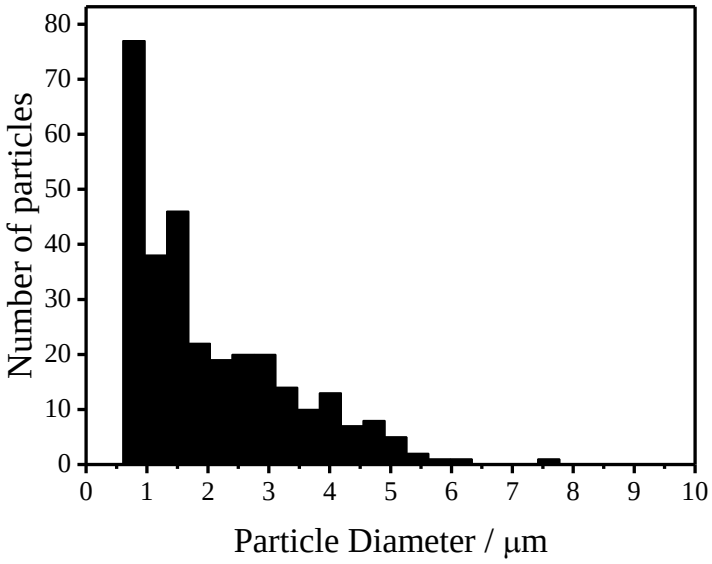

Figure 102. Histogram illustrating particle size distribution of series four ZBS produced with 40:60 molar ratio split.

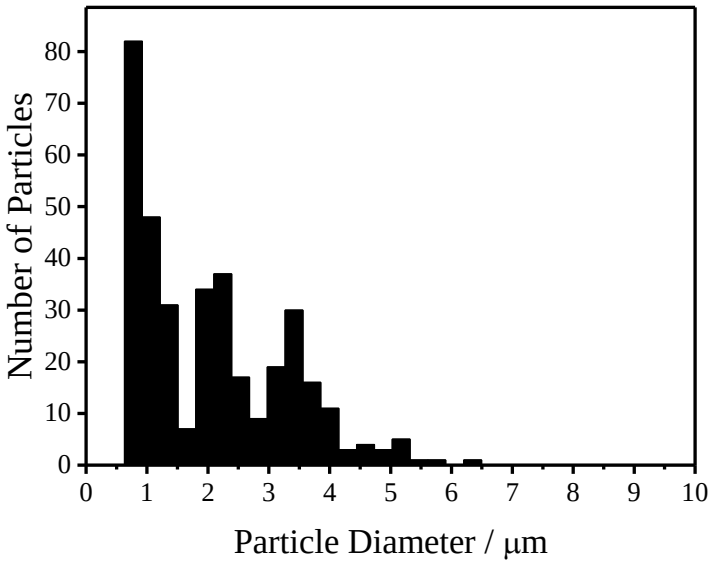

Figure 103. Histogram illustrating particle size distribution of series four ZBS produced with 50:50 molar ratio split.

Conclusions

The concentration variations of series one in the starting reagents do not the affect the size of the particles in the continuous flow process as they do in the batch. Unlike the batch process the concentration of the reagents does not affect the concentration in the reactor. The concentration along the reactor is constant as is the temperature control. This means all the particles that are formed have the same chemical potential. Therefore, all particles are dissolving and precipitating at the same rate, preventing any particles from growing. Because of this it was decided to keep the concentration of zirconium oxychloride at 100 % for all the following samples.

While an increase in temperature in series two does decrease the chemical potential of a particle, it is the temperature variations in the batch process that would result in the increase in particle size. The temperature in the continuous flow process is constant throughout the reactor. With the constant temperature and concentration the particles are of similar potentials, resulting in no particle growth. Due to the sample made at 80 °C giving the better yield and spectrum it was decided to remain with the literature temperature through the following samples.

The method of series three failed due to it not having a temperature gradient. The temperature changed but due to the controlled environment of the continuous flow process the chemical potentials changed for all the material at each temperature in a uniformed manner nullifying at potential gradient.

The process method of series four also failed due to the controlled environment of the continuous flow process. Through the concentration and the temperature did change it changed in a uniformed manner along the latter length of the reactor. This prevents any gradient in the reactor.

This study has shown that the production of zirconium basic sulfate is possible in a continuous flow process. It also demonstrates that a continuous flow process will only produce the kinetic product rather than allow a thermodynamically stable product to be reached. In this particular case, the particle size cannot be increased.

The particle size can be altered in the batch process due the variable environment within the reactor. Inefficient mixing creates concentration gradients where material in the lower concentration regions will be of a lower chemical potential, encouraging the dissolution of the particles of higher potential in the higher concentration regions. This is further encouraged by inefficient heating creating a temperature gradient affecting the chemical potentials of the materials in a similar manner as the concentration. It is the gradients within the batch reactor that allow for the thermodynamic product to be produced and the particle size to increase.

In a continuous flow reactor these gradients do not exist. The advantage of the flow reactor is the ability to control the environment of the reactor. The uniformity of the reactor environment eliminates any temperature or concentration gradients, keeping all the materials at similar chemical potentials limiting particle growth.

While a temperature gradient would not be possible to achieve within the continuous flow reactor, it may be possible to create a concentration gradient. Using a syringe pump (see Figure 104 below), or a pump of similar design, it would be possible to pump a solution of one concentration for a period of time before pumping a solution of different concentration in to the reactor. This would possibly create a concentration gradient within the reactor. This would need looking into in further study.

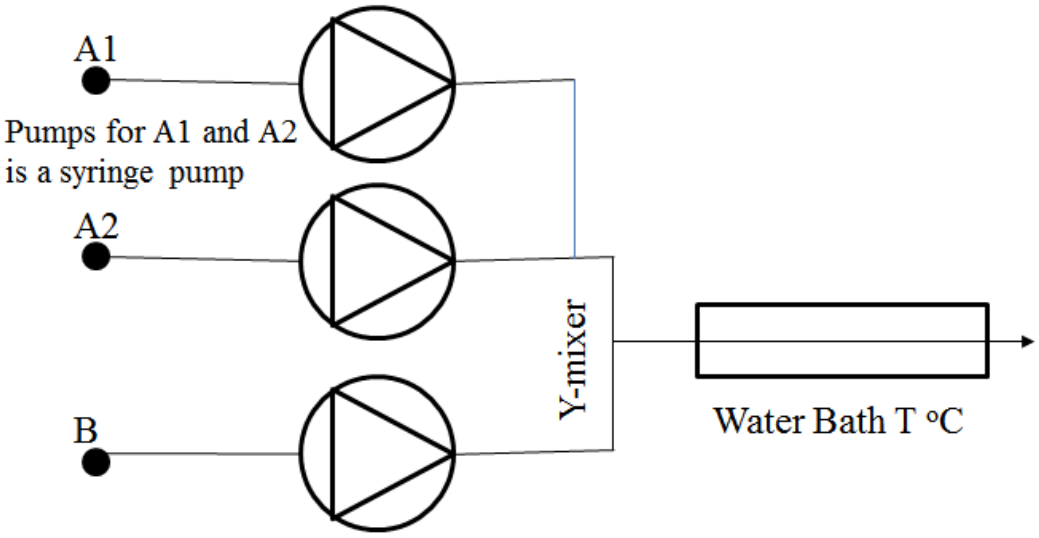

Figure 104. Proposed set up of equipment that could produce a concentration gradient within the reactor.

Chapter 6 – Final Conclusions

The aim of the project was to produce hydrotalcite and zirconium basic sulphate in a continuous flow process. Both of these materials are traditionally made in a batch process, but the project showed that both of these materials could also be made in a continuous flow process. The continuous flow process allowed for greater control of the reaction conditions as expected and it was found that these conditions gave rise to a kinetically controlled reaction as opposed to the thermodynamically controlled reactions in the batch process.

The often cited problems of the batch process are the ineffective mixing and heating of the batch reactor. The continuous flow process removed these problems, however it was found that material synthesis could benefit for these problems. The temperature and concentration gradients found in a batch reactor provides the material the environment needed for both precipitation and dissolution. It is a combination of these two actions that allow the material to achieve the lowest energy configurations. The continuous flow reactor provides stable conditions throughout the duration of the reaction. This prevented achievement of the lowest energy configuration and instead produced to the quickest configuration possible.

For hydrotalcite, this affected the structure of the lattice, which in turn effected the chemical composition of material as a whole. The thermodynamically controlled batch material was able a configuration where aluminium ions in opposing lattices were adjacent to each other. This allowed for the charge imbalance of the lattices to be balanced by a carbonate anion acting as a bridge between the two layers. The kinetically controlled continuous flow process did not allow for this arrangement to be achieved which resulted in aluminium ions being out of phase with each other.

This in turn resulted in the carbonate anions becoming bicarbonate anions and balancing the charge at only one aluminium ion. The remaining aluminium ions had their charges balanced by nitrate anions that were present from the starting reagents. This structural alteration did not produce any significant effect on the performance of the material. It could be argued that this is due to the reaction preformed with the hydrotalcite required the calcined products of hydrotalcite. During calcination the structure collapses to form a mixed oxide. It would be of interest for future examination the activity of uncalcined material.

During a batch process, the temperature and concentration gradients in the reactor allowed zirconium basic sulphate particle to grow. This was due to the effect these gradients have on the chemical potentials of the partials, with the particles at higher chemical potential dissolving and the particles at lower chemical potential growing. In the continuous flow process these gradients were not present and all the particles were at the same chemical potential. This meant that the particle could not grow beyond the initial seeding stage of precipitation.

Going forward, it would be of interest to examine whether continuous flow processes produce exclusively kinetic reactions or whether a set of conditions exist that would allow for thermodynamic control. This could be done by rapid change in concentration of the starting reagents, creating localised concentration gradients in the reactor. In general this project has provided an understanding of how synthesis of solid material is affected in a continuous flow process.

Appendix

The additional micrographs of the zirconium basic sulfate samples used in Chapter 5.

Series 1

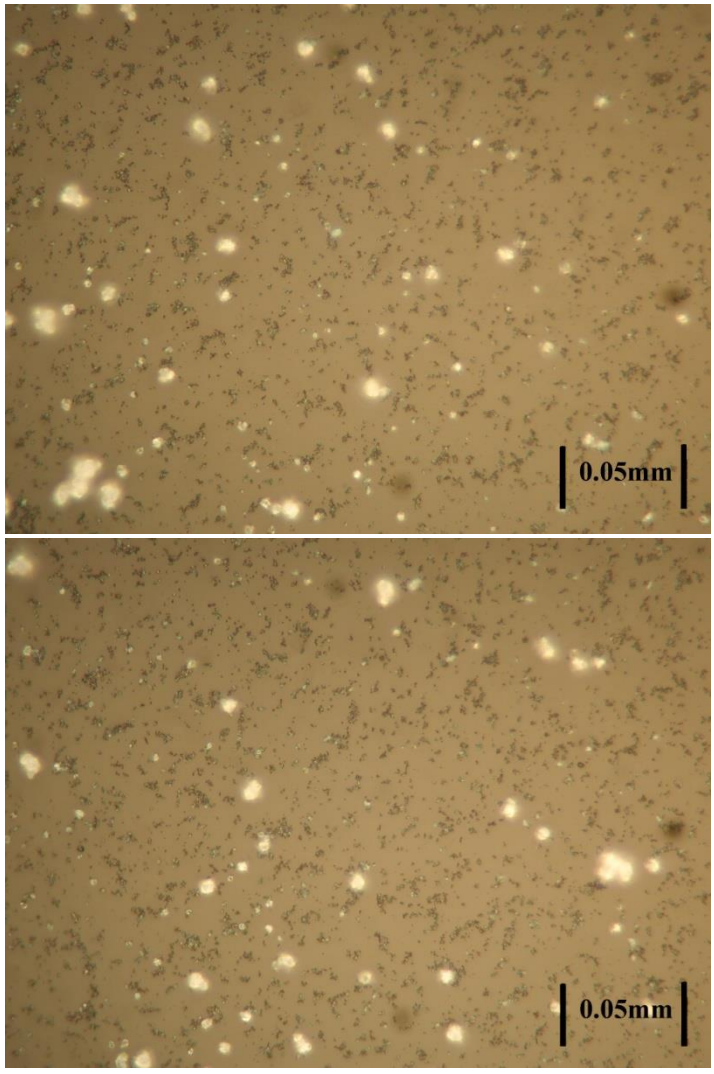

Figure 105. Series one micrographs a) 50 % b) 25 %

Series 2

a)

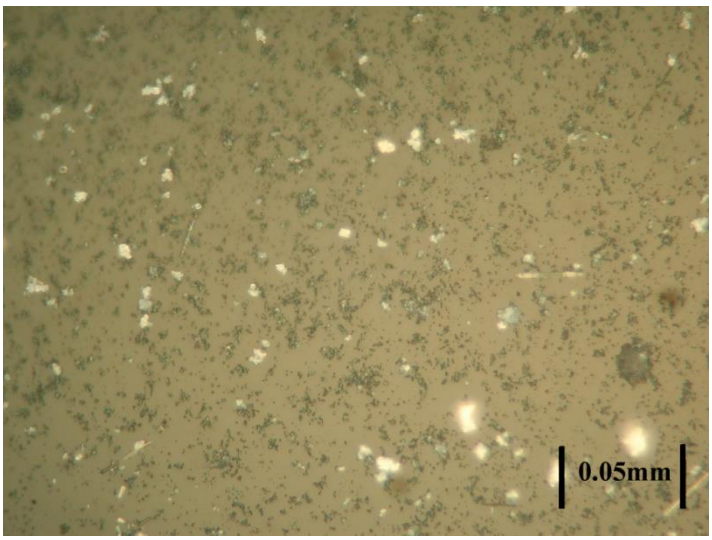

b)

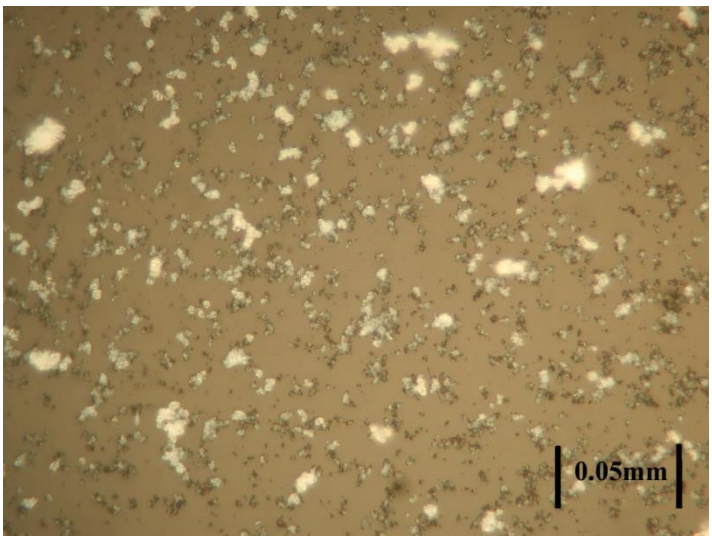

c)

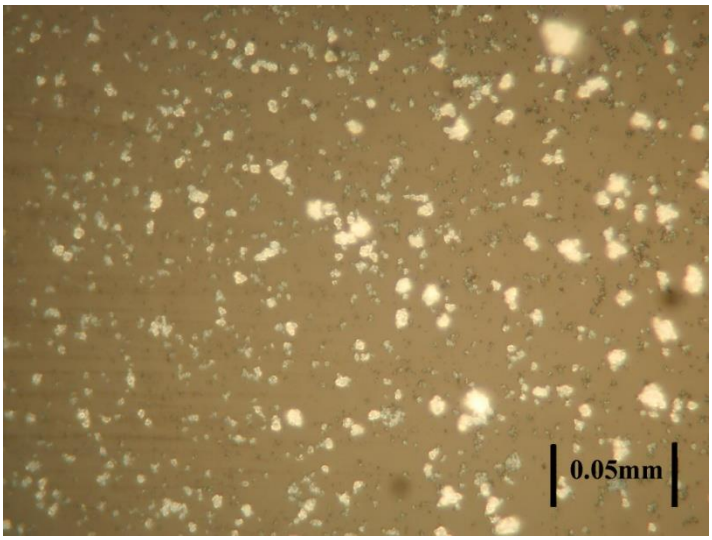

d) 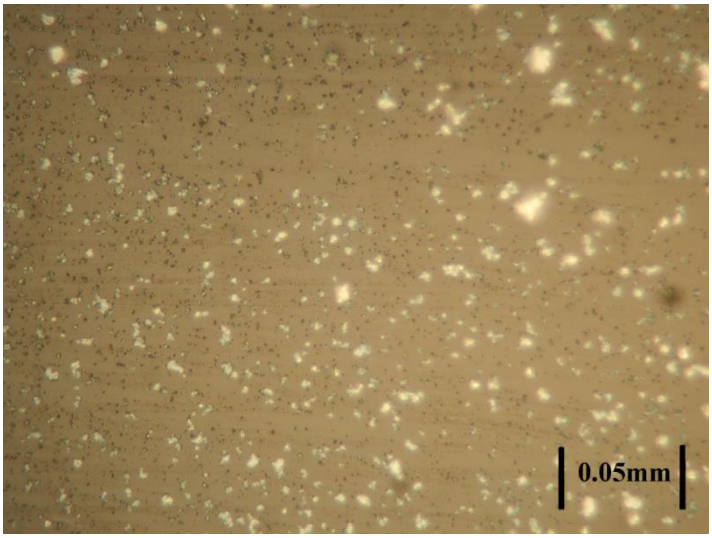

Figure 106. Series two micrographs a) 60 °C b) 70 °C c) 80 °C d) 90 °C

Series 3

a) 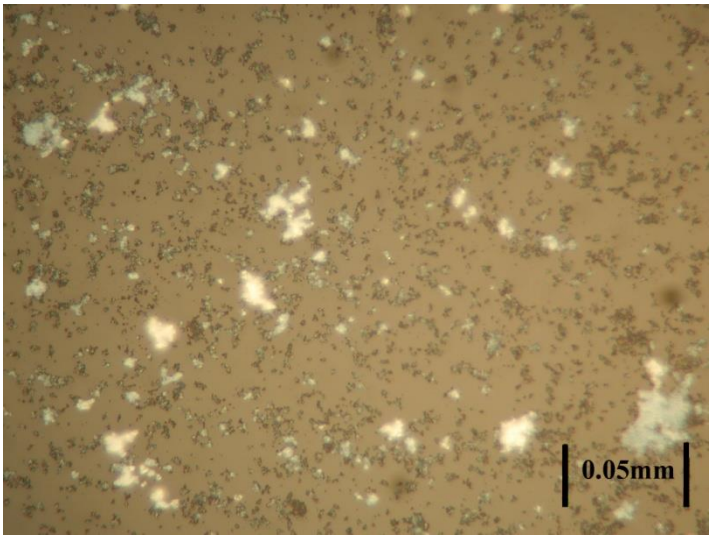

b)

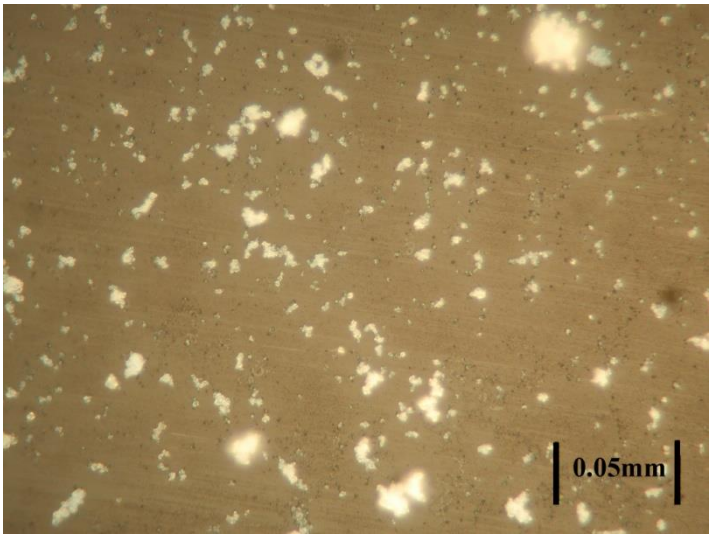

c)

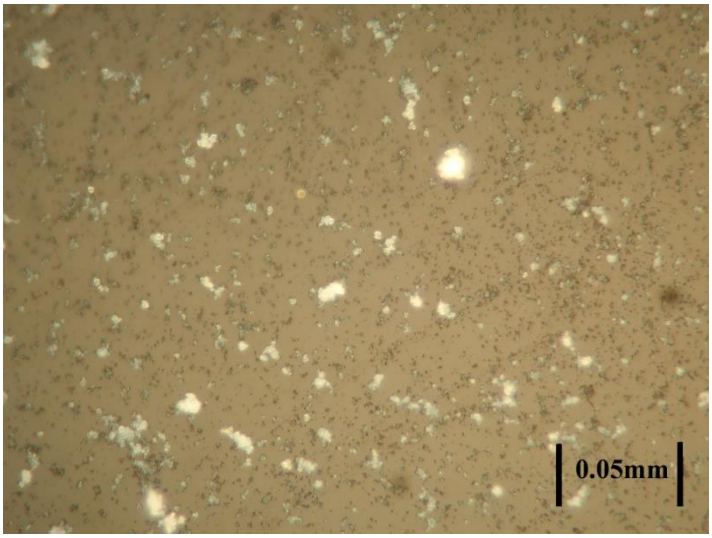

d)

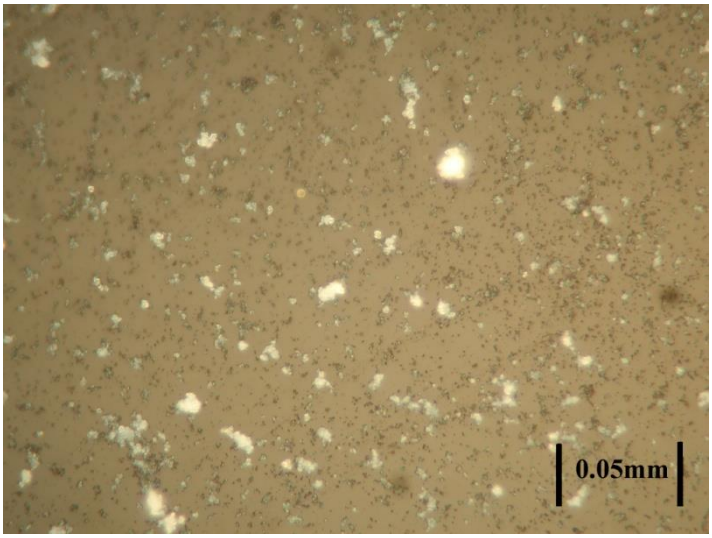

e)

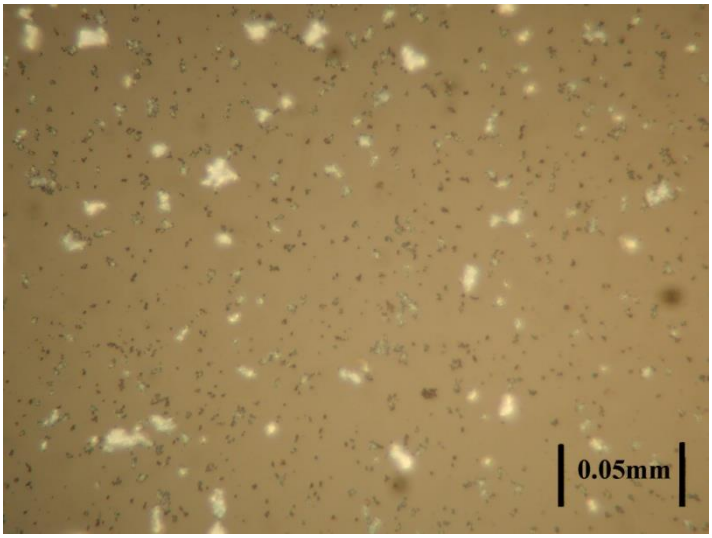

f)

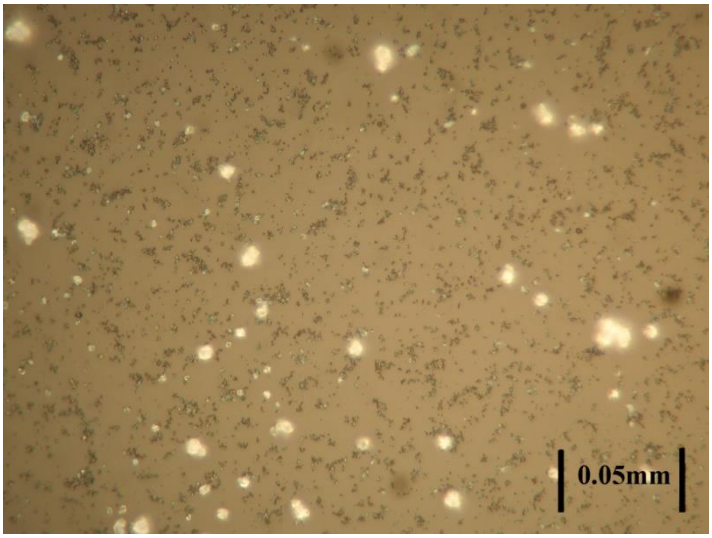

Figure 107. Series three micrographs a) 40/80 °C b) 50/80 °C c) 60/80 °C d) 70/80 °C e) 80/80 °C f) 90/80 °C.

Series 4

a)

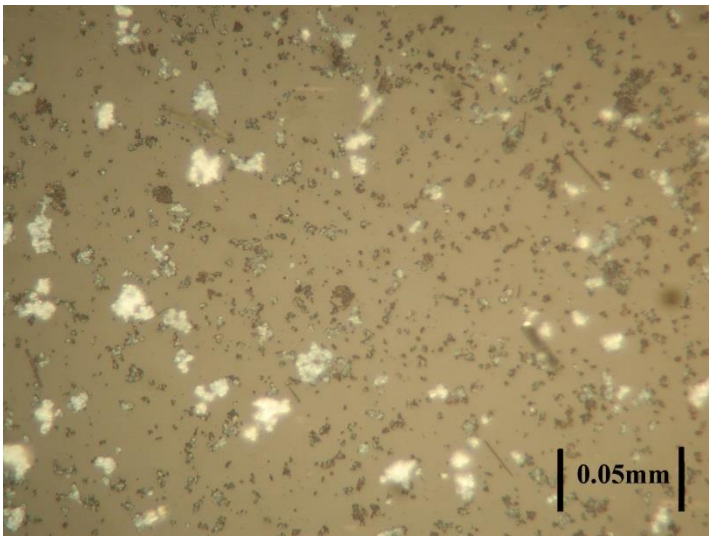

b)

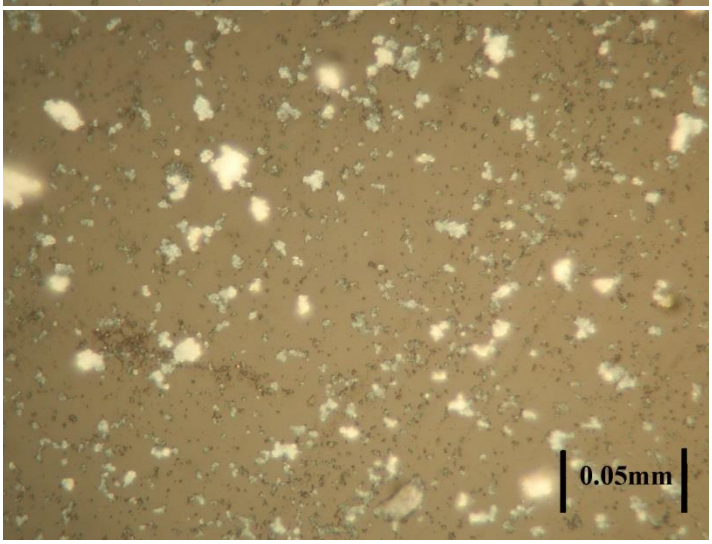

c)

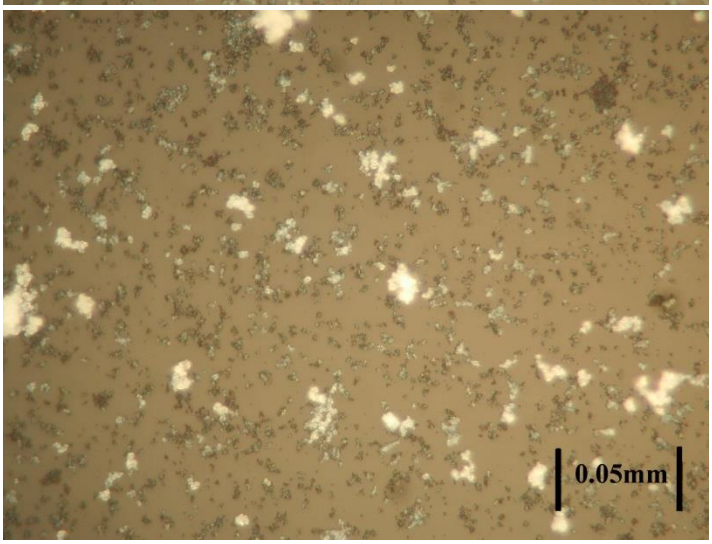

d)

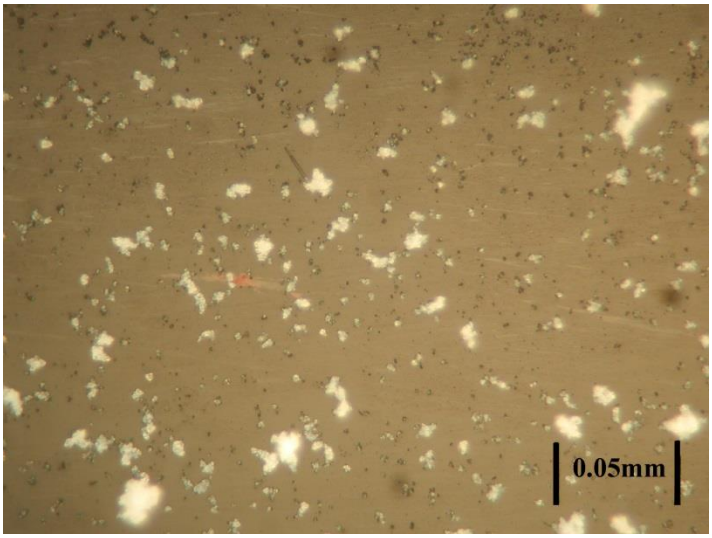

e)

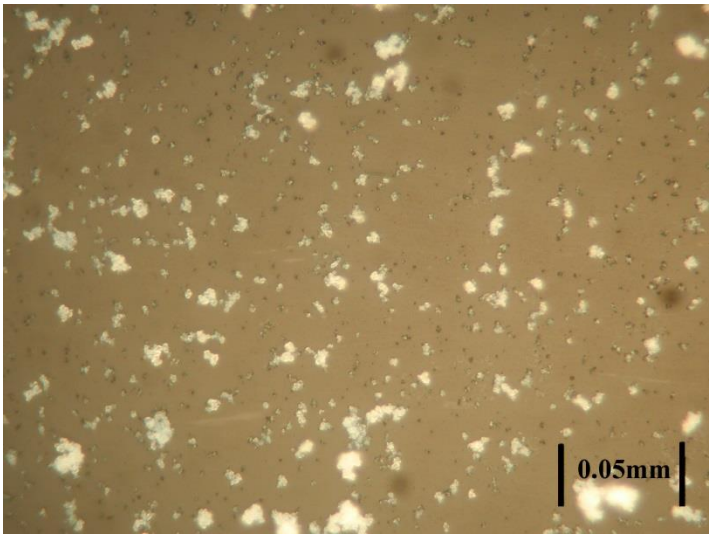

Figure 108. Series four micrographs a) 10:90 b) 20:80 c) 30:70 d) 40:60 e) 50:50

References

1. Rippin, D.W.T., 1993. Batch process systems engineering: a retrospective and prospective review. *Computers & chemical engineering*, *17*, pp.S1-S13.
2. Blömer, F. and Günther, H.O., 1998. Scheduling of a multi-product batch process in the chemical industry. *Computers in Industry*, *36*(3), pp.245-259.
3. Ravemark, D.E. and Rippin, D.W., 1998. Optimal design of a multi-product batch plant. *Computers & Chemical Engineering*, *22*(1), pp.177-183..
4. Petkov, S.B. and Maranas, C.D., 1998. Design of single-product campaign batch plants under demand uncertainty. *AIChE Journal*, *44*(4), pp.896-911.
5. Omar, M.K. and Teo, S.C., 2007. Hierarchical production planning and scheduling in a multi-product, batch process environment. *International Journal of Production Research*, *45*(5), pp.1029-1047.
6. Barker, M. and Rawtani, J., 2004. *Practical batch process management*. Elsevier.
7. Rippin, D.W.T., 1983. Design and operation of multiproduct and multipurpose batch chemical plants.—An analysis of problem structure. *Computers & chemical engineering*, *7*(4), pp.463-481.
8. Lee, C.Y., 1999. Minimizing makespan on a single batch processing machine with dynamic job arrivals. *International Journal of Production Research*, *37*(1), pp.219-236.
9. Takamatsu, T., Hashimoto, I. and Hasebe, S., 1982. Optimal design and operation of a batch process with intermediate storage tanks. *Industrial & Engineering Chemistry Process Design and Development*, *21*(3), pp.431-440.

10. Yeh, N.C. and Reklaitis, G.V., 1987. Synthesis and sizing of batch/semicontinuous processes: single product plants. *Computers & chemical engineering*, *11*(6), pp.639-654.

11. Liberopoulos, G., Kozanidis, G. and Hatzikonstantinou, O., 2010. Production scheduling of a multi-grade PET resin plant. *Computers & chemical engineering*, *34*(3), pp.387-400.

12. Hatzikonstantinou, O., Athanasiou, E. and Pandelis, D.G., 2012. Real-time production scheduling in a multi-grade PET resin plant under demand uncertainty. *Computers & Chemical Engineering*, *40*, pp.191-201.

13. Bitran, G.R. and Tirupati, D., 1989. Approximations for product departures from a single-server station with batch processing in multi-product queues.*Management science*, *35*(7), pp.851-878.

14. Kirschning, A., Solodenko, W. and Mennecke, K., 2006. Combining enabling techniques in organic synthesis: continuous flow processes with heterogenized catalysts. *Chemistry–A European Journal*, *12*(23), pp.5972-5990..

15. Li, S., Gross, G.A., Günther, P.M. and Köhler, J.M., 2011. Hydrothermal micro continuous-flow synthesis of spherical, cylinder-, star-and flower-like ZnO microparticles. *Chemical engineering journal*, *167*(2), pp.681-687.

16. Bavykin, D.V., Lapkin, A.A., Kolaczkowski, S.T. and Plucinski, P.K., 2005. Selective oxidation of alcohols in a continuous multifunctional reactor: Ruthenium oxide catalysed oxidation of benzyl alcohol. *Applied Catalysis A: General*, *288*(1), pp.175-184.

17. Webb, D. and Jamison, T.F., 2010. Continuous flow multi-step organic synthesis. *Chemical Science*, *1*(6), pp.675-680.

18. Quimby, B.D. and Sullivan, J.J., 1990. Evaluation of a microwave cavity, discharge tube, and gas flow system for combined gas chromatography-atomic emission detection. *Analytical Chemistry*, *62*(10), pp.1027-1034.

19. Mason, B.P., Price, K.E., Steinbacher, J.L., Bogdan, A.R. and McQuade, D.T., 2007. Greener approaches to organic synthesis using microreactor technology. *Chemical reviews*, *107*(6), pp.2300-2318.

20. Taghavi-Moghadam, S., Kleemann, A. and Golbig, G., 2001. Microreaction technology as a novel approach to drug design, process development and reliability. *Organic process research & development*, *5*(6), pp.652-658.

21. Baldyga, J. and Pohorecki, R., 1995. Turbulent micromixing in chemical reactors--a review. *The Chemical Engineering Journal and the Biochemical Engineering Journal*, *58*(2), pp.183-195.

22. Bernard, A.M. and Lauwerys, R.R., 1983. Continuous-flow system for automation of latex immunoassay by particle counting. *Clinical chemistry*,*29*(6), pp.1007-1011.

23. Siraganian, R.P., 1974. An automated continuous-flow system for the extraction and fluorometric analysis of histamine. *Analytical biochemistry*,*57*(2), pp.383-394.

24. Champ, D.R., Gulens, J. and Jackson, R.E., 1979. Oxidation-reduction sequences in ground water flow systems. *Canadian Journal of earth sciences*, *16*(1), pp.12-23.

25. Kenis, P.J., Ismagilov, R.F. and Whitesides, G.M., 1999. Microfabrication inside capillaries using multiphase laminar flow patterning. *Science*,*285*(5424), pp.83-85.

26. Luis, S.V. and Garcia-Verdugo, E., 2010. *Chemical reactions and processes under flow conditions* (No. 5). Royal Society of Chemistry.

27. Perry, J.H., 1950. Chemical engineers' handbook. *Journal of Chemical Education*, *27*, p.533.

28. AtkinsP, D.P., 2006. Atkins' Physical Chemistry, 8th EditionNew York.

29. Yatmaz, H.C., Wallis, C. and Howarth, C.R., 2001. The spinning disc reactor–studies on a novel TiO 2 photocatalytic reactor. *Chemosphere*, *42*(4), pp.397-403.

30. Oxley, P., Brechtelsbauer, C., Ricard, F., Lewis, N. and Ramshaw, C., 2000. Evaluation of spinning disk reactor technology for the manufacture of pharmaceuticals. *Industrial & engineering chemistry research*, *39*(7), pp.2175-2182.

31. Fan, X., Chen, H., Ding, Y., Plucinski, P.K. and Lapkin, A.A., 2008. Potential of 'nanofluids' to further intensify microreactors. *Green Chemistry*, *10*(6), pp.670-677.

32. Exchangers, M.H., 2000. Microreactors: New Technology for Modern Chemistry.

33. Ismagilov, Z.R., Podyacheva, O.Y., Pushkarev, V.V., Koryabkina, N.A., Antsiferov, V.N., Danchenko, Y.V., Solonenko, O.P. and Veringa, H., 2000. Development and study of metal foam heat-exchanging tubular reactor: Catalytic combustion of methane combined with methane steam reforming.*Studies in Surface Science and Catalysis*, *130*, pp.2759-2764.

34. Jas, G. and Kirschning, A., 2003. Continuous flow techniques in organic synthesis. *Chemistry–A European Journal*, *9*(23), pp.5708-5723.

35. Watts, P. and Haswell, S.J., 2003. Continuous flow reactors for drug discovery. *Drug discovery today*, *8*(13), pp.586-593.

36. Rajagopal, S. and Spatola, A.F., 1995. Mechanism of palladium-catalyzed transfer hydrogenolysis of aryl chlorides by formate salts. *The Journal of Organic Chemistry*, *60*(5), pp.1347-1355.

37. Stadler, A. and Kappe, C.O., 2002. Rapid formation of triarylphosphines by microwave-assisted transition metal-catalyzed CP cross-coupling reactions.*Organic letters*, *4*(20), pp.3541-3543.

38. Solodenko, W., Schoen, U., Messinger, J., Glinschert, A. and Kirschning, A., 2004. Microwave-assisted Suzuki-Miyaura reactions with an insoluble pyridine-aldoxime Pd-catalyst. *Synlett*, (10), pp.1699-1702.

39. Löwe, H. and Ehrfeld, W., 1999. State-of-the-art in microreaction technology: concepts, manufacturing and applications. *Electrochimica Acta*, *44*(21), pp.3679-3689.

40. Angeletti, E., Canepa, C., Martinetti, G. and Venturello, P., 1989. Amino groups immobilized on silica gel: an efficient and reusable heterogeneous catalyst for the Knoevenagel condensation. *Journal of the Chemical Society, Perkin Transactions 1*, (1), pp.105-107.

41. Fukuyama, T., Shinmen, M., Nishitani, S., Sato, M. and Ryu, I., 2002. A copper-free Sonogashira coupling reaction in ionic liquids and its application to a microflow system for efficient catalyst recycling. *Organic letters*, *4*(10), pp.1691-1694.

42. Burguete, M.I., Erythropel, H., Garcia-Verdugo, E., Luis, S.V. and Sans, V., 2008. Base supported ionic liquid-like phases as catalysts for the batch and continuous-flow Henry reaction. *Green Chemistry*, *10*(4), pp.401-407.

43. Sotenko, M.V., Rebroš, M., Sans, V.S., Loponov, K.N., Davidson, M.G., Stephens, G. and Lapkin, A.A., 2012. Tandem transformation of glycerol to esters. *Journal of biotechnology*, *162*(4), pp.390-397.

44. Usutani, H., Tomida, Y., Nagaki, A., Okamoto, H., Nokami, T. and Yoshida, J.I., 2007. Generation and reactions of o-bromophenyllithium without benzyne formation using a microreactor. *Journal of the American Chemical Society*, *129*(11), pp.3046-3047.

45. Hessel, V., Löwe, H. and Schönfeld, F., 2005. Micromixers—a review on passive and active mixing principles. *Chemical Engineering Science*, *60*(8), pp.2479-2501.

46. Kockmann, N., 2006. Transport processes and exchange equipment. *Micro process engineering: Fundamentals, devices, fabrication, and applications*, pp.71-113.

47. Kockmann, N., 2007. *Transport phenomena in micro process engineering*. Springer Science & Business Media.

48. Schwesinger, N., Frank, T. and Wurmus, H., 1996. A modular microfluid system with an integrated micromixer. *Journal of Micromechanics and Microengineering*, *6*(1), p.99.

49. Schwalbe, T., Autze, V., Hohmann, M. and Stirner, W., 2004. Novel innovation systems for a cellular approach to continuous process chemistry from discovery to market. *Organic process research & development*, *8*(3), pp.440-454.

50. Wirth, T. ed., 2013. *Microreactors in organic chemistry and catalysis*. John Wiley & Sons.

51. Hartman, R.L. and Jensen, K.F., 2009. Microchemical systems for continuous-flow synthesis. *Lab on a Chip*, *9*(17), pp.2495-2507.

52. Geyer, K., Gustafsson, T. and Seeberger, P.H., 2009. Developing continuous-flow microreactors as tools for synthetic chemists. *Synlett*, (15), pp.2382-2391.

53. Jähnisch, K., Hessel, V., Löwe, H. and Baerns, M., 2004. Chemistry in microstructured reactors. *Angewandte Chemie International Edition*, *43*(4), pp.406-446.

54. Yaseneva, P., Plaza, D., Fan, X., Loponov, K. and Lapkin, A., 2015. Synthesis of the antimalarial API artemether in a flow reactor. *Catalysis Today*, *239*, pp.90-96.

55. Schwalbe, T., Kadzimirsz, D. and Jas, G., 2005. Synthesis of a library of ciprofloxacin analogues by means of sequential organic synthesis in microreactors. *QSAR & Combinatorial Science*, *24*(6), pp.758-768.

56. Poe, S.L., Cummings, M.A., Haaf, M.P. and McQuade, D.T., 2006. Solving the Clogging Problem: Precipitate-Forming Reactions in Flow. *Angewandte Chemie International Edition*, *45*(10), pp.1544-1548.

57. Jongen, N., Donnet, M., Bowen, P., Lemaître, J., Hofmann, H., Schenk, R., Hofmann, C., Aoun-Habbache, M., Guillemet-Fritsch, S., Sarrias, J. and Rousset, A., 2003. Development of a Continuous Segmented Flow Tubular Reactor and the "Scale-out" Concept–In Search of Perfect Powders.*Chemical engineering & technology*, *26*(3), pp.303-305.

58. Donnet, M., Jongen, N., Lemaitre, J. and Bowen, P., 2000. New morphology of calcium oxalate trihydrate precipitated in a segmented flow tubular reactor.*Journal of materials science letters*, *19*(9), pp.749-750.

59. Sönnichsen, C. and Alivisatos, A.P., 2005. Gold nanorods as novel nonbleaching plasmon-based orientation sensors for polarized single-particle microscopy. *Nano letters*, *5*(2), pp.301-304.

60. Wagner, J. and Köhler, J.M., 2005. Continuous synthesis of gold nanoparticles in a microreactor. *Nano letters*, *5*(4), pp.685-691.

61. Shalom, D., Wootton, R.C., Winkle, R.F., Cottam, B.F., Vilar, R. and Wilde, C.P., 2007. Synthesis of thiol functionalized gold nanoparticles using a continuous flow microfluidic reactor. *Materials Letters*, *61*(4), pp.1146-1150.

62. Edel, J.B. and Fortt, R., 2002. Microfluidic routes to the controlled production of nanoparticles. *Chemical Communications*, (10), pp.1136-1137.

63. Cavani, F., Trifirò, F. and Vaccari, A., 1991. Hydrotalcite-type anionic clays: Preparation, properties and applications. *Catalysis today*, *11*(2), pp.173-301.

64. Iwan, A.A., 2008. *High temperature CO2 sequestration using solid absorbents: lithium zirconate and Mg-Al hydrotalcite* (Doctoral dissertation, University of bath).

65. Kohjiya, S., Sato, T., Nakayama, T. and Yamashita, S., 1981. Polymerization of propylene oxide by calcined synthetic hydrotalcite. *Die Makromolekulare Chemie, Rapid Communications*, *2*(3), pp.231-233.

66. Nakatsuka, T., Kawasaki, H., Yamashita, S. and Kohjiya, S., 1979. The polymerization of. BETA.-propiolactone by calcined synthetic hydrotalcite.*Bulletin of the Chemical Society of Japan*, *52*(8), pp.2449-2450.

67. Reichle, W.T., 1985. Catalytic reactions by thermally activated, synthetic, anionic clay minerals. *Journal of Catalysis*, *94*(2), pp.547-557.

68. Abelló, S., Medina, F., Tichit, D., Pérez-Ramírez, J., Groen, J.C., Sueiras, J.E., Salagre, P. and Cesteros, Y., 2005. Aldol condensations over

reconstructed Mg–Al hydrotalcites: structure–activity relationships related to the rehydration method. *Chemistry–A European Journal*, *11*(2), pp.728-739.

69. Suzuki, E. and Ono, Y., 1988. Aldol condensation reaction between formaldehyde and acetone over heat-treated synthetic hydrotalcite and hydrotalcite-like compounds. *Bulletin of the Chemical Society of Japan*,*61*(3), pp.1008-1010.

70. León, M., Díaz, E. and Ordóñez, S., 2011. Ethanol catalytic condensation over Mg–Al mixed oxides derived from hydrotalcites. *Catalysis today*,*164*(1), pp.436-442.

71. Watanabe, Y. and Tatsumi, T., 1998. Hydrotalcite-type materials as catalysts for the synthesis of dimethyl carbonate from ethylene carbonate and methanol. *Microporous and mesoporous materials*, *22*(1), pp.399-407.

72. Balasamy, R.J., Tope, B.B., Khurshid, A., Al-Ali, A.A., Atanda, L.A., Sagata, K., Asamoto, M., Yahiro, H., Nomura, K., Sano, T. and Takehira, K., 2011. Ethylbenzene dehydrogenation over FeO x/(Mg, Zn)(Al) O catalysts derived from hydrotalcites: Role of MgO as basic sites. *Applied Catalysis A: General*, *398*(1), pp.113-122.

73. Choudary, B.M., Kantam, M.L., Rahman, A., Reddy, C. and Rao, K.K., 2001. The First Example of Activation of Molecular Oxygen by Nickel in Ni-Al Hydrotalcite: A Novel Protocol for the Selective Oxidation of Alcohols.*Angewandte Chemie International Edition*, *40*(4), pp.763-766.

74. Prescott, H.A., Li, Z.J., Kemnitz, E., Trunschke, A., Deutsch, J., Lieske, H. and Auroux, A., 2005. Application of calcined Mg–Al hydrotalcites for Michael additions: an investigation of catalytic activity and acid–base properties. *Journal of Catalysis*, *234*(1), pp.119-130.

75. Figueras, F., Lakshmi Kantam, M. and Manoranjan Choudary, B., 2006. Solid base catalysts in organic synthesis. *Current Organic Chemistry*, *10*(13), pp.1627-1637.

76. Hutson, N.D., Speakman, S.A. and Payzant, E.A., 2004. Structural effects on the high temperature adsorption of CO2 on a synthetic hydrotalcite.*Chemistry of materials*, *16*(21), pp.4135-4143.

77. Tsuji, M., Mao, G., Yoshida, T. and Tamaura, Y., 1993. Hydrotalcites with an extended Al 3+-substitution: Synthesis, simultaneous TG-DTA-MS study, and their CO 2 adsorption behaviors. *Journal of materials research*, *8*(05), pp.1137-1142.

78. Yang, J.I. and Kim, J.N., 2006. Hydrotalcites for adsorption of CO2 at high temperature. *Korean Journal of Chemical Engineering*, *23*(1), pp.77-80.

79. Yong, Z., Mata, V. and Rodrigues, A.E., 2001. Adsorption of carbon dioxide onto hydrotalcite-like compounds (HTlcs) at high temperatures. *Industrial & Engineering Chemistry Research*, *40*(1), pp.204-209.

80. Lwin, Y. and Abdullah, F., 2009. High temperature adsorption of carbon dioxide on Cu–Al hydrotalcite-derived mixed oxides: kinetics and equilibria by thermogravimetry. *Journal of thermal analysis and calorimetry*, *97*(3), pp.885-889..

81. Ding, Y. and Alpay, E., 2000. Equilibria and kinetics of CO 2 adsorption on hydrotalcite adsorbent. *Chemical Engineering Science*, *55*(17), pp.3461-3474.

82. Tichit, D., Lhouty, M.H., Guida, A., Chiche, B.H., Figueras, F., Auroux, A., Bartalini, D. and Garrone, E., 1995. Textural properties and catalytic activity of hydrotalcites. *Journal of catalysis*, *151*(1), pp.50-59.

83. Wang, X.P., Yu, J.J., Cheng, J., Hao, Z.P. and Xu, Z.P., 2007. High-temperature adsorption of carbon dioxide on mixed oxides derived from hydrotalcite-like compounds. *Environmental science & technology*, *42*(2), pp.614-618.

84. Hutson, N.D. and Attwood, B.C., 2008. High temperature adsorption of CO2 on various hydrotalcite-like compounds. *Adsorption*, *14*(6), pp.781-789.

85. Othman, M.R., Rasid, N.M. and Fernando, W.J.N., 2006. Mg–Al hydrotalcite coating on zeolites for improved carbon dioxide adsorption. *Chemical engineering science*, *61*(5), pp.1555-1560.

86. Lopez, T., Bosch, P., Ramos, E., Gomez, R., Novaro, O., Acosta, D. and Figueras, F., 1996. Synthesis and characterization of sol-gel hydrotalcites. Structure and texture. *Langmuir*, *12*(1), pp.189-192.

87. Kloprogge, J.T., Wharton, D., Hickey, L. and Frost, R.L., 2002. Infrared and Raman study of interlayer anions CO32–, NO3–, SO42–and ClO4–in Mg/Al-hydrotalcite. *American Mineralogist*, *87*(5-6), pp.623-629.

88. Frache, A., Monticelli, O., Nocchetti, M., Tartaglione, G. and Costantino, U., 2011. Thermal properties of epoxy resin nanocomposites based on hydrotalcites. *Polymer degradation and stability*, *96*(1), pp.164-169.

89. Walspurger, S., Cobden, P.D., Safonova, O.V., Wu, Y. and Anthony, E.J., 2010. High CO2 Storage Capacity in Alkali-Promoted Hydrotalcite-Based Material: In Situ Detection of Reversible Formation of Magnesium Carbonate.*Chemistry–A European Journal*, *16*(42), pp.12694-12700.

90. Palmer, S.J., Frost, R.L., Ayoko, G. and Nguyen, T., 2008. Synthesis and Raman spectroscopic characterisation of hydrotalcite with CO32− and

(MoO4) 2− anions in the interlayer. *Journal of Raman Spectroscopy*, *39*(3), pp.395-401.

91. Martin, E.S., Stinson, J.M., Cedro III, V. and Horn Jr, W.E., Aluminum Company of America, 1998. *Two powder synthesis of hydrotalcite and hydrotalcite like compounds*. U.S. Patent 5,728,364.

92. Millange, F., Walton, R.I. and O'Hare, D., 2000. Time-resolved in situ X-ray diffraction study of the liquid-phase reconstruction of Mg–Al–carbonate hydrotalcite-like compounds. *Journal of Materials Chemistry*, *10*(7), pp.1713-1720.

93. Miyata, S., 1977. Synthesis of Hydrotalcite-Like Compounds and their Physico-Chemical Properties---The Systems Mg2+-Al3+-SO42-and Mg2+-Al3+-CrO42. *Clays and Clay Minerals*, *25*, pp.14-18.

94. Costantino, U., Marmottini, F., Nocchetti, M. and Vivani, R., 1998. New synthetic routes to hydrotalcite-like compounds-characterisation and properties of the obtained materials. *European Journal of Inorganic Chemistry*, *1998*(10), pp.1439-1446.

95. Zăvoianu, R., Ionescu, R., Pavel, O.D., Bîrjega, R. and Angelescu, E., 2011. Comparison between Me II Mg/Al hydrotalcites and hydrotalcite-supported Me (II) acetylacetonates (Me (II)= Co, Cu or Ni) catalysts for the epoxidation of cyclohexene with molecular oxygen. *Applied Clay Science*, *52*(1), pp.1-10.

96. Navajas, A., Campo, I., Arzamendi, G., Hernández, W.Y., Bobadilla, L.F., Centeno, M.A., Odriozola, J.A. and Gandía, L.M., 2010. Synthesis of biodiesel from the methanolysis of sunflower oil using PURAL® Mg–Al hydrotalcites as catalyst precursors. *Applied Catalysis B: Environmental*,*100*(1), pp.299-309.

97. Sato, T., Fujita, H., Endo, T., Shimada, M. and Tsunashima, A., 1988. Synthesis of hydrotalcite-like compounds and their physico-chemical properties. *Reactivity of Solids*, *5*(2), pp.219-228.

98. Rey, F., Fornes, V. and Rojo, J.M., 1992. Thermal decomposition of hydrotalcites. An infrared and nuclear magnetic resonance spectroscopic study. *Journal of the Chemical Society, Faraday Transactions*, *88*(15), pp.2233-2238.

99. Frost, R.L., Weier, M.L. and Kloprogge, J.T., 2003. Raman spectroscopy of some natural hydrotalcites with sulphate and carbonate in the interlayer.*Journal of Raman Spectroscopy*, *34*(10), pp.760-768.

100. Kloprogge, J.T., Hickey, L. and Frost, R.L., 2005. The effect of varying synthesis conditions on zinc chromium hydrotalcite: a spectroscopic study.*Materials chemistry and physics*, *89*(1), pp.99-109.

101. Mascolo, G., 1995. Synthesis of anionic clays by hydrothermal crystallization of amorphous precursors. *Applied Clay Science*, *10*(1), pp.21-30.

102. Frost, R.L. and Erickson, K.L., 2005. Raman spectroscopic study of the hydrotalcite desautelsite Mg 6 Mn 2 CO 3 (OH) 16· 4H 2 O. *Spectrochimica Acta Part A: Molecular and Biomolecular Spectroscopy*, *61*(11), pp.2697-2701.

103. Climent, M.J., Corma, A., Iborra, S., Epping, K. and Velty, A., 2004. Increasing the basicity and catalytic activity of hydrotalcites by different synthesis procedures. *Journal of Catalysis*, *225*(2), pp.316-326.

104. Pérez-Ramırez, J., Mul, G. and Moulijn, J.A., 2001. In situ Fourier transform infrared and laser Raman spectroscopic study of the thermal decomposition

of Co–Al and Ni–Al hydrotalcites. *Vibrational Spectroscopy*, *27*(1), pp.75-88.

105. Reichle, W.T., 1986. Synthesis of anionic clay minerals (mixed metal hydroxides, hydrotalcite). *Solid State Ionics*, *22*(1), pp.135-141.

106. Chen, Y.Z., Hwang, C.M. and Liaw, C.W., 1998. One-step synthesis of methyl isobutyl ketone from acetone with calcined Mg/Al hydrotalcite-supported palladium or nickel catalysts. *Applied Catalysis A: General*,*169*(2), pp.207-214.

107. Palmer, S.J. and Frost, R.L., 2011. Characterization of bayer hydrotalcites formed from bauxite refinery residue liquor. *Industrial & Engineering Chemistry Research*, *50*(9), pp.5346-5351.

108. Mantilla, A., Jácome-Acatitla, G., Morales-Mendoza, G., Tzompantzi, F. and Gómez, R., 2010. Photoassisted degradation of 4-chlorophenol and p-cresol using MgAl hydrotalcites. *Industrial & Engineering Chemistry Research*,*50*(5), pp.2762-2767.

109. Frost, R.L., Erickson, K.L. and Kloprogge, T.J., 2005. Vibrational spectroscopic study of the nitrate containing hydrotalcite mbobomkulite.*Spectrochimica Acta Part A: Molecular and Biomolecular Spectroscopy*,*61*(13), pp.2919-2925.

110. Adachi-Pagano, M., Forano, C. and Besse, J.P., 2003. Synthesis of Al-rich hydrotalcite-like compounds by using the urea hydrolysis reaction—control of size and morphology. *Journal of Materials Chemistry*, *13*(8), pp.1988-1993.

111. Nelson, S.A., 2006. Phyllosilicates (Micas, Chlorite, Talc, & Serpentine).*Tulane University [Web-page],[Refered 11 th April 2008] From: http://www. tulane. edu/~ sanelson/eens211/phyllosilicates. htm*.

112. Costa, D.G., Rocha, A.B., Souza, W.F., Chiaro, S.S.X. and Leitao, A.A., 2011. Ab Initio Simulation of Changes in Geometry, Electronic Structure, and Gibbs Free Energy Caused by Dehydration of Hydrotalcites Containing Cl− and CO32− Counteranions. *The Journal of Physical Chemistry B*, *115*(13), pp.3531-3537.

113. Cygan, R.T., Greathouse, J.A., Heinz, H. and Kalinichev, A.G., 2009. Molecular models and simulations of layered materials. *Journal of Materials Chemistry*, *19*(17), pp.2470-2481.

114. Allada, R.K., Navrotsky, A. and Boerio-Goates, J., 2005. Thermochemistry of hydrotalcite-like phases in the MgO-Al2O3-CO2-H2O system: A determination of enthalpy, entropy, and free energy. *American Mineralogist*,*90*(2-3), pp.329-335.

115. Allada, R.K., Pless, J.D., Nenoff, T.M. and Navrotsky, A., 2005. Thermochemistry of hydrotalcite-like phases intercalated with CO32-, NO3-, Cl-, I-, and ReO4. *Chemistry of materials*, *17*(9), pp.2455-2459.

116. Forano, C., Costantino, U., Prévot, V. and Gueho, C.T., 2013. Layered double hydroxides (LDH). *Handbook of clay science*, pp.Volume-5.

117. Miyata, S., 1980. Hydrotalcites in relation to composition. *Clays Clay Miner*,*28*(1), pp.50-56.

118. Catherine, E., 2008. Housecroft and Alan G. Sharpe. *Inorganic Chemistry (3rd Edition), Pearson Education Limited*.

119. Askeland, D.R. and Phulé, P.P., 2003. The science and engineering of materials.

120. Mermet, J.M., 1991. Use of magnesium as a test element for inductively coupled plasma atomic emission spectrometry diagnostics. *Analytica chimica acta*, *250*, pp.85-94.

121. Vela, N.P., Olson, L.K. and Caruso, J.A., 1993. Elemental speciation with plasma mass spectrometry. *Analytical Chemistry*, *65*(13), pp.585A-597A.

122. Stefansson, A., Gunnarsson, I. and Giroud, N., 2007. New methods for the direct determination of dissolved inorganic, organic and total carbon in natural waters by Reagent-Free™ Ion Chromatography and inductively coupled plasma atomic emission spectrometry. *Analytica chimica acta*,*582*(1), pp.69-74.

123. Montaser, A. and Golightly, D.W., 1987. Inductively coupled plasmas in analytical atomic spectrometry.

124. Clayden, J., Warren, W., Greeves, N. and Wothers, P., „Organic Chemistry “, 2001.

125. Harris, R.K., Becker, E.D., Cabral de Menezes, S.M., Goodfellow, R. and Granger, P., 2001. NMR nomenclature. Nuclear spin properties and conventions for chemical shifts (IUPAC recommendations 2001). *Pure and Applied Chemistry*, *73*(11), pp.1795-1818.

126. Barrett, E.P., Joyner, L.G. and Halenda, P.P., 1951. The determination of pore volume and area distributions in porous substances. I. Computations from nitrogen isotherms. *Journal of the American Chemical society*, *73*(1), pp.373-380.

127. Wen, N. and Brooker, M.H., 1995. Ammonium carbonate, ammonium bicarbonate, and ammonium carbamate equilibria: a Raman study. *The Journal of Physical Chemistry*, *99*(1), pp.359-368.

128. Günther, H., 2013. *NMR spectroscopy: basic principles, concepts and applications in chemistry*. John Wiley & Sons.

129. Fu, G., Nazar, L.F. and Bain, A.D., 1991. Aging processes of alumina sol-gels: Characterization of new aluminum polyoxycations by aluminum-27 NMR spectroscopy. *Chemistry of Materials*, *3*(4), pp.602-610.

130. Akitt, J.W., 1989. Multinuclear studies of aluminium compounds. *Progress in nuclear magnetic resonance spectroscopy*, *21*(1), pp.1-149.

131. Vyalikh, A., Costa, F.R., Wagenknecht, U., Heinrich, G., Massiot, D. and Scheler, U., 2009. From Layered Double Hydroxides to Layered Double Hydroxide-Based Nanocomposites A Solid-State NMR Study. *The Journal of Physical Chemistry C*, *113*(51), pp.21308-21313.

132. Allen, T., 2013. *Particle size measurement*. Springer.

133. Pletcher, D. and Walsh, F., Industrial Electrochemistry; 1990. *Chapman & Hall Chapters*, *1*, pp.1-172.

134. Martin, E.S., Stinson, J.M., Cedro III, V. and Horn Jr, W.E., Aluminum Company of America, 1998. *Two powder synthesis of hydrotalcite and hydrotalcite-like compounds with monovalent organic anions*. U.S. Patent 5,728,366.

135. Zumdahl, S.S., 1992. *Chemical principles*. DC Heath.

136. Young, F.E., 1944. The Heats of Formation of Al (NO3) 3· 6H2O and Al (NO3) 3· 9H2O1. *Journal of the American Chemical Society*, *66*(5), pp.777-779.

137. Samanta, A., Zhao, A., Shimizu, G.K., Sarkar, P. and Gupta, R., 2011. Post-combustion CO2 capture using solid sorbents: a review. *Industrial & Engineering Chemistry Research*, *51*(4), pp.1438-1463.

138. Astaria, G., Savage, D.W. and Bisio, A., 1983. Gas treating with chemical solvents.

139. Kohl, A.L. and Nielsen, R., 1997. *Gas purification*. Gulf Professional Publishing.

140. Maddox, R.N. and Campbell, J.M., 2004. *Gas conditioning and processing: gas treating and sulfur recovery*. Campbell Petroleum Services.

141. Wolsky, A.M., Daniels, E.J. and Jody, B.J., 1994. CO2 Capture from the flue gas of conventional fossil-fuel-fired power plants. *Environmental Progress*,*13*(3), pp.214-219.

142. Ryckebosch, E., Drouillon, M. and Vervaeren, H., 2011. Techniques for transformation of biogas to biomethane. *Biomass and bioenergy*, *35*(5), pp.1633-1645.

143. Hullu, J.D., Waassen, J.I.W., Van Meel, P.A., Shazad, S. and Vaessen, J.M.P., 2008. Comparing different biogas upgrading techniques. *Eindhoven University of Technology*, p.56.

144. Ohashi, T. and Nakagawa, K., 1998. Effect of potassium carbonate additive on CO 2 absorption in lithium zirconate powder. In *MRS Proceedings* (Vol. 547, p. 249). Cambridge University Press.

145. Xiong, R., Ida, J. and Lin, Y.S., 2003. Kinetics of carbon dioxide sorption on potassium-doped lithium zirconate. *Chemical Engineering Science*, *58*(19), pp.4377-4385.

146. Kato, M., Yoshikawa, S. and Nakagawa, K., 2002. Carbon dioxide absorption by lithium orthosilicate in a wide range of temperature and carbon dioxide concentrations. *Journal of Materials Science Letters*, *21*(6), pp.485-487.

147. Liang, Z., Marshall, M. and Chaffee, A.L., 2009. CO2 adsorption-based separation by metal organic framework (Cu-BTC) versus zeolite (13X).*Energy & Fuels*, *23*(5), pp.2785-2789.

148. Caskey, S.R., Wong-Foy, A.G. and Matzger, A.J., 2008. Dramatic tuning of carbon dioxide uptake via metal substitution in a coordination polymer with cylindrical pores. *Journal of the American Chemical Society*, *130*(33), pp.10870-10871.

149. Gurkan, B.E., de la Fuente, J.C., Mindrup, E.M., Ficke, L.E., Goodrich, B.F., Price, E.A., Schneider, W.F. and Brennecke, J.F., 2010. Equimolar CO2 absorption by anion-functionalized ionic liquids. *Journal of the American Chemical Society*, *132*(7), pp.2116-2117.

150. Auroux, A. and Gervasini, A., 1990. Microcalorimetric study of the acidity and basicity of metal oxide surfaces. *Journal of Physical Chemistry*, *94*(16), pp.6371-6379.

151. Jones, K., Davies, T.J., Emblem, H.G. and Parkes, P., 1986. Spinel formation from magnesium aluminium double alkoxides. In *MRS Proceedings* (Vol. 73, p. 111). Cambridge University Press.

152. Barker, M.G., Gadd, P.G. and Begley, M.J., 1984. Identification and characterisation of three novel compounds in the sodium–aluminium–oxygen system. *Journal of the Chemical Society, Dalton Transactions*, (6), pp.1139-1146.

153. Böckelmann, H.K. and Schlecht, R.G., 1974. Raman scattering from microcrystals of MgO. *Physical Review B*, *10*(12), p.5225.

154. Little, L.H. and Amberg, C.H., 1962. Infrared spectra of carbon monoxide and carbon dioxide adsorbed on Chromia-Alumina and on Alumina. *Canadian Journal of Chemistry*, *40*(10), pp.1997-2006.

155. Rao, A.B. and Rubin, E.S., 2002. A technical, economic, and environmental assessment of amine-based CO2 capture technology for power plant greenhouse gas control. *Environmental science & technology*, *36*(20), pp.4467-4475.

156. Curran, G.P., Clancey, J.T., Scarpiel,. D.A., Fink, C.E. and Gorin, E., 1966. Carbon dioxide acceptor process. *Chemical Engineering Progress*, *62*(2), p.80.

157. Silaban, A. and Harrison, D.P., 1995. High temperature capture of carbon dioxide: characteristics of the reversible reaction between CaO (s) and CO2 (g). *Chemical Engineering Communications*, *137*(1), pp.177-190.

158. Shimizu, T., Hirama, T., Hosoda, H., Kitano, K., Inagaki, M. and Tejima, K., 1999. A twin fluid-bed reactor for removal of CO 2 from combustion processes. *Chemical Engineering Research and Design*, *77*(1), pp.62-68.

159. Lin, S.Y., Suzuki, Y., Hatano, H. and Harada, M., 2002. Developing an innovative method, HyPr-RING, to produce hydrogen from hydrocarbons.*Energy Conversion and Management*, *43*(9), pp.1283-1290.

160. Abanades, J.C., Rubin, E.S. and Anthony, E.J., 2004. Sorbent cost and performance in CO2 capture systems. *Industrial & Engineering Chemistry Research*, *43*(13), pp.3462-3466.

161. Hayashi, H., Taniuchi, J., Furuyashiki, N., Sugiyama, S., Hirano, S., Shigemoto, N. and Nonaka, T., 1998. Efficient recovery of carbon dioxide from flue gases of coal-fired power plants by cyclic fixed-bed operations over K2CO3-on-carbon. *Industrial & engineering chemistry research*, *37*(1), pp.185-191.

162. Hoffman, J.S., Fauth, D.J. and Pennline, H.W., 2002, September. Development of novel dry regenerable sorbents for CO2 capture. In *19th Annual International Pittsburgh Coal Conference* (pp. 1-34).

163. Green, D.A., Turk, B.S., Portzer, J.W., Gupta, R.P., McMichael, W.J., Liang, Y., Moore, T. and Harrison, D.P., 2005. Carbon dioxide capture from flue gas using dry regenerable sorbents. *Quarterly Technical Progress Report, Research Triangle Institute*.

164. Nakagawa, K. and Ohashi, T., 1998. A novel method of CO 2 capture from high temperature gases. *Journal of the Electrochemical Society*, *145*(4), pp.1344-1346.

165. Xiong, R., Ida, J. and Lin, Y.S., 2003. Kinetics of carbon dioxide sorption on potassium-doped lithium zirconate. *Chemical Engineering Science*, *58*(19), pp.4377-4385.

166. Yong, Z., Mata, V. and Rodrigues, A.E., 2002. Adsorption of carbon dioxide at high temperature—a review. *Separation and Purification Technology*,*26*(2), pp.195-205..

167. Hufton, J.R., Mayorga, S. and Sircar, S., 1999. Sorption-enhanced reaction process for hydrogen production. *AIChE Journal*, *45*(2), pp.248-256.

168. Mattisson, T., Lyngfelt, A. and Cho, P., 2001. The use of iron oxide as an oxygen carrier in chemical-looping combustion of methane with inherent separation of CO 2. *Fuel*, *80*(13), pp.1953-1962.

169. Mattisson, T., Järdnäs, A. and Lyngfelt, A., 2003. Reactivity of some metal oxides supported on alumina with alternating methane and oxygen application for chemical-looping combustion. *Energy & Fuels*, *17*(3), pp.643-651.

170. Jin, H., Okamoto, T. and Ishida, M., 1999. Development of a novel chemical-looping combustion: synthesis of a solid looping material of NiO/NiAl2O4.*Industrial & Engineering Chemistry Research*, *38*(1), pp.126-132.

171. Yu, J., Corripio, A.B., Harrison, D.P. and Copeland, R.J., 2003. Analysis of the sorbent energy transfer system (SETS) for power generation and CO 2 capture. *Advances in Environmental Research*, *7*(2), pp.335-345.

172. Ryu, H.J., Bae, D.H. and Jin, G.T., 2002, October. Carbon deposition characteristics of NiO based oxygen carrier particles for chemical-looping combustor. In *Proceedings of GHGT-6, Kyoto, Japan, October*.

173. Hattori, H., 1995. Heterogeneous basic catalysis. *Chemical Reviews*, *95*(3), pp.537-558.

174. áLakshmi Kantam, M. and áKoteswara Rao, K., 2001. Layered double hydroxide fluoride: a novel solid base catalyst for C–C bond formation. *Green Chemistry*, *3*(5), pp.257-260.

175. Botalova, O., Schwarzbauer, J., Frauenrath, T. and Dsikowitzky, L., 2009. Identification and chemical characterization of specific organic constituents of petrochemical effluents. *Water research*, *43*(15), pp.3797-3812.

176. Pérez, M.H., Peñuela, G., Maldonado, M.I., Malato, O., Fernández-Ibáñez, P., Oller, I., Gernjak, W. and Malato, S., 2006. Degradation of pesticides in water using solar advanced oxidation processes. *Applied Catalysis B: Environmental*, *64*(3), pp.272-281.

177. Pera-Titus, M., Garcıa-Molina, V., Baños, M.A., Giménez, J. and Esplugas, S., 2004. Degradation of chlorophenols by means of advanced oxidation processes: a general review. *Applied Catalysis B: Environmental*, *47*(4), pp.219-256.

178. H. Mullre-Tamm, H.F., G. Schweier, L. Reuter, *German Patent 2163851-2 to BASF AG*. 1973.

179. Rahul, R., Satyarthi, J.K. and Srinivas, D., 2011. Lanthanum and zinc incorporated hydrotalcites as solid base catalysts for biodiesel and biolubricants production. *Indian Journal of Chemistry-Part A InorganicPhysical Theoretical and Analytical*, *50*(8), p.1017.

180. Tichit, D., Das, N., Coq, B. and Durand, R., 2002. Preparation of Zr-containing layered double hydroxides and characterization of the acido-basic properties of their mixed oxides. *Chemistry of materials*, *14*(4), pp.1530-1538..

181. Van Rossum, G., Kersten, S.R. and van Swaaij, W.P., 2007. Catalytic and noncatalytic gasification of pyrolysis oil. *Industrial & engineering chemistry research*, *46*(12), pp.3959-3967.

182. Kechagiopoulos, P.N., Voutetakis, S.S., Lemonidou, A.A. and Vasalos, I.A., 2006. Hydrogen production via steam reforming of the aqueous phase of bio-oil in a fixed bed reactor. *Energy & Fuels*, *20*(5), pp.2155-2163.

183. Wu, C., Huang, Q., Sui, M., Yan, Y. and Wang, F., 2008. Hydrogen production via catalytic steam reforming of fast pyrolysis bio-oil in a two-stage fixed bed reactor system. *Fuel Processing Technology*, *89*(12), pp.1306-1316.

184. Wang, Z.X., Dong, T., Yuan, L.X., Kan, T., Zhu, X.F., Torimoto, Y., Sadakata, M. and Li, Q.X., 2007. Characteristics of bio-oil-syngas and its utilization in Fischer-Tropsch synthesis. *Energy & Fuels*, *21*(4), pp.2421-2432.

185. Li, C., Hirabayashi, D. and Suzuki, K., 2009. Development of new nickel based catalyst for biomass tar steam reforming producing H 2-rich syngas.*Fuel Processing Technology*, *90*(6), pp.790-796.

186. Fogassy, G., Thegarid, N., Toussaint, G., van Veen, A.C., Schuurman, Y. and Mirodatos, C., 2010. Biomass derived feedstock co-processing with vacuum gas oil for second-generation fuel production in FCC units. *Applied Catalysis B: Environmental*, *96*(3), pp.476-485.

187. Garcia, L., French, R., Czernik, S. and Chornet, E., 2000. Catalytic steam reforming of bio-oils for the production of hydrogen: effects of catalyst composition. *Applied Catalysis A: General*, *201*(2), pp.225-239.

188. Galdámez, J.R., Garcia, L. and Bilbao, R., 2005. Hydrogen production by steam reforming of bio-oil using coprecipitated Ni-Al catalysts. Acetic acid as a model compound. *Energy & Fuels*, *19*(3), pp.1133-1142.

189. Wang, D., Czernik, S., Montane, D., Mann, M. and Chornet, E., 1997. Biomass to hydrogen via fast pyrolysis and catalytic steam reforming of the pyrolysis oil or its fractions. *Industrial & Engineering Chemistry Research*,*36*(5), pp.1507-1518.

190. Al-Ubaid, A. and Wolf, E.E., 1988. Steam reforming of methane on reduced non-stoichiometric nickel aluminate catalysts. *Applied Catalysis*, *40*, pp.73-85.

191. Suh, D.J., Park, T.J., Kim, J.H. and Kim, K.L., 1998. Nickel–alumina aerogel catalysts prepared by fast sol–gel synthesis. *Journal of non-crystalline solids*, *225*, pp.168-172.

192. Clause, O., Rebours, B., Merlen, E., Trifiro, F. and Vaccari, A., 1992. Preparation and characterization of nickel-aluminum mixed oxides obtained by thermal decomposition of hydrotalcite-type precursors. *Journal of Catalysis*, *133*(1), pp.231-246.

193. El-Shobaky, G.A., Ghoneim, N.M. and Sultan, E.A., 1983. Thermal decomposition of nickel aluminium mixed hydroxides and formation of nickel aluminate spinel. *Thermochimica Acta*, *63*(1), pp.39-49.

194. Joo, O.S. and Jung, K.D., 2002. CH~ 4 Dry Reforming on Alumina-Supported Nickel Catalyst. *Bulletin-Korean chemical society*, *23*(8), pp.1149-1153.

195. Scheffer, B., Molhoek, P. and Moulijn, J.A., 1989. Temperature-programmed reduction of NiOWO3/Al2O3 Hydrodesulphurization catalysts. *Applied catalysis*, *46*(1), pp.11-30.

196. Llorca, J., Homs, N., Sales, J. and de la Piscina, P.R., 2002. Efficient production of hydrogen over supported cobalt catalysts from ethanol steam reforming. *Journal of Catalysis*, *209*(2), pp.306-317.

197. Sánchez-Sánchez, M.C., Navarro, R.M. and Fierro, J.L.G., 2007. Ethanol steam reforming over Ni/MxOy–Al2O3 (M= Ce, La, Zr and Mg) catalysts:

influence of support on the hydrogen production. *International Journal of Hydrogen Energy*, *32*(10), pp.1462-1471.

198. Wynblatt, P. and Gjostein, N.A., 1976. Particle growth in model supported metal catalysts—I. Theory. *Acta Metallurgica*, *24*(12), pp.1165-1174.

199. Squattrito, P.J., Rudolf, P.R. and Clearfield, A., 1987. Crystal structure of a complex basic zirconium sulfate. *Inorganic Chemistry*, *26*(25), pp.4240-4244.

200. Alves Rosa, M.A., Sanhueza, C.S.S., Santilli, C.V., Pulcinelli, S.H. and Briois, V., 2008. Stimuli-responsive controlled growth of mono-and bidimensional particles from basic zirconium sulfate hydrosols. *The Journal of Physical Chemistry B*, *112*(30), pp.9006-9012.

201. McWhan, D.T. and Lundgren, G., 1966. The crystal structure of Zr2 (OH) 2 (SO4) 3 (H2O) 4. *Inorganic Chemistry*, *5*(2), pp.284-289.

202. Chatterjee, M., Ray, J., Chatterjee, A. and Ganguli, D., 1989. Characterization of basic zirconium sulphate, a precursor for zirconia.*Journal of materials science letters*, *8*(5), pp.548-550.

203. Reddy, J.S. and Sayari, A., 1996. Nanoporous zirconium oxide prepared using the supramolecular templating approach. *Catalysis letters*, *38*(3-4), pp.219-223.

204. Romannikov, V.N., Fenelonov, V.B., Paukshtis, E.A., Derevyankin, A.Y. and Zaikovskii, V.I., 1998. Mesoporous basic zirconium sulfate: structure, acidic properties and catalytic behaviour. *Microporous and mesoporous materials*,*21*(4), pp.411-419.

205. Clearfield, A., 1964. Crystalline hydrous zirconia. *Inorganic Chemistry*, *3*(1), pp.146-148.

206. H Nielsen, R., H Schlewitz, J. and Nielsen, H., 1997. Zirconium and zirconium compounds. *Kirk-Othmer Encyclopedia of Chemical Technology*.

207. Nielsen, R.H. and Govro, R.L., 1956. *Zirconium Purification, using A Basic Sulfate Precipitation* (No. BM-RI-5214). Bureau of Mines.

208. Singer, J. and Cromer, D.T., 1959. The crystal structure analysis of zirconium sulphate tetrahydrate. *Acta Crystallographica*, *12*(10), pp.719-723.

209. Babou, F., Coudurier, G. and Vedrine, J.C., 1995. Acidic properties of sulfated zirconia: an infrared spectroscopic study. *Journal of Catalysis*,*152*(2), pp.341-349.

210. Sohn, J.R. and Lee, D.G., 2003. Characterization of zirconium sulfate supported on TiO2 and activity for acid catalysis. *Korean Journal of Chemical Engineering*, *20*(6), pp.1030-1036.

211. Nakamoto, K., 1986. *Infrared and Raman spectra of inorganic and coordination compounds*. John Wiley & Sons, Ltd.